

# Fundamental characteristics of friction riveted multi-material joints

(Vom Promotionsausschuss der Technischen Universität Hamburg-Harburg als Dissertation angenommene Arbeit)

J. Altmeyer



# **Fundamental characteristics of friction riveted multi-material joints**

(Vom Promotionsausschuss der Technischen Universität Hamburg-Harburg als Dissertation angenommene Arbeit)

**J. Altmeyer**

---

Die HZG Reporte werden kostenlos abgegeben.  
HZG Reports are available free of charge.

Anforderungen/Requests:

Helmholtz-Zentrum Geesthacht  
Zentrum für Material- und Küstenforschung GmbH  
Bibliothek/Library  
Max-Planck-Straße 1  
21502 Geesthacht  
Germany  
Tel.: +49 4152 87-1690  
Fax.: +49 4152 87-1717  
E-Mail: [bibliothek@hzg.de](mailto:bibliothek@hzg.de)

*Druck: HZG-Hausdruckerei*

Als Manuskript vervielfältigt.  
Für diesen Bericht behalten wir uns alle Rechte vor.

ISSN 2191-7833

Helmholtz-Zentrum Geesthacht  
Zentrum für Material- und Küstenforschung GmbH  
Max-Planck-Straße 1  
21502 Geesthacht

[www.hzg.de](http://www.hzg.de)

## Fundamental characteristics of friction riveted multi-material joints

*(Vom Promotionsausschuss der Technischen Universität Hamburg-Harburg als Dissertation angenommene Arbeit)*

Julie Altmeyer

*175 pages with 142 figures and 26 tables*

### Abstract

In the last decades, the transportation industry has been challenged by cost-saving requirements, ever-stronger environmental protection regulations and the significant growth of transport volume. One approach for tackling these challenges is the development of new, improved transportation vehicles using new materials and innovative joining technologies.

A new and very promising joining technology is friction riveting (FricRiveting), a friction-based spot-joining process developed at the Helmholtz-Zentrum Geesthacht. FricRiveting bridges the gap between mechanical fastening and welding, and offers advantages such as short joining cycle times and a minimum of surface pre-treatment of the joining partners. In the present study, the feasibility of FricRiveting has been demonstrated for the first time for carbon fibre-reinforced materials using multi-material joints produced using carbon fibre-reinforced thermoplastic polymer PEEK (polyether ether ketone) and titanium. From the knowledge gained about the joint formation mechanisms and the mechanical properties of the joints, a design concept for woven fabric-reinforced polymer single-lap shear joints (composite-composite joints) is proposed.

In order to fully understand the effect of the FricRiveting process on the joint properties and the influence of fibre reinforcement (the type of reinforcement, short- and long woven fibres, and fibre volume content), experimental work was carried out on the analysis of unreinforced, short carbon fibre-reinforced and woven-reinforced PEEK laminates. As an intermediate step, design of experiments (DoE) was used to investigate the influence of the process parameters on the joint formation and the mechanical performance of the joints, in order to achieve a better understanding of the process. The fundamental understanding of microstructure-mechanical performance-process relationships achieved in this way was applied to control the formation of joints and to tailor their mechanical performance to specific requirements. An optimised process parameter set, leading to improved mechanical performance, was determined by statistical regression models using analysis of variance (ANOVA) techniques. The joints produced using this parameter set showed improved pull-out performance, reaching the strength levels of the titanium rivet base material, with final ductile failure occurring outside the joining area.

These optimised joints were then characterized by analysing the process-related microstructural properties of the metal and composite region of the joint, and the physicochemical and mechanical properties. The microstructural investigations of the joining area revealed the presence of zones demonstrating different thermomechanical and heat effects in the metallic and the composite regions of the joint, which indicated severe microstructural changes caused by process-related high heating rates, temperatures and plastic deformation.

With the knowledge obtained from the investigation of unreinforced and short carbon-fibre PEEK/titanium joints, a transferability study was carried out to evaluate the joinability of grade 3 titanium and woven fabric-reinforced PEEK. After optimising these joints, a design concept for friction riveted single-lap shear joints was developed by analysing the extent to which the key design parameters edge distance, specimen width and clamping torque influenced the strength of the joints. The mechanical performance of the resulting high-strength single-lap shear joint was then placed into context by comparing it with state-of-the-art bolted composite joints provided by Airbus. The optimised friction-riveted single-lap shear joints achieved a joint efficiency 21% higher than the state-of-the-art mechanically fastened joints provided by Airbus. Hence it was proven that the FricRiveting process offers great potential to be applied as an alternative joining technology, especially in aircraft structures.

---

## Grundlegende Eigenschaften von reibgenieteten Multi-Material-Verbindungen

### Zusammenfassung

Seit mehreren Jahrzehnten unterzieht sich die Transportindustrie einem starken Wandel, der von diversen Herausforderungen geprägt ist. Dabei stehen enorme Kosteneinsparungen, neue Umweltschutzbestimmungen sowie der signifikante Anstieg des zu transportierenden Volumens im Fokus. Ein Ansatz diesen Anforderungen gerecht zu werden, ist die Entwicklung von neuen, verbesserten Transportmitteln, unter dem Einsatz neuer Materialien und innovativer Füge Technologien.

Eine neue und sehr vielversprechende Füge Technologie ist das Reibnieten (FricRiveting), ein auf Reibung basierender Punktfügeprozess der am Helmholtz-Zentrum Geesthacht entwickelt wurde. FricRiveting bildet den Brückenschlag zwischen mechanischer Befestigung und Schweißverbindungen und bietet dabei gleichzeitig Vorteile wie kurze Fügezyklen sowie geringe Oberflächenvorbereitung der Fügepartner. In dieser Studie wurde erstmalig die Machbarkeit von FricRiveting für kohlefaserverstärkte Kunststoffe, am Beispiel von Multi-Material-Verbindungen, bestehend aus dem kohlefaserverstärkten, thermoplastischen Kunststoff PEEK (polyether ether ketone) und Titan, gezeigt. Basierend auf dem Wissen über Verbindungsentstehungsmechanismen und deren mechanischen Eigenschaften, wurde ein Designkonzept für Überlappverbindungen (composite-composite joints) aus gewebeverstärktem PEEK vorgeschlagen.

Um den Effekt des FricRiveting Prozesses auf die Verbindungseigenschaften nachzuvollziehen sowie den Einfluss der Faserverstärkung (Art der Verstärkung, ob verstärkt durch kurze oder verwobene, lange Fasern und den Faservolumengehalt) zu untersuchen, wurden Versuche mit unverstärkten, kurzfaserverstärkten und gewebeverstärkten PEEK Kunststoffen durchgeführt. Mit dem Ziel eines besseren Prozessverständnisses, wurde in einem Zwischenschritt der Einfluss der Prozessparameter auf die Verbindungsentstehung sowie ebenfalls auf das mechanische Verhalten der Verbindung mittels statistischer Versuchsplanung (DoE), untersucht. Das auf diesem Wege erlangte, fundamentale Verständnis über die Beziehungen zwischen Mikrostruktur, Fügeprozess und mechanischem Verhalten der Verbindung wurde ferner eingesetzt, um die Verbindungsentstehung und das mechanische Verhalten auf bestimmte Bedingungen zuzuschneiden. Dementsprechend wurde unter Anwendung eines statistischen Regressionsmodelles, der Varianzanalyse (ANOVA), ein optimierter Prozessparametersatz bestimmt, welcher zu verbessertem, mechanischen Verhalten führt. Die mit diesem Prozessparametersatz hergestellten Verbindungen zeigten verbesserte Auszugsfestigkeit auf und erreichten die Grundmaterialfestigkeit des Titanriets, wobei das Versagen durch einen duktilen Versagenstyp außerhalb der Fügestelle stattfand.

Des Weiteren wurden diese optimierten Verbindungen durch die Analyse der prozessbedingten, mikrostrukturellen Eigenschaften der metallischen Bereiche sowie der Verbundwerkstoffbereiche der Verbindung wie auch der physikochemischen und mechanischen Eigenschaften, charakterisiert. Die mikrostrukturelle Untersuchung der Fügestelle zeigte dabei das Vorhandensein von diversen thermisch und thermomechanisch beeinflussten Zonen auf. Dieser Sachverhalt weist auf massive, mikrostrukturelle Veränderungen hin, verursacht durch die prozessbedingten hohen Heizraten, Temperaturen und plastischen Verformungen.

Um die Fügbarkeit von Titan grade 3 und gewebeverstärktem PEEK zu evaluieren, wurde eine Übertragbarkeitsstudie unter Anwendung des zuvor erlangten Wissens aus den Untersuchungen von Verbindungen bestehend aus unverstärktem und kurzfaserverstärktem PEEK in Kombination mit Titan, durchgeführt. Nachdem eine Optimierung dieser Verbindungen realisiert wurde, konnte ein Designkonzept für reibgenietete Überlappverbindungen entwickelt werden. Dabei wurde analysiert, inwieweit die Schlüsselparameter des Designkonzepts, Randabstand, Probenbreite und Anzugsmoment, die Festigkeit der Verbindung beeinflussen. Das mechanische Verhalten der entwickelten, hochfesten Überlappverbindungen wurde im Folgenden in einen Kontext gebracht. Hierzu wurden die reibgenietete, mit von Airbus bereitgestellten Verbindungen, die dem Stand der Technik entsprechen, verglichen. Die reibgenieteten Überlappverbindungen konnten dabei eine Verbindungseffizienz erreichen, die 21% über der der mechanischen Referenzverbindung lag. Somit wurde gezeigt, dass FricRiveting das Potenzial bietet, um als innovatives Fügeverfahren, beispielsweise in der Luftfahrtindustrie, eingesetzt zu werden.

# Contents

<b>1. Introduction</b>	<b>1</b>
1.1. Motivation . . . . .	1
1.2. Objectives . . . . .	3
<b>2. State of the Art</b>	<b>4</b>
2.1. Joining of composites . . . . .	4
2.1.1. Mechanical fastening . . . . .	5
2.1.2. Adhesive Bonding . . . . .	6
2.1.3. Welding . . . . .	8
2.1.4. Hybrid joining . . . . .	9
2.2. FricRiveting . . . . .	9
2.2.1. Characteristics of the technology . . . . .	9
2.2.2. Process parameters and variables . . . . .	10
2.2.3. Joining and monitoring . . . . .	12
2.2.4. Process phases . . . . .	12
2.2.5. Mechanical energy input . . . . .	14
2.2.6. Microstructural zones in the joining region . . . . .	15
2.2.7. Advantages and challenges . . . . .	16
2.2.8. Previous research on FricRiveting . . . . .	17
<b>3. Experimental approach</b>	<b>22</b>
<b>4. Materials and methods</b>	<b>24</b>
4.1. Base materials and specimen geometries . . . . .	24
4.1.1. Titanium rivets . . . . .	24
4.1.2. Polyether ether ketone . . . . .	25
4.1.3. Polyether ether ketone reinforced with 30% short carbon fibres	26
4.1.4. Woven fabric-reinforced polyether ether ketone laminates . .	27
4.2. Friction riveting equipment and joining procedure . . . . .	28
4.2.1. Joining equipment . . . . .	28
4.2.2. Friction riveting joining procedure . . . . .	30
4.3. Statistical methods . . . . .	30
4.4. Temperature measurement . . . . .	32
4.5. Nondestructive testing by X-ray radiography . . . . .	33
4.6. Microstructural analysis . . . . .	34
4.6.1. Light optical microscopy . . . . .	34
4.6.2. Scanning electron microscopy . . . . .	34

4.7.	Thermal and physicochemical properties . . . . .	35
4.7.1.	Thermogravimetric analysis . . . . .	35
4.8.	Global mechanical performance . . . . .	35
4.8.1.	Pull-out tensile testing . . . . .	35
4.8.2.	Bearing testing . . . . .	37
4.8.3.	Torsion testing . . . . .	37
4.8.4.	Lap shear testing . . . . .	39
<b>5.</b>	<b>Development of FricRiveting for PEEK/titanium joints</b>	<b>41</b>
5.1.	Selection of a suitable rivet material . . . . .	41
5.2.	Feasibility study on PEEK/grade 3 titanium joints . . . . .	43
5.2.1.	Assessment of the joint formation . . . . .	45
5.2.2.	Assessment of the joint mechanical performance . . . . .	49
5.3.	Summary and conclusion . . . . .	51
<b>6.</b>	<b>Relationship between process, microstructure and mechanical performance</b>	<b>53</b>
6.1.	FricRiveting of short carbon fibre-reinforced PEEK and grade 3 titanium . . . . .	53
6.2.	Influence of the process parameters on joint formation . . . . .	57
6.2.1.	Mushrooming efficiency of the deformed rivet . . . . .	57
6.2.2.	Rivet penetration depth . . . . .	59
6.2.3.	Mechanical energy input . . . . .	59
6.3.	Influence of the process parameters on joint performance . . . . .	61
6.3.1.	Ultimate pull-out tensile force . . . . .	61
6.4.	Statistical model validation . . . . .	64
6.5.	Influence of rivet anchoring performance on tensile strength . . . . .	67
6.6.	Thermal history, microstructure and local mechanical properties . . . . .	69
6.6.1.	Temperature evolution during joining . . . . .	69
6.6.2.	Microstructural analysis of the titanium rivet . . . . .	73
6.6.3.	Microstructural analysis of the PEEK composite . . . . .	79
6.6.4.	Simplified material flow model for PEEK composite . . . . .	87
6.6.5.	Process-related thermomechanical degradation of the composite . . . . .	88
6.7.	Summary and conclusions . . . . .	91
<b>7.</b>	<b>Determination of key design parameters for friction-riveted joints</b>	<b>94</b>
7.1.	Comparison of PEEK-CA30/Ti joints produced using the RSM and RNA systems . . . . .	94
7.1.1.	Monitoring process parameters and torque . . . . .	95
7.1.2.	Geometry of the rivet anchoring zone . . . . .	96
7.1.3.	Quasi-static mechanical performance . . . . .	97
7.2.	FricRiveting of fabric-reinforced PEEK/grade 3 Ti joints . . . . .	98
7.2.1.	Adjustment of the optimised process parameter set for composite PEEK laminates . . . . .	99



7.3. Evaluation of key design parameters . . . . .	102
7.3.1. Influence of edge distance on joint mechanical performance .	103
7.3.2. Influence of rivet clamping torque on joint mechanical performance . . . . .	106
7.3.3. Influence of specimen width on joint mechanical performance	108
7.4. Failure mechanisms . . . . .	110
7.5. Mechanical performance of friction-riveted and state-of-the-art mechanically fastened joints . . . . .	115
7.6. Summary and conclusion . . . . .	118
<b>8. Final remarks</b>	<b>120</b>
<b>9. Recommendations for future work</b>	<b>123</b>
<b>Bibliography</b>	<b>124</b>
<b>Appendices</b>	<b>i</b>
<b>A. Appendix</b>	<b>ii</b>
<b>B. Appendix</b>	<b>vii</b>
<b>C. Appendix</b>	<b>xi</b>
<b>D. Appendix</b>	<b>xvi</b>
<b>E. Appendix</b>	<b>xxii</b>
<b>F. Appendix</b>	<b>xxiv</b>
<b>G. Appendix</b>	<b>xxvii</b>



# List of symbols and abbreviations

AA2024	aluminum alloy 2024
ANOVA	analysis of variance
$AR$	aspect ratio
AZ	anchoring zone
$B$	hight of the anchoring zone
BM	base material
BO	burn-off
BOR	burn-off rate
CBM	composite base material
CFRP	carbon fibre reinforced polymers
CHAZ	composite heat affected zone
CSZ	composite stir zone
CTMAZ	composite thermo-mechanical affected zone
$d$	fastener diameter
$D$	initial diameter of the undeformed rivet
DoE	design of experiments
$e$	edge distance
$E_{mech}$	mechanical energy input
EBSD	electron backscatter diffraction
$e_{mush}$	mushrooming efficiency
$F$	force
$F_{bru}$	ultimate bearing strength

FRP	fibre reinforced plastic
FoP	forging pressure
FoT	forging time
$F_{pull-out}$	pull-out force
FricRiveting	friction riveting
FP	friction pressure
FT	friction time
$F_{tu}$	ultimate tensile strength of the rivet base material
GF-PEI	glass fibre reinforced polyetherimide
HAB	high angel boundary
HT	heating time
$H$	penetration depth of the metallic rivet
5HS	5-harness satin weave
HV	Vickers hardness
ICJ	injection clinching joining
IR	infra red
$J$	joint efficiency
JP	joining pressure
JT	joining time
$k$	force per hole factor
$L$	length of the specimen
LAB	low angel boundary
LOM	light optical microscopy
$M$	torque
MFZ	metal friction zone
MHAZ	metal heat affected zone
MTMAZ	metal thermo-mechanical affected zone

NDT	non-destructive testing
$P$	ultimate tensile force
PEEK-CA30	polyether ether ketone reinforced with 30 % short carbon fibres
PEEK	polyether ether keton
PEI	polyetherimide
PHAZ	polymer heat affected zone
$P_i$	force at the i-th data point
P	phase
$P(r)$	normal friction pressure
PTMAZ	polymer thermo-mechanical affected zone
$Q_{total}$	total heat input
RS	rotational speed
SEM	scanning electron microscope
$T$	penetration depth
$t$	laminar thickness
$T_{end}$	temperature at the end of the first decomposition step
$T_g$	glass transition temperature
TGA	thermogravimetric analysis
TiAl6V4	titanium grade 5
Ti	titanium
$T_m$	melting point
$T_{onset}$	decomposition onset temperature
TPCL	thermoplastic consolidated laminate
$T_{peak}$	temperature at the maximum reaction rate
$V_{dp}$	volume of the dislocated polymer material
$V_{lp}$	volume of the remaining polymeric material above the deformed rivet tip

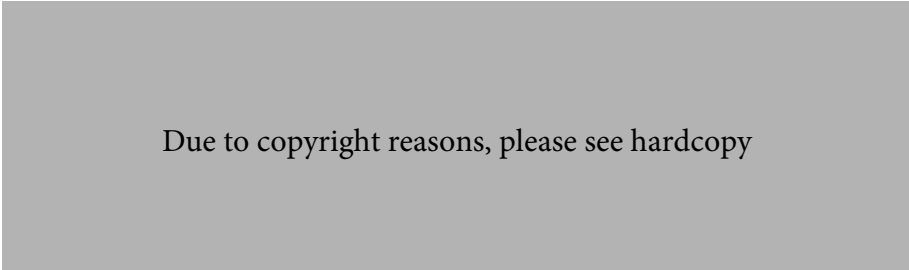
$V_{max}$	maximal tangential speed of the rivet
$V_{riv}$	volume of the deformed metallic rivet
VR	volumetric ratio
$w$	deformed width of the rivet tip
$w$	joint width
$W$	maximal diameter of the deformed rivet tip
$w/d$	width-to-diameter ratio
$x$	axial displacement
$\omega$	angular velocity
$\mu$	kinetic friction coefficient
$\eta$	polymer viscosity in the molten state
$\sigma_i^{br}$	bearing stress
$\epsilon_i^{br}$	bearing strain
$\delta_i$	extensometer displacement
$\sigma_{net-ten}$	ultimate joint strength

# 1. Introduction

## 1.1. Motivation

One of the major challenges our society has to cope with is the contradiction between population and economic growth on the one hand and the limitation of resources on the other. Over the years, topics such as environmental protection and energy efficiency have received increasing attention, while at the same time the availability of products and the mobility of people become more important. The transportation industry is driven by various challenges, such as cost-saving requirements, new environmental protection regulations and the significant growth of transport volumes. One approach to tackling these challenges is the development of new, improved transportation vehicles that use new materials and innovative joining technologies. Therefore, transportation industries such as the automotive and aircraft industries are increasingly making use of fibre-reinforced materials. Figure 1.1 shows the material breakdown of the new A 350 aircraft. It will contain more than 50% composite materials [1]. Nevertheless, composite materials also have their drawbacks. Thermoset carbon fibre-reinforced polymers (CFRP), extensively used in primary aircraft structures, are highly sensitive to impact damage. This will become a major issue for airlines regarding recycling because the thermoset matrix cannot be remelted, so that the fibres remain glued in the matrix. Some of these disadvantages can be avoided by using thermoplastic composites. These materials show improved impact behaviour along with good recyclability.

Over the past years the use of thermoplastics and fibre-reinforced thermoplastics has increased significantly in the transportation industry, for instance in automotive and aircraft structures, and in other high-performance engineering applications such as wind-energy engineering applications, sporting goods and medical technology [2].



Due to copyright reasons, please see hardcopy

**Figure 1.1.** New A 350-900XWB including the material breakdown [1]

The advantages of using thermoplastic composites are their high fracture toughness, better environmental resistance and recyclability [2–4], but one of the main reasons for moving from purely metallic toward composite multi-material structures is the possibility of tailoring their performance to requirements [4, 5].

The increased presence of thermoplastic parts in large structural components raises the question of adequate joining techniques for multi-material structures [6]. Today thermoplastics and reinforced thermoplastics are joined using several techniques. These can be divided into three main groups: mechanical fastening, adhesive bonding, and welding [6–10]. The design of large complex structures with new materials leads to new material combinations requiring new joining technologies [5, 11]. There are also new, innovative joining technologies available for joining thermoplastic composites, such as induction- and resistance welding [12–15], laser-bonding [16], friction spot joining [17, 18] and injection clinching joining (ICJ) [19–21]. These joining technologies exploit the property of thermoplastic matrices that they can be reheated or remelted and consolidated repeatedly [13, 15, 16].

An alternative and very promising joining technology is friction riveting (FricRiveting see section 2.2), a friction-based spot-joining process, first patented by Helmholtz-Zentrum Geesthacht [22, 23]. FricRiveting bridges the gap between mechanical fastening and welding, and offers certain advantages such as short joining cycles and little requirement for surface pre-treatment of the joining partners, and it also reduces the number of installation steps, since no pre-drilling is needed [24]. FricRiveting was developed for joining thermoplastic-lightweight alloy structures. Earlier studies on FricRiveting of unreinforced polyetherimide (PEI) and aluminium AA2024 [24, 25] have successfully demonstrated the feasibility of metallic-insert joints. As this is still a very new process, there is still a lack of knowledge in terms of the effect of the process parameters on the process outcome, the range of materials that can be joined using this technology and the possibilities and limitations of the process regarding future application fields. Following these three points, the present work aims to fill these knowledge gaps by demonstrating the feasibility of friction riveted multi-material joints made of carbon fibre-reinforced PEEK and titanium. The effect of the process parameters on the joint formation and the mechanical performance is an important subject addressed in this work. In order to assess the possibility for structural applications, the design and analysis of friction riveted single-lap shear joints fulfilling aircraft industry requirements, such as high strength and non-catastrophic failure, was also investigated.



## 1.2. Objectives

The focus of the present work is mainly on the feasibility of the FricRiveting process on carbon fibre-reinforced PEEK and titanium hybrid joints. It is intended to close the knowledge gap regarding the detailed explanation of the effect of the process parameters on the process outcome, represented by the joint formation mechanisms and the mechanical performance of the joint. Therefore three key aspects have been identified:

- The development of the FricRiveting process for the application on titanium/carbon fibre-reinforced polymer hybrid joints.
- The investigation of the relationships between the joining process, the microstructure and the mechanical performance.
- The determination of the key design parameters for friction riveted single lap shear joints to fulfil aircraft industry requirements.

Therefore this work intends to establish and explain the fundamental joint characteristics of the FricRiveting process on multi-material joints for future aircraft structures.

## 2. State of the Art

### 2.1. Joining of composites

Joining is the essential step when designing and manufacturing a structure or a product since they can almost never be fabricated in one piece. Therefore the performance of a structure or a product strongly depends on the performance and efficiency of its joints [26]. The main reasons for structures to have joints are [5, 11, 12]:

- to allow the manufacturing of large-sized components, and the assembly of a structure on site
- to achieve geometrical complexity and provide the product with a functionality that could not be obtained using primary processing methods such as casting, forging or forming
- to fulfil the requirements for inspection, ensure accessibility and the possibility of repair
- to achieve structural efficiency by using a joining process that adds material only at the location where it is actually needed
- to optimise the use of materials by adding material rather than removing it, for example by milling, which can lead to significant loss of material
- to allow the production of hybrid structures composed of dissimilar materials, where a specific material can be used at the required location.

The two major challenges when joining composite materials are, firstly, to achieve mechanical, physical or chemical compatibility between the joining partners (which concerns the composite matrix), and secondly to protect the fibre reinforcement along the joint [5].

Basically, there are only three ways to join material components: the technology must use either mechanical, chemical or physical force [5, 11]. In the case of mechanical force, which is the basis of mechanical fastening, the joining partners remain separate and distinct at the atomic or molecular level, and no chemical bonds are formed. The joining partners are held together by physical interlocking or interference to macroscopic or microscopic features, and a third object is used to keep the parts together, such as a rivet, bolt, screw etc. When the technology uses chemical forces, the joining partners are kept together by the formation of chemical bonds resulting from a chemical reaction. When the technology relies on physical forces,

the bond is created by the natural tendency of atoms, ions and molecules to attract each other so that no chemical reaction is required [5, 11].

The joining technologies available for composite materials can be divided basically into three categories [5, 6, 11]. Firstly, mechanical joining, where strictly mechanical forces are applied by fasteners to create physical interference and interlocking. Secondly, adhesive bonding, where chemical forces are used to bond materials at the atomic level with the help of chemical agents. Thirdly, welding, which relies on the natural tendency of atoms to bond using physical forces with their origin in electromagnetic effects, using heat and/or pressure [5, 11]. Additionally, there are hybrid joining processes which represent combinations of these individual technologies [11]. The most common hybrid joining process is the combination of adhesive bonding and mechanical fastening [27]. The main technologies available today for joining composite materials are discussed in the following sections.

### 2.1.1. Mechanical fastening

In composite structures, mechanical fastening is still one of the most commonly used joining technologies [27]. This method usually allows dissimilar materials to be joined, using only interference or interlocking at a microscopic or macroscopic level to hold the joining partners together. The technology requires a third component (the fastener) to cause interference between the joining partners – for example, rivets, bolts, screws etc. [5, 11].

For mechanically fastened joints, the selection of the optimum joint geometry and the material are important for the structural integrity and reliability of the composite structure [27]. The performance of the joint and the occurrence of a specific failure mode mainly depend on the joint geometry and the laminate configuration, or lay-up [28]. The main design parameters to be considered when designing a joint in composite material are the fastener diameter ( $d$ ), the laminate thickness ( $t$ ), the edge distance ( $e$ ), the width of the joint ( $w$ ) and the clamping torque of the fastener [29].

The commonly observed failure modes of single-bolt joints are shown in Figure 2.1. Figure 2.1 a-c shows the basic failure modes, which are net-tension, shear-out and bearing failure. Tear-out and cleavage failure are shown in Figure 2.1 d and e; these are secondary failure modes which occur only after an initial bearing failure [27]. Only two of these failure modes, bearing failure and net-tension failure, are considered desirable. The other failure modes are regarded as premature failures at lower loads [29]. Bearing failure is generally preferred to net-tension failure since it progresses slowly, allowing it to be detected before ultimate failure. Due to the non-catastrophic nature of bearing failure, it often has less serious consequences for the structure than the other failure modes [30]. Therefore, bearing failure will also be the preferred failure mode for friction-riveted composite-composite joints. Net-tension, shear-out and cleavage failure occur suddenly and are therefore considered to be catastrophic failures [27, 31]. The distinction between bearing and net-tension

failure mainly depends on the geometry of the joint, especially the width to diameter ratio ( $w/d$ ) [29]. When the width to diameter ratio increases and the edge distance is large enough, the failure mode changes from tensile to bearing failure [31]. If the edge distance is too small, the joint fails in the shear-out or cleavage mode. Increasing the edge distance when  $w/d$  is sufficiently large, changes the failure mode from shear-out failure to bearing failure [31].

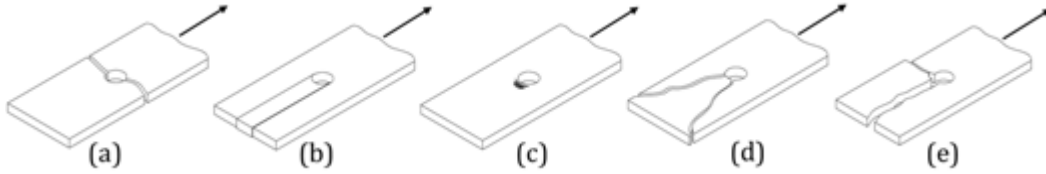


**Figure 2.1.** Most commonly observed bearing failure modes, adapted from [27,32]: (a) net-tension or tensile failure; (b) shear-out failure; (c) bearing failure; (d) tear-out failure; (e) cleavage failure

State-of-the-art mechanical fastening are not considered to be a permanent joining technology since the fasteners can be removed without damaging the parts. The possibility of disassembling such joints can simultaneously be seen both as an advantage and a problem [5]. The main advantages of mechanically fastened joints are: no special surface preparation required, inspection by direct observation is usually possible, good resistance to out-of-plane loading, and lower sensitivity to environmental degradation than bonded joints [5].

The major disadvantages of this joining technology are the unavoidable presence of stress concentrations at the holes required for the fasteners; the possibility of galvanic corrosion of the fastener by the composite; and the weight penalty due to the fasteners, inserts or doublers [5].

### 2.1.2. Adhesive Bonding

Adhesive bonding offers the possibility of joining almost all materials and material combinations. It is a relatively mature and widely used technology for joining composite materials in structural applications [6]. Adhesive bonding uses a substance that holds the joining partners together by surface attachment. The joining partners are termed adherends; the bonding substance is an adhesive, a chemical agent that uses chemical forces to bond the joining partners together. This chemical bond is often the result of a chemical reaction, and can also cause mechanical interlocking at the microscopic level between the adhesive and the adherends, at least in the case of porous or rough-surfaced adherends [5]. The load in bonded joints is transferred by shear, which means that the joint configuration and the size of the bond area are of particular importance. The favoured joint configuration is the lap joint, where the joint strength can be increased by increasing the overlapping bonding area until it is sufficient to transfer the shear load [33].

The use of adhesively bonded joints provides numerous advantages, such as the very limited alteration of the chemical composition and microstructure of the joining partners, the possibility of joining dissimilar materials, the ability to produce large bearing areas and the tendency to distribute loading evenly. These joints also result in little, if any, weight penalty for the structure and a lower sensitivity to cyclic loading (fatigue) due to lower stress concentrations and better strain accommodation. It also produces smooth external surfaces which are beneficial for the aerodynamics and the appearance of the part. Additional benefits of adhesive bonding include the sealing capability and therefore the absence of galvanic corrosion problems between dissimilar materials, offering the possibility of producing permanent joints [5, 34, 35].

The major weakness of composite bonded joints is their susceptibility to degradation by environmental factors such as extreme temperature, solvents, moisture, salt, ultraviolet light and other radiation [5]. Additional problems associated with the use of bonded joints include complex and time-consuming surface pretreatment, intensive process control, difficulty in repairing or servicing introduced damage, and complex inspection procedures, except by indirect, nondestructive methods. Also, bonded joints are very difficult or impossible to disassemble without damaging the joining partners. Prediction of the failure mode of such joints is complicated by the often complex structure and the failure mechanisms [5, 34].

The types of failure modes that can occur during the mechanical testing of bonded fibre reinforced plastic (FRP) joints is described in ASTM D5573-99 [36] and summarised in Figure 2.2. The main failure modes observed in bonded composite structures are defined below.

- Adhesive failure (Figure 2.2 a) is a form of failure in which separation of the joined materials occurs at the interface between the adhesive and the adherend. The surface of the adhesive and the FRP joining partners might have a shiny appearance, which indicates that no material transfer had taken place between the adhesive and the FRP.
- Cohesive failure (Figure 2.2 b) is the mode in which the failure occurs within the adhesive, such that a layer of the adhesive is found on both adherends following failure.
- Thin-layer cohesive failure (Figure 2.2 c) is similar to cohesive failure, except that it occurs very close to the FRP-adhesive interface, with one adherend showing only traces of the adhesive at the surface, whereas the other shows a thicker layer of adhesive.
- Fibre-tear failure (Figure 2.2 d) occurs only in the adherend, with the result that reinforcing fibres appear on both failure surfaces.
- Light-fibre-tear failure (Figure 2.2 e) occurs within, and close to the surface of the FRP. The mode is characterised by a thin layer of FRP resin matrix on the adhesive containing few or no fibres.

- Stock-break failure (Figure 2.2 f) is a mode where the FRP substrate breaks outside of the bonding region, but often in close proximity to it.

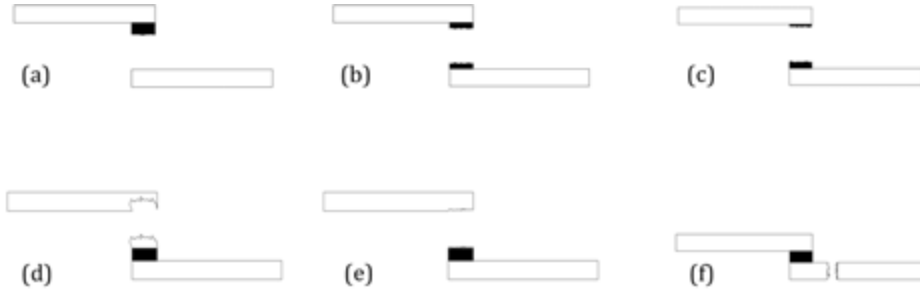


**Figure 2.2.** Commonly observed failure modes for adhesive bonded joints, adapted from [36]: (a) adhesive failure; (b) cohesive failure; (c) thin-layer cohesive failure; (d) fibre-tear failure; (e) light-fibre-tear failure; (f) stock-break failure

### 2.1.3. Welding

In contrast to bonded joints, welded joints normally do not require any chemical reaction to take place during the joining process. The welded joints rely solely on the natural tendency of atoms, ions or molecules to be attracted by each other [5]. In welding, the bonds formed are strong primary bonds in comparison to adhesive bonding where the bonds are weaker secondary (e.g. van der Waals) bonds. Thus welded joints are the most permanent of all joints, since the bonds formed in the joining region are similar to the bonds found inside the base material itself. These joints can only be disassembled by severely damaging the joining partners [5, 11].

Joining by welding is well known in the thermoplastics industry. The joint efficiency has been shown to be close to that of the base material. Although welding technologies are well known, they are not well understood – especially regarding the effect of the process parameters on the mechanical performance of the joints [6]. Welded joints, like bonded joints, do not have the issue of stress concentrations at the holes necessary for mechanical fastening. Moreover, welded joints also offer shorter processing times and less surface preparation [12]. The welding technologies available for polymers or polymer composites are manifold and can be divided into three classes depending on the technology used to introduce the welding heat. The first is thermal welding, including hot-gas welding, extrusion welding and hot-tool welding. Friction (mechanical) welding, such as ultrasonic welding, vibration welding and spin welding, forms the second group. The third classification is electromagnetic welding – resistance welding and induction welding [6, 12]. A description and review of these welding technologies is not intended in this work; further information can be found elsewhere [6, 12–14, 37].

The main advantage of welded joints is their high structural integrity and efficiency. They are also the most permanent joints, which is both an advantage and a disadvantage. This joining process leads to changes in the composition, microstructure and properties of the materials in the joining region, which is seen as the greatest shortcoming of welded joints [5, 11].

#### 2.1.4. Hybrid joining

It is also possible to combine the abovementioned primary joining technologies (mechanical fastening, adhesive bonding and welding) in order to obtain joints having properties suited to specific purposes. Currently, the joints produced with hybrid joining methods utilise a combination of resistance spot welding and adhesive bonding (weld bonding), or a combination of mechanical fastening and adhesive bonding (rivet bonding) [11].

Most of the research into hybrid joining, although still limited, was found to be on bonded-bolted joints. Kelly [38] showed in his study of bolted-bonded single-lap shear joints that the combination of mechanical fastening and adhesive bonding can be beneficial for specific joint geometries and material combinations. Kelly [39] reported that hybrid joining offers the potential to improve both the strength and fatigue life with respect to adhesive bonded joints; to achieve this, the material selection and the joint design must be carefully combined. More recently, Lee *et al.* [40] reported that the failure loads of hybrid joints were almost identical to those of purely bonded joints, but were at least double the failure loads of mechanically fastened joints.

## 2.2. FricRiveting

FricRiveting is a new and innovative friction-based spot joining process, patented by the Helmholtz-Zentrum Geesthacht in 2007 [22, 23]. The FricRiveting process was introduced by Amancio *et al.* [10, 24, 25, 41–43] who first investigated the friction riveting process applied to unreinforced thermoplastics and aluminium. FricRiveting bridges the gap between mechanical fastening and welding, and offers advantages such as short joining cycles and minimal surface pretreatment of the joining partners. It also reduces the number of installation steps, since no pre-drilling is required [24].

### 2.2.1. Characteristics of the technology

The process can best be explained by considering the most basic friction-riveted joint example, the metallic-insert joint, where a metallic rivet is anchored into a thermoplastic base plate. The main process steps are described in Figure 2.3. First, the two joining partners are fixed in the joining equipment, the thermoplastic base plate onto the backing plate and the metallic rivet in the spindle. Subsequently the

rivet starts to rotate and moves towards the thermoplastic base plate and touches down (Figure 2.3 b). The combination of rotation and axial pressure generates frictional heat which leads to a thin layer of molten polymer around the rivet tip. Due to the continuous feed of the rivet during the friction phase, some of the molten material is partially expelled and forms a flash. During this phase, the rate of heat generation increases and the heat input exceeds the heat outflow, due to the very low thermal conductivity of the polymer. The local increase in temperature plasticises the tip of the rivet. At this point the motor brake begins to decelerate the spindle rotation; simultaneously, additional pressure (forging pressure, FoP) is applied (Figure 2.3 c). The molten polymer layer below the rivet tip is suppressed by the additional axial pressure and the tip of the rivet is forged backwards by the revealed solid region, widening the rivet tip until it assumes an inverted parabolic, or mushroom-like, shape. In the last step (Figure 2.3 d) the joint consolidates and cools while constant external pressure is maintained, and the rivet remains strongly anchored in the polymeric plate, forming a metallic-insert joint.

### 2.2.2. Process parameters and variables

The FricRiveting process is controlled by the data input into the riveting system. The data input is managed by the process parameter settings: the rotational speed (RS), joining time (JT) (friction time (FT) and forging time (FoT)), and joining pressure (JP) (friction pressure (FP) and forging pressure (FoP)). A description of the parameter-setting process involved in FricRiveting, and their function, were reported by Amancio-Filho ([25, 43]).

The rotational speed defines the nominal value of the angular velocity of the rivet during the joining process. The rotational speed strongly affects temperature evolution during joining and contributes to the mechanical energy input into the joint, and it is also associated with the viscosity of the softened or molten polymer matrix as well as with the formation of thermal defects and degradation. The friction time represents the duration of the friction phase, and also controls the energy input into the joint and thereby affects the number of volumetric defects and the degree of decomposition as a result of the FricRiveting process. The forging time defines the duration of the forging phase, where additional pressure is applied and the RS approaches zero. The FoT mainly affects the shrinkage by providing constant conditions during consolidation. The friction pressure is the normal force applied to the rotating rivet during the friction phase, which affects the normal pressure distribution at the joining surfaces. The FP contributes also to the energy input and temperature evolution as described for the RS and the FT. The FoP is the additional pressure applied to the rivet as the rotation decelerates, and mainly controls the forging of the rivet and consolidation of the joint.

The output of the FricRiveting process is described in terms of the process variables introduced in [25, 43]. The reported process variables are the heating time (HT),



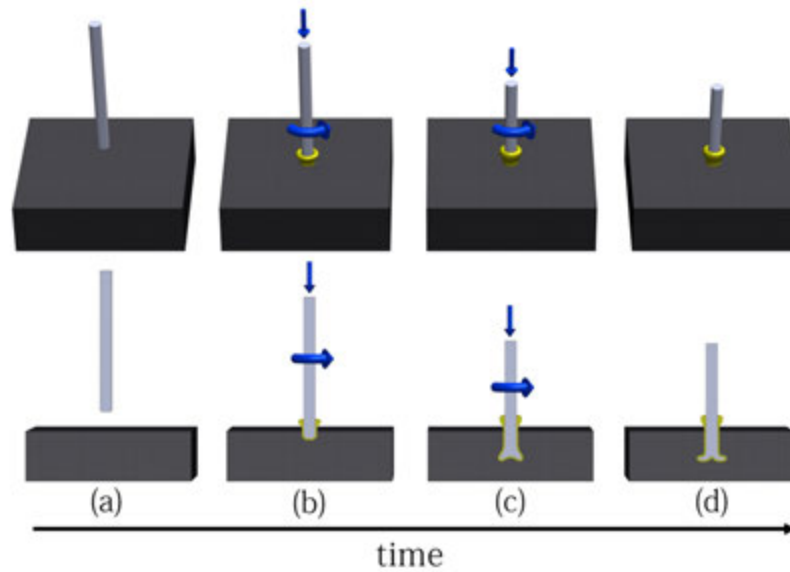


**Figure 2.3.** Friction riveting process steps: (a) positioning of joining parts; (b) frictional heat leads to molten polymer layer and rivet penetrates the polymer; (c) increase of axial force results in anchoring by widening (mushrooming) of the rivet tip; (d) consolidation of the joint

burn-off (BO), burn-off rate (BOR), process temperature and torque. These are defined below.

The HT is the time between the initial contact of the rotating rivet with the surface of the polymer substrate (touchdown), and the end of the process, where the RS approaches zero. The HT is associated with the heat input regime and provides a close estimate of the plasticisation level of the material. It is also an indicator for estimating the extent of structural change occurring due to elevated temperature.

The BO is taken from the axial displacement curve, monitored during the joining process. It represents the displacement between touchdown of the rivet and the end of the joining process, since it is related to the penetration of the rivet inside the substrate and to the deformation (consumption) of the rivet. Together with the HT, the BO provides an estimate of the plasticising level of the rivet caused by the process. The BOR represents the joining speed, and is calculated as the quotient of BO divided by HT (see Equation 2.1). The average process temperature provides information on the changes of the viscosity of the softened or molten polymer. The process temperature, along with the deformation level of the rivet, is directly associated with the energy input. Changes in the local properties and the microstructure of the joining area are correlated with temperature evolution during the riveting process. The torque evolution during joining is used to estimate the rheological behaviour of the molten polymer and the plasticising of the metal-

lic rivet. Inconsistencies in the torque evolution indicate abnormalities during the process or malfunction of the joining equipment.

$$\text{BOR} = \frac{BO}{HT} \quad (2.1)$$

### 2.2.3. Joining and monitoring

The FricRiveting process consists of five separate phases, explained in detail in [25, 43]. Figure 2.4 is an example of a monitoring diagram of a friction-riveted joint, including the main FricRiveting process parameters and variables. These process steps are obtained from the process monitoring systems connected to the welding equipment. The rivet begins to rotate and moves toward the composite base plate when the pre-set rotational speed is reached, then touches down at a defined friction pressure corresponding to the beginning of the friction step. Figure 2.4 shows the evolution of the process parameters over time, and an increase in torque and axial displacement related to the penetration of the polymer. The motor brake begins to operate when the friction time is passed and additional pressure (forging pressure) is applied. It is also seen that the increased axial pressure results in an immediate rise in both the torque and axial displacement; this is the forging step. After forging time expires, rotation stops and the joint consolidates, appearing in Figure 2.4 as constant displacement while both pressure and torque decrease. After the FoT is complete, the pressure is released and the joined sample can be removed from the clamping device [25, 43].

### 2.2.4. Process phases

Friction-based joining technologies such as spin welding of plastics are commonly divided into process phases [44]. Analogously, the FricRiveting process is divided into five main process phases associated with the different stages of heat generation and axial displacement of the rivet over the joining time, as shown schematically in Figure 2.5. The phases have been described by Amancio-Filho [25, 43]; the details are explained in the following paragraphs.

Phase P-I is the solid friction, or Coulomb friction, phase in which the necessary heating takes place. In FricRiveting, the solid friction is assumed to be of the polymer–polymer type, where the harder asperities of the metal rivet penetrate the softer polymer. This initial friction phase occurs on a very small scale, and no axial displacement is monitored by the system, as shown in Figure 2.5. Once sufficient frictional heat is generated to soften the polymer matrix (at the glass transition temperature for amorphous polymers, and at the melting point for semi-crystalline polymers) at the faying surfaces, the friction regime changes from a solid to a molten state and the second phase starts.

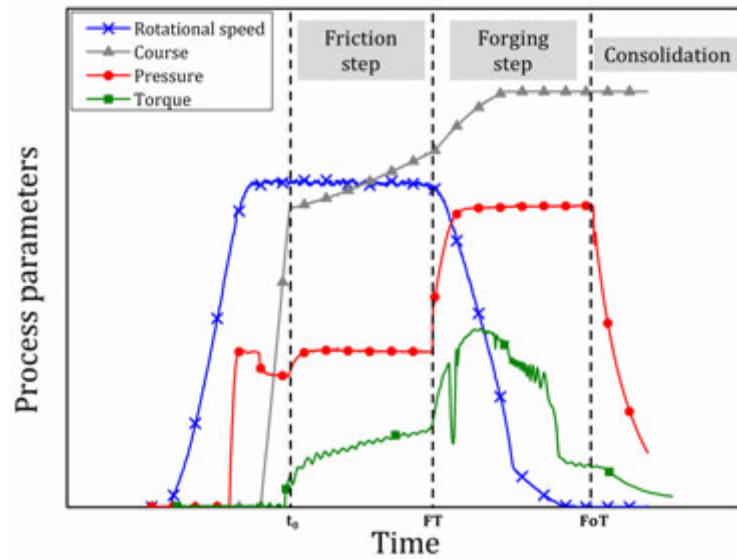


**Figure 2.4.** Typical evolution of friction-riveting process parameters over time. Friction step: Rivet starts to penetrate the polymer/composite so that torque and axial displacement increase with time. Forging step: Increase of axial force leads to a rise in torque and displacement. Consolidation step: Joint cools and attains its final strength

Phase P-II is the unsteady state of viscous dissipation, where frictional heat is mainly generated by internal shearing within the molten polymer. Axial displacement is observed as the rotating rivet begins to penetrate the substrate. Figure 2.5 shows that the axial displacement increases over time in a nonlinear fashion.

Phase P-III Is the steady-state viscous dissipation phase, where a balance is reached between the melting rate of the polymer beneath the rivet tip and the outflow rate of the melted material, which is expelled as flash. The rotating rivet continues to penetrate into the substrate; Figure 2.5 shows that the axial displacement in P-III increases linearly with time. Approaching the end of this phase, the rivet reaches the plasticisation level required for the the next phase of the process.

Phase P-IV is the forging phase, where the rotational speed of the rivet is reduced until it reaches zero and additional pressure (the forging pressure) is applied. Due to the increase in axial pressure, the rivet forces the molten polymer out of the joining region, which increases the amount of expelled flash material; by doing so, the plasticised rivet tip is exposed to solid polymer material, and is plastically deformed by the reactive forces. The tip of the rivet is widened until it assumes a parabolic (mushroom-like) shape. The axial displacement responds to this processes with an immediate increase in the axial displacement rate, see Figure 2.5.

Phase P-V is the consolidation phase, where the rotational speed is zero and the joint consolidates under constant pressure to prevent shrinkage. In this phase the

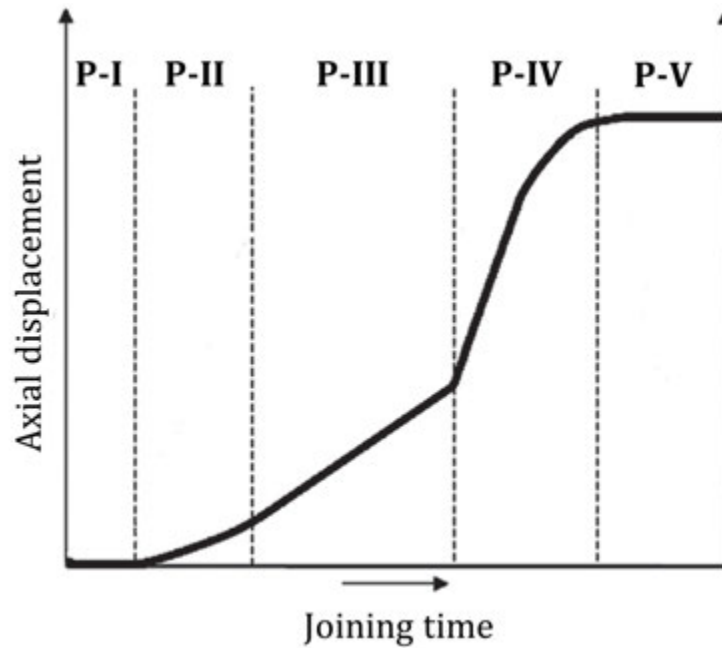


**Figure 2.5.** Schematic indicating the FricRiveting process phases, adapted from [24, 43]. P-I: Coulomb friction (solid friction); P-II: unsteady-state viscous dissipation; P-III: steady-state viscous dissipation; P-IV: rivet forging phase; P-V: consolidation phase

joining process is completed, and the joint reaches its final strength. Figure 2.5 shows that the axial displacement has reached a plateau and remains constant.

### 2.2.5. Mechanical energy input

The heat development regime in friction-riveting is a very complex phenomenon, described by [43] to be related to the heat generated by solid friction (a small proportion, normally less than one percent of the total generated heat) and viscous dissipation (internal shearing of macromolecules) in the melted polymer. A detailed analytical model for the heat input during FricRiveting was proposed and validated for unreinforced thermoplastic/aluminum joints [25]. Although this analytical model enables the total generated heat to be calculated, it requires a precise determination of the process temperature, microstructural changes, shear rates and changes in molten polymer viscosity, increasing the complexity of the model.

The mechanical energy input is often used to estimate heat generation during friction-based welding processes for thermoplastics [44, 45] and metals [46–48]. Considering the similarities to the friction-riveting process, this approach was used to study the influence of frictional heat on the geometrical changes in the rivet anchoring zone and its effect on the tensile strength of the joint. The mechanical

energy input is the energy introduced into the joint by the FricRiveting process in accordance with Equation 2.2 [48, 49]. This consists of two terms, the first describing the energy accumulated due to the torque  $M$  and angular velocity ( $\omega$ ), and the second term corresponding to the energy due to the axial force ( $F$ ) and axial speed ( $v_0$ ). The second term usually makes a much smaller contribution to the total introduced mechanical energy, and may be neglected; thus Equation 2.2 is simplified to Equation 2.3:

$$E_{\text{mech}} = \int M \times \omega dt + \int F \times v_0 dt \quad (2.2)$$

$$E_{\text{mech}} = \int M \times \omega dt \quad (2.3)$$

### 2.2.6. Microstructural zones in the joining region

A FricRiveted metallic insert joint typically consists of five microstructural zones, as described in [25, 43]: the polymer heat-affected zone (PHAZ), the polymer thermomechanically affected zone (PTMAZ), the metal heat-affected zone (MHAZ), the metal thermomechanically affected zone (MTMAZ) and the anchoring zone (AZ) are shown in Figure 2.6. Amancio described the five zones as follows, using metallic-insert joints made of PEI and AA2024 as an example.

The PHAZ is the polymeric zone around the metallic rivet which experiences elevated temperature during the riveting process without reaching the softening temperature ( $T_g$  or  $T_m$ ) of the polymer. This heat-affected region shows changes in its local mechanical properties, although the zone might not be visible. In the case of semi-crystalline polymers such as PEEK, these changes might include crystallisation or the growth of crystallites.

The PTMAZ is the layer of molten polymer around the rivet and is situated between the metallic rivet and the PHAZ (see Figure 2.6). Severe plastic deformation occurs in this zone. The temperature rises above  $T_g$  or  $T_m$  and the polymer may be exposed to higher temperatures, resulting in thermal degradation. These high temperatures may lead to the formation of voids and flaws and to changes in the local mechanical properties. The voids are formed for several reasons, including the expansion of volatiles such as absorbed water, or entrapped air associated with the high viscosity of some molten polymers, or cooling shrinkage due to different thermal expansion coefficients of the polymer and the metal components of the joint, and as a result of thermal or thermomechanical degradation. These flaws play a significant role in the mechanical performance of the joint, and their presence should therefore be reduced in an optimised process.

The MHAZ is the zone of the metallic rivet which is affected by the heat associated with the process but does not undergo plastic deformation: see Figure 2.6. Due to the heat experienced in this region and depending on the rivet material,

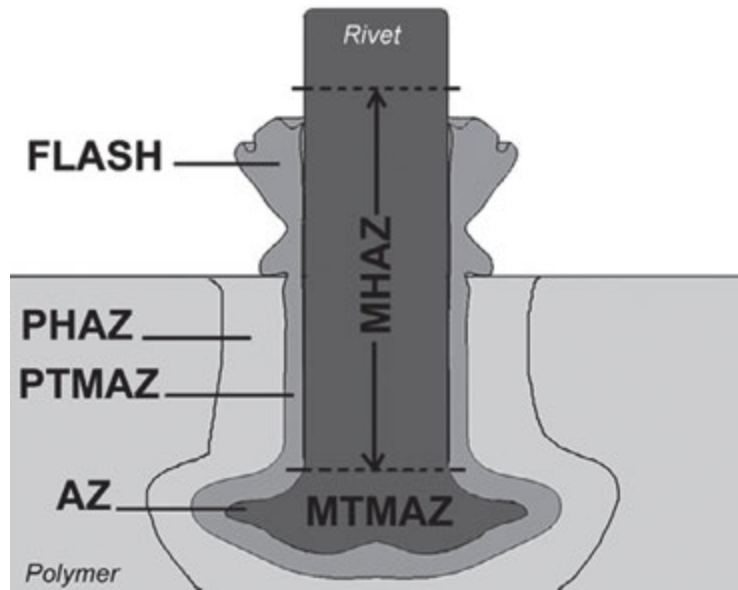


**Figure 2.6.** Schematic representation of typical microstructural zones found in FricRiveted metallic-insert joints, indicating five zones: polymer heat-affected zone (PHAZ), polymer thermomechanically affected zone (PTMAZ), metal heat-affected zone (MHAZ), metal thermomechanically affected zone (MTMAZ) and anchoring zone (AZ) [25, 43]

different annealing phenomena may emerge, such as static recrystallisation, over-ageing and recovering, as well as different hardening mechanisms such as ageing and re-precipitation. Thus the heat in this region leads to severe modification of the structure, a fact which is indicated by microhardness measurements, even in the absence of visible changes in the microstructure when observed by light optical microscopy (LOM).

The MTMAZ is the region at the deformed rivet tip, which is affected by frictional heat and severe plastic deformation. In this zone, dynamic recovery and recrystallisation takes place. The microstructure typically shows grain refinement and grains with sub-grain patterns characteristic of dynamic recrystallisation and recovery.

The AZ is the zone of the deformed rivet tip. The plastic deformation results in a parabolic (mushroom-shaped) anchoring feature inside the polymer substrate, with a diameter greater than that of the initial rivet. This region forms the mechanical interlock (anchoring) and is responsible for the load-carrying behaviour of the metallic-insert joints.

### 2.2.7. Advantages and challenges

Previous studies have indicated that FricRiveting is an innovative joining technology with great potential for industrial applications in numerous fields. The advantages

of the FricRiveting process, which combines the benefits of mechanical fastening and friction welding, are pointed out below [10, 42, 43].

- Little or no surface cleaning or preparation are required, which reduces the number of installation steps.
- The process usually requires access to one side only, allowing joining at locations which are otherwise difficult to access.
- The presence of through holes in the structure is not required prior to joining, which also reduces the total number of installation steps.
- The technology benefits from very short joining cycles (currently 0.5 s to 10 s), reducing the cost per joint.
- A wide range of polymers (thermoplastic and thermoset), composites and light-weight metals can be joined, which indicates the versatility of the technology.
- FricRiveting equipment is commercially available and of low cost. Additionally, the system offers the possibility of being implemented in robotic systems.
- FricRiveted metallic-insert joints and overlap joints show good pull-out tensile and shear performance.

Since every joining assignment comes with its own challenges and no technology can meet all of them all the time, it is always possible to identify drawbacks, depending on the specific application. This also applies for the FricRiveting process. The following drawbacks have been identified [10, 43].

- The technology can be only applied in joining assignments that require a spot-joining process.
- The FricRiveting process requires the polymer or composite substrate to have a minimum thickness that allows the formation of an anchoring feature.
- FricRiveted joints cannot be disassembled.

### 2.2.8. Previous research on FricRiveting

Since its invention in the middle of the year 2000 [22, 23], extensive research on FricRiveting has been carried out at the Helmholtz-Zentrum Geesthacht, a German research centre. The highlights of published results are summarised in this subsection.

The feasibility of FricRiveting has been demonstrated for several material combinations. A basic understanding has grown regarding the influence of the process parameters on the heat generation phenomenon and the process temperature evolution, the pull-out tensile performance of metallic-insert joints and the mechanical performance of lap shear specimens. The feasibility of the FricRiveting process was first demonstrated by Amancio-Filho in his PhD thesis [25]. That work included





- Type II represents the “rivet pull-out with back plug”. In this failure mode the crack nucleates inside the joining area at the deformed rivet tip. Subsequently, the rivet is pulled out of the substrate, leaving behind parts of the deformed rivet tip, or “back plug”. The tensile strength of this failure mode is acceptable but is lower than for Type I.
- Type III, the “full rivet pull-out”, occurs if the degree of deformation of the rivet tip is relatively small, lessening the mechanical anchoring action of the rivet inside the substrate. This failure mode has also been observed in ductile polymers (e.g. polycarbonate [52]). In this failure mode, cracks initiate around the anchoring zone and ultimately the rivet completely pulls out, leaving a hole with a diameter similar to that of the deformed rivet tip. Joints experiencing this type of failure usually fail at tensile force levels lower than those for Types I and II joints.
- Type IV is termed “rivet pull-out” failure, usually observed in joints with a highly deformed rivet tip close to the upper surface of the substrate. In this case the crack nucleates inside the substrate at the outer region of the anchoring zone and propagates toward the upper surface. A conical piece of the polymer breaks free from the substrate but remains attached to the rivet, which is also pulled out of the substrate.
- Type V is “rivet pull-out with secondary cracking” failure, a complex mixed-mode failure that is still not well understood. Cracking begins at a number of sites within the substrate including around the rivet. Initially it resembles Type IV failure until the complete rivet is pulled out of the substrate without the conical polymer piece attached to it. The failed joint is then similar in appearance to a Type III “full rivet pull-out” failure; metallic-insert joints failing in this mode usually have medium- to low tensile strength.

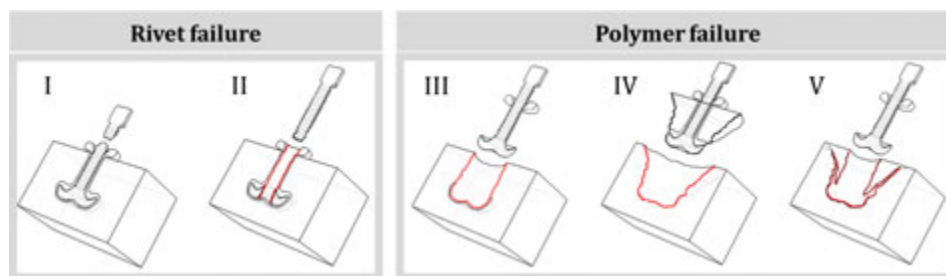


**Figure 2.7.** Previously reported failure modes for the metallic-insert joints, adapted from [51]: I: “through the rivet”; II: “rivet pull-out with back plug”; III: “full rivet pull-out”; IV: “rivet pull-out”; V: “rivet pull-out with secondary cracking” [51–53]

The feasibility of joining glass fibre-reinforced PEI (GF-PEI) and grade 2 titanium using the FriRiveting technology was first demonstrated by [54]. The metallic-insert joints were optimised in order to avoid extensive thermomechanical polymer degradation inside the joined area, resulting in improved mechanical performance.

The optimised metallic-insert joints on GF-PEI/grade 2 titanium led to moderate to good mechanical performance (tensile pull-out force of 1.9 kN – 4.0 kN) compared to the results of previous work on unreinforced polymers such as PEI/AA2024 (average tensile pull-out force 6.1 kN) [43].

Blaga *et al.* [53] and [54] proposed a more precise formulation to describe the mechanical anchoring behavior of friction-riveted metallic-insert joints subjected to tensile loading, developed to overcome the dimensional limitations of the simple aspect ratio formulation proposed by Amancio-Filho *et al.* [24]. The proposed volumetric approach considered all possible changes of width and depth. To obtain a more suitable mathematical formulation for anchoring performance, the following specific volumes were introduced: the volume of the deformed metallic rivet ( $V_{riv}$ ), the volume of the dislocated polymer material ( $V_{dp}$ ) and the volume of the remaining polymeric material above the deformed rivet tip ( $V_{lp}$ ), as shown in Figure 2.8. The figure is a schematic, showing the interactions of the different volumes used to calculate the volumetric ratio (VR), which is a measure of the anchoring efficiency of metallic-insert joints calculated from Equation 2.6, where  $H$  is the penetration depth of the metallic rivet,  $B$  is the height of the anchoring zone,  $W$  is the maximum diameter of the deformed rivet tip, and  $D$  is the initial diameter of the undeformed rivet. This analytical model simplifies the adhesion forces attributed to the contact surfaces between the rivet and the substrate, together with the reactive forces in the substrate material. The model was validated in [52] and [54]; it has been demonstrated to be directly proportional to the ultimate tensile force, and thus gives a reasonable estimate of the pull-out strength of FricRiveted metallic-insert joints [53, 54].

$$VR = \frac{V_{lp}}{V_{dp}} = \frac{(H - B)(W^2 - D^2)}{W^2 H} \quad (2.6)$$

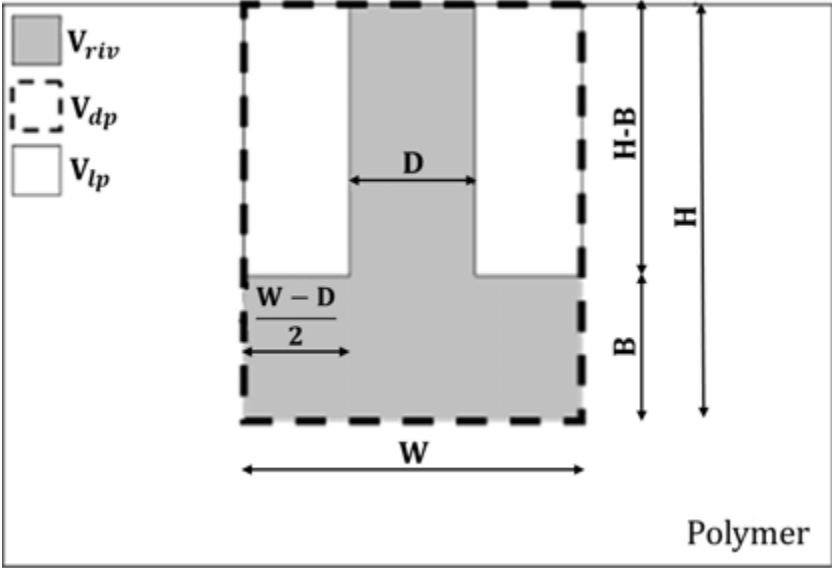


**Figure 2.8.** Geometry of a simplified FricRiveted joint, used to calculate the volumetric ratio (VR), adapted from [53, 54]. The volumes represented in two dimensions are used to calculate VR: the volume of the deformed metallic rivet ( $V_{riv}$ ), the volume of the dislocated polymer material ( $V_{dp}$ ) and the volume of the remaining polymeric material above the deformed rivet tip ( $V_{lp}$ )

### 3. Experimental approach

The methodology chosen for the present work is schematically shown in Figure 3.1. The key aspects of the approach are explained in detail in the following.

In a first step, the feasibility of FricRiveting on unreinforced polyether ether ketone (PEEK) and different commercially available titanium alloys was demonstrated. This step was necessary to identify a suitable rivet material for the following steps, since no previous research had been carried out at that time on the application of the FricRiveting technology to titanium and carbon fibre-reinforced materials. The aim was to identify a titanium rivet material which can be plasticised by the thermal energy imposed by the process. This phase includes the visual inspection and the analysis of X-ray scan radiographs of the metallic-insert joint trials for all of the investigated material combinations. Titanium alloys such as Ti6Al4V and several commercially pure titanium grades were investigated. Preliminary tests of the mechanical performance were also carried out.

For the second step, PEEK reinforced with 30% short carbon fibres and grade 3 titanium was used to investigate joint formation mechanisms and the mechanical performance of metallic-insert joints. To increase the level of statistical confidence in the results, full factorial design of experiments (DoE) and analysis of variance (ANOVA) were conducted. This methodology provided the possibility of studying the effect of the process parameters on joint formation and performance as well as the effect of their combined influences. DoE was additionally used to reveal an optimised process parameter set that would lead to improved widening of the rivet tip and improved mechanical performance. ANOVA tools were used to achieve high reproducibility with reduced standard deviation. Subsequently, the microstructure, local mechanical properties and process-related thermomechanical changes were studied by temperature measurement and thermal analysis.

In the final step, the optimised parameter set obtained for short fibre-reinforced PEEK was adapted for woven fabric-reinforced PEEK laminates using the knowledge gained from the previous step on the effect of the process parameters on the joint formation. These findings were used to tailor the joint formation and achieve high-strength anchoring of the plasticised rivet tip in the woven fabric-reinforced PEEK substrate. A friction-riveted single-lap shear joint was then designed on the basis of an analysis of the influence of the key design parameters (edge distance, specimen width and clamping torque) on the strength of the joint. As a result, an optimised high-strength friction-riveted single-lap shear joint was produced. In order to place the mechanical performance of these joints into context, they were compared to state-of-the-art mechanically fastened joints produced by Airbus.

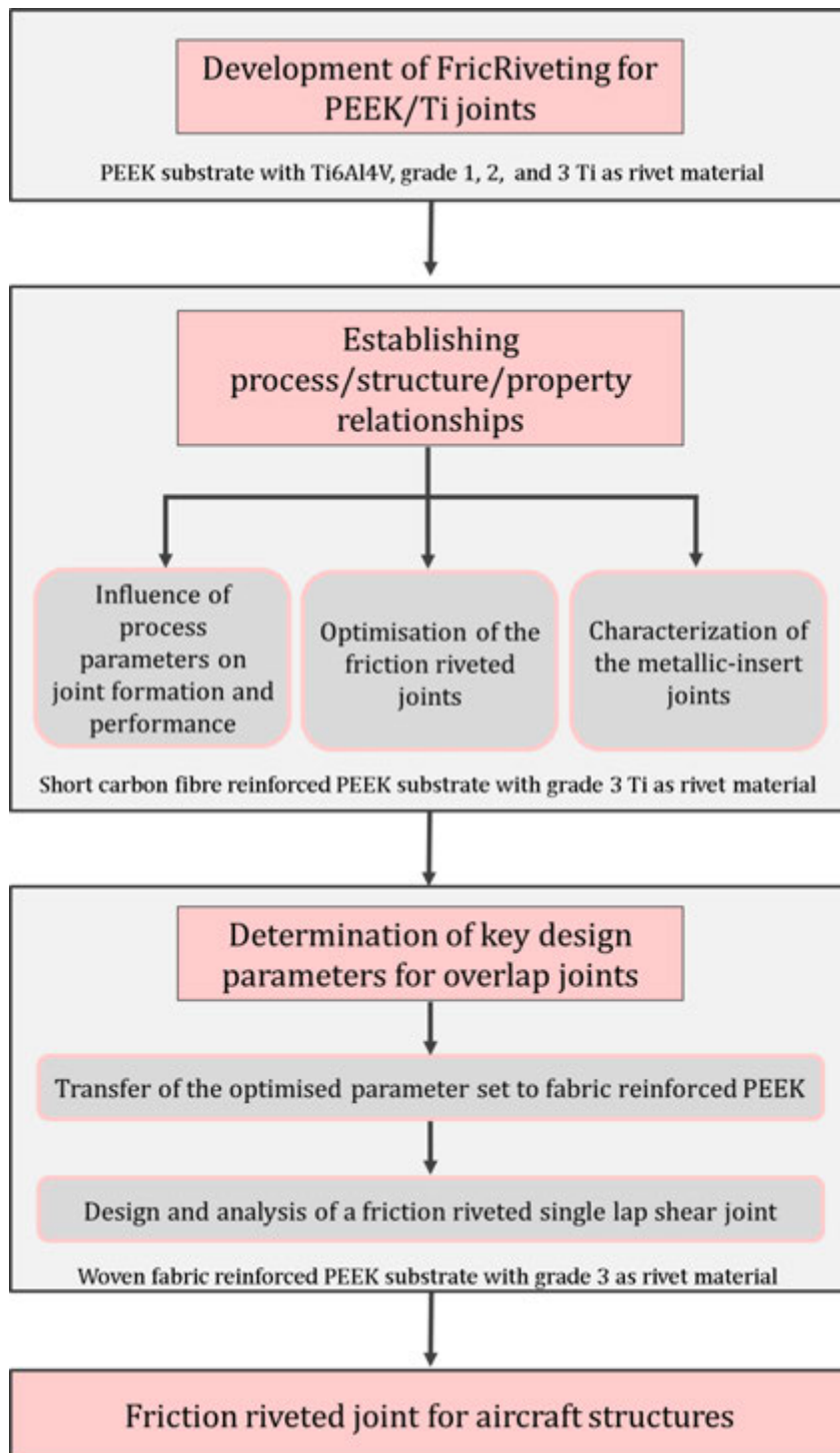


**Figure 3.1.** Schematic view of the scientific approach of the thesis

## 4. Materials and methods

### 4.1. Base materials and specimen geometries

#### 4.1.1. Titanium rivets

Rivets of grades 1, 2, 3 and 5 (TiAl6V4) titanium were used for preliminary tests to demonstrate the feasibility of FricRiveting on PEEK substrate. The mechanical and thermal properties for the titanium rivets are given in Table 4.1. The feasibility study in Chapter 5 below indicated that grade 3 titanium (Ti grade 3), commercially pure titanium, was the material with the best mechanical properties for structural applications, and at the same time offered the possibility of being plastically deformed by available FricRiveting equipment. Therefore all the investigated metallic-insert and lap shear specimens for this work were produced using rivets made of extruded grade 3 titanium rods. The rivets were 60 mm long, with a diameter of 5 mm; see Figure 4.1 a.

**Table 4.1.** Mechanical and thermal properties of titanium grades used in this work [55]

	Tensile strength [MPa]	Thermal conductivity [W/m K]	Melting temperature [°C]
Ti grade 1	240	16.0	1670
Ti grade 2	344	16.4	1665
Ti grade 3	550	19.9	1660
Ti grade 5	950	6.7	1660

Grades 1, 2 and 3 titanium are grades of unalloyed titanium. The chemical composition of grade 3 titanium is shown in Table 4.2. The base material consists only of the alpha phase with a hexagonal close-packed crystal structure [55, 56]. The microstructure parallel to the extrusion direction of the Ti grade 3 is shown in Figure 4.1 b displaying equiaxed alpha grains containing few twins.

Commercially pure titanium has excellent corrosion resistance and a reasonably good strength-to-weight ratio, with the result that it is often utilised to bridge the design gap between aluminum and steel [55]. The strength of grade 3 titanium is comparable to that of the AA 2024 typically used in aircraft applications. The relevant properties of this alloy are listed in Table 4.3. Unalloyed titanium is typi-

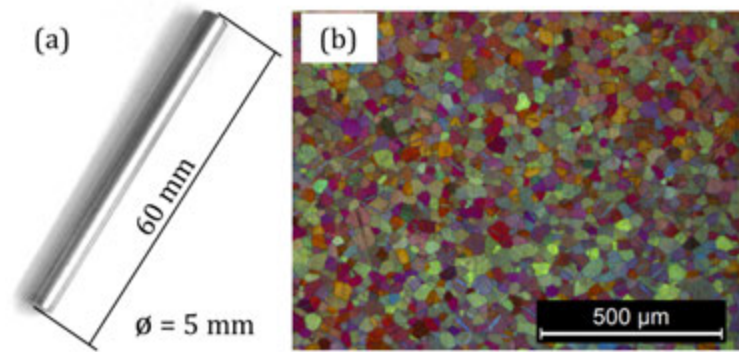


**Figure 4.1.** (a) Geometry of titanium rivet; (b) Microstructure of grade 3 titanium base material, showing equiaxed alpha-grains containing few twins

**Table 4.2.** Nominal chemical composition of grade 3 titanium

Weight [%]	C	H	O	N	Fe	Ti
Ti grade 3	0.07	0.001	0.17	0.01	0.05	BAL.

cally used in non-structural aircraft parts and for engineering applications requiring corrosion resistance [55].

**Table 4.3.** Main properties of grade 3 titanium base material [55–57]

	Ti grade 3
Tensile strength	545 MPa
Tensile modulus	105 GPa
Hardness	235 HV 0.1
Thermal conductivity	19.9 W/m K
Melting temperature	1660 °C

#### 4.1.2. Polyether ether ketone

The feasibility study in Chapter 5 was conducted using polyether ether ketone (PEEK) as the polymeric substrate. The material was supplied by Arthur Krueger Germany with the trade name Ketrone<sup>®</sup> PEEK-1000. Specimens for the substrate were cut with the dimensions 70 mm × 70 mm × 13 mm; see Figure 4.2 a. PEEK is a high-performance semi-crystalline thermoplastic polymer with the molecular structure shown in Figure 4.2 b. PEEK was produced for the first time in 1977 by the ICI laboratories [58]. The relevant mechanical, physicochemical and thermal properties of PEEK are compiled in Table 4.4. The polymer has a very good thermal stability [58–60] due to the aromaticity of its backbones [59]. Furthermore, PEEK

is suitable for aircraft applications because of its low emission of smoke and toxic gases. Being a thermoplastic polymer, PEEK has an indefinite storage life [4,58,60]. It is often selected for engineering applications because of its excellent wear resistance [58,60] and good mechanical performance at elevated temperatures [60,61]. In addition, PEEK is also known for its good degradation and fatigue resistance [58,59] as well as for its high toughness [58] and low moisture absorption. Due to these very good properties, PEEK is applied in different fields such as the automotive and aircraft industries [59] and in the chemical [59] and medical industries [62], being frequently used as a substitute for metals [58,61,62].

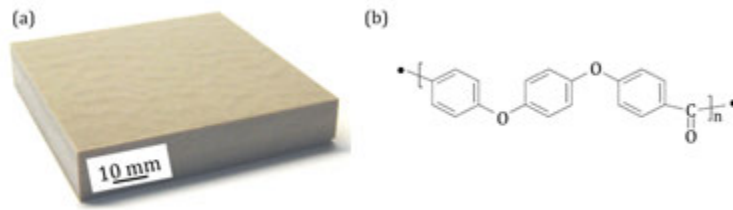


**Figure 4.2.** Polyether ether ketone (PEEK): (a) PEEK substrate used for metallic-insert joints; (b) structure of PEEK, adapted from [63]

#### 4.1.3. Polyether ether ketone reinforced with 30 % short carbon fibres

PEEK containing 30% by weight of short carbon fibres (PEEK-CA30) was used as an intermediate step in the progress toward applying the FricRiveting technology to woven fabric reinforced PEEK laminates. This reinforced polymer was used as described in Chapter 6 to investigate the effect of the FricRiveting process parameters on joint formation and mechanical performance. The material with the trade name Ketron<sup>®</sup> PEEK-CA30 was produced by Arthur Krueger Germany. The base plate geometry (70 mm × 70 mm × 21 mm) is shown in Figure 4.3a and the microstructure of the substrate is shown in a light optical micrograph (LOM) in Figure 4.3b, in which it is seen that the fibres are evenly distributed within the PEEK matrix without a preferred orientation. The LOM image also shows a small

**Table 4.4.** Main properties of polyether ether ketone base material [4,58–61,64,65]

	PEEK	PEEK-CA30
Tensile strength	92 MPa	130 MPa
Tensile modulus	3.8 GPa	7.7 GPa
Hardness	26 HV 0.1	35 HV 0.1
Thermal conductivity	0.25 W/m K	0.92 W/m K
Glass transition temperature	143 °C	143 °C
Melting temperature	334 °C	334 °C



number of pores present in the PEEK-CA30 base material. The most important properties of this short fibre-reinforced thermoplast are summarised in Table 4.4. When comparing the properties of PEEK and PEEK containing 30% short carbon fibres, a significant increase can be observed in tensile strength, modulus and thermal conductivity related to the presence of the short carbon fibres. Neither the melting point nor the glass transition temperature are affected by the addition of the fibres; the hardness undergoes only minor changes, increasing from 26 HV 0.1 to 35 HV 0.1. Typically, the addition of the short carbon fibres results in improvements to wear resistance [64], stiffness, strength and hardness [59,61,66]. The combination of these properties makes this material of interest for a wide range of applications, including the automobile and aircraft industries [66,67], the medical industry for use in orthopedic implants [62] and the chemical industry [67].

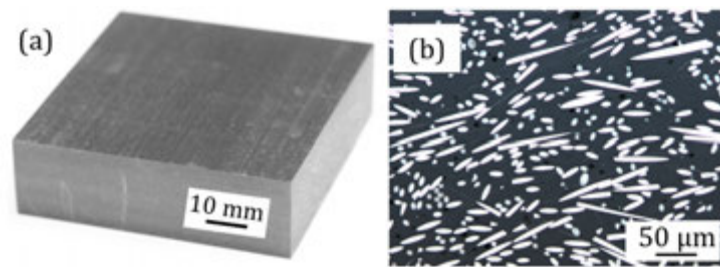


**Figure 4.3.** Short carbon fibre-reinforced PEEK base plate: (a) base plate geometry; (b) LOM microstructure image of Ketron<sup>®</sup> PEEK-CA30

#### 4.1.4. Woven fabric-reinforced polyether ether ketone laminates

PEEK reinforced with woven carbon fibre fabric (TPCL PEEK) was used to demonstrate the relevance and the potential of the FricRiveting technology for structural joining assignments in aircraft structures. The material used was the composite laminate Tenax<sup>®</sup>-E TPCL PEEK-HTA40 produced by Toho Tenax Europe GmbH, Germany. The material is a thermoplastic consolidated laminate (TPCL) made of 14 plies of thermoplastic powdered woven fabric with a thickness of 0.31 mm. The fabric is a 5-Harness Satin Weave (5HS) and consists of high-tenacity carbon fibres, Tenax<sup>®</sup>-E HTA40 E13 3K 200tex, with an average diameter of 7 µm and a PEEK matrix. The TPCL PEEK has a fibre content of 58 wt%. The stacking sequence of the laminate is  $[[ (0, 90) / (+45, -45) ]_3 / (0, 90) ]_s$ , resulting in a thickness of 4.34 mm. The geometry of the TPCL PEEK base plate is shown in Figure 4.4 a; the microstructure of the base material can be seen in Figure 4.4 b.

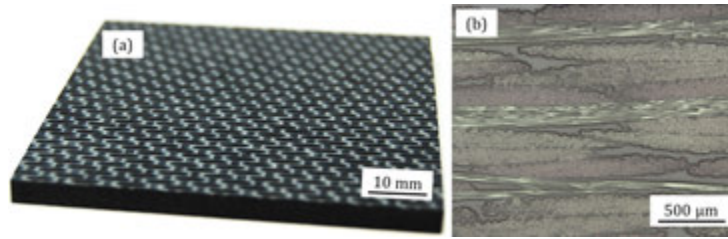


**Figure 4.4.** Woven carbon fibre fabric-reinforced PEEK base plate: (a) substrate geometry; (b) LOM image of the microstructure of Tenax<sup>®</sup>-E TPCL PEEK-HTA40 laminate

**Table 4.5.** Main properties of TPCL PEEK-HTA40 base material [68]

	TPCL PEEK
Tensile strength	963 MPa
Tensile modulus	60 GPa
Compressive strength	725 MPa
Compressive modulus	59 GPa
Melting point	343 °C
Glass transition temperature	143 °C

## 4.2. Friction riveting equipment and joining procedure

### 4.2.1. Joining equipment

In this work two different joining systems were used. The joining equipment used for the feasibility study and the process optimisation was the RSM 400 developed by Harms & Wende GmbH & Co. KG, Hamburg, Germany. The RSM 400 was initially developed as a friction welding head to join aluminum, steel and cast and sintered materials [69] and was therefore only calibrated within the friction pressure range 0.3 MPa to 0.6 MPa. The materials investigated during this study required friction pressures up to 0.9 MPa. As a result, the equipment was modified by installing a differential pressure switch to allow additional higher friction pressures to be calibrated, and reproducible results were obtained for the whole friction pressure range within the power spectrum of the RSM 400. The welding head had a maximum rotational speed of 23000 rpm, nominal power of 1.8 kW and maximum axial force of 6 kN (corresponding to manometric machine pressure of 10 bar or 1 MPa). Additionally, the welding head was equipped with a fully automatic chuck to clamp the metallic rivets [69, 70]. The equipment consisted of the welding head, the RSM 400, a torque measurement platform with a sample holder for clamping the polymer and composite substrates (Figure 4.5), together with a switch cabinet and control panel. The customised torque measurement platform (measurement range from 0–25 Nm) was developed by H. Loitz-Robotik, Germany. Measurement of the torque associ-

ated with the rivet rotation and insertion, which was later utilised to calculate the mechanical energy input, was directly achieved by a piezoelectric sensor inside the backing plate in combination with a load amplifier.

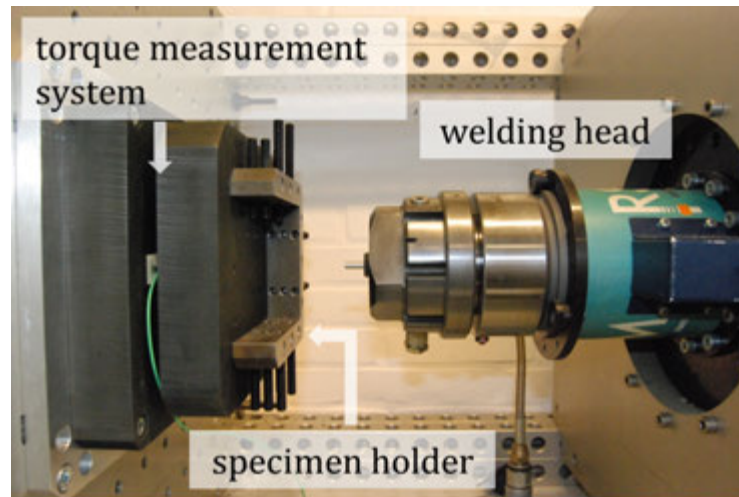


**Figure 4.5.** RSM 400 welding system used to produce friction-riveted multi-material joints

The second item of joining equipment for composite laminate joints was the newly-built RNA equipment, developed by the Helmholtz-Zentrum Geesthacht in cooperation with H. Loitz-Robotik, Germany. The construction and commissioning of the RNA system was carried out within the framework of this PhD thesis. The main reasons for developing new riveting equipment were the limited power of the RSM 400, the limitations of the monitoring sensors and the size of the working room. Moreover, the new RNA system allowed very precise control of the penetration and forging of the rivet, which was fundamental for avoiding mechanical damage to the thin substrates. The new FricRiveting system, shown in Figure 4.6, consisted of a triaxial gantry system, a welding head RSM 410 from Harms & Wende GmbH & Co. KG, Hamburg, Germany, and several sensors. The welding head had a maximum rotational speed of 21000 rpm, a maximum axial force of 24 kN and a maximum axial torque of 20 Nm. The backing plate, positioned on a movable table, measured 1000 mm  $\times$  1500 mm. The maximum vertical travel of the welding head was 1000 mm, which defined the working space. The system was also equipped with sensors to monitor force, torque and displacement, integrated to allow improved process control and a high degree of repeatability in processing. This arrangement makes it possible to join large components as well as high-strength materials. Another major improvement was the implementation of different joining-process control-variants, such as force- and displacement-control, which were essential for joining thin structures.

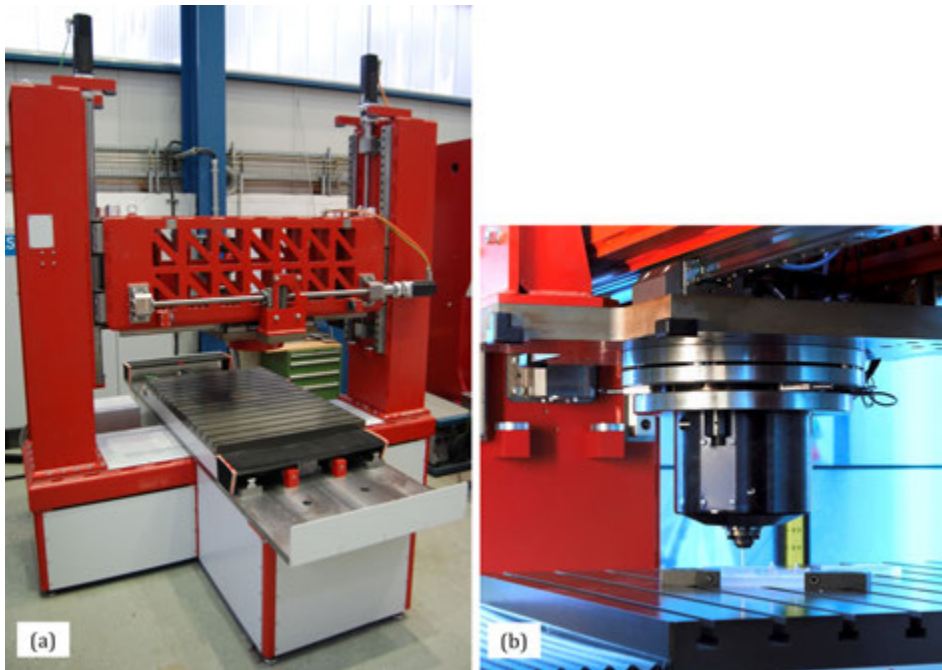


**Figure 4.6.** RNA FricRiveting system: (a) triaxial gantry system; (b) welding head RSM410 from Harms & Wende GmbH & Co. KG, Hamburg, Germany

#### 4.2.2. Friction riveting joining procedure

The joining procedure for all specimens in this work consisted of the following steps. First, the joining partners were fixed in the joining equipment; the polymer or carbon fibre-reinforced polymeric base plates were fixed to the backing plate by the torque measuring system, and the titanium rivet was placed in the spindle chuck. Then the process parameters (rotational speed, friction pressure, forging pressure, friction time and forging time) were set and the riveting procedure was carried out. A detailed description of the joining procedure is given in subsection 2.2.3.

### 4.3. Statistical methods

Design of experiments (DoE) combined with analysis of variance (ANOVA) is a statistical tool which can be used to investigate complex problems involving responses that vary as a function of one or more independent variables. The goal of DoE is to develop a quantitative relationship between factors (input variables) and responses (output variables) [71–73]. The approach was used in this work to gain a better understanding of the FricRiveting process – more precisely, to evaluate the influence of the process parameters on joint formation and mechanical performance. Therefore, the experiments were planned in accordance with full-factorial design, which is more

efficient than a one-factor-at-a-time approach and offers the possibility of evaluating all the effects of the factors on the overall response, as well as quantifying the factor interactions [72,74]. This approach was used to evaluate the effects of process parameters RS, FT, FP and FoP on the joint formation (mushrooming efficiency  $e_{\text{mush}}$ , which is a measure of the anchoring efficiency of the rivet inside the polymeric base plate; the rivet penetration depth ( $T$ ); the mechanical energy input ( $E_{\text{mech}}$ ); and the mechanical performance of the joint when loaded in tension (pull-out force ( $F_{\text{pull-out}}$ )). A schematic of the relationship between the input factors and output factors is illustrated in Figure 4.7.

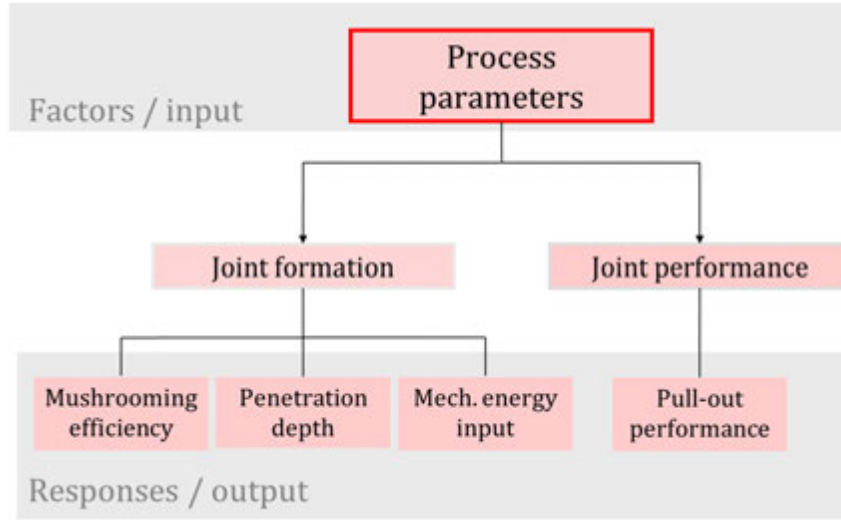


**Figure 4.7.** Schematic of the DoE methodology, showing the inputs and outputs to be evaluated

The concept of the mushrooming effect was first introduced in ballistics to describe the radial widening of cylindrical projectiles due to high velocity impact [75–79]. The mushrooming efficiency is introduced here to describe the deformation and widening of the rivet tip in the FricRiveting process, and is determined from Equation 4.1, which combines the initial rivet diameter ( $D$ ) and the width of the deformed rivet tip ( $w$ ) into a factor that gives the widening of the rivet tip as a percentage of the original width. Since no significant changes of the rivet penetration depth were observed within the parameter range of the investigated process, mushrooming efficiency was used in this study to describe the relationship between the geometry of the deformed rivet and the mechanical performance of the resulting joint. For simplicity, “mushrooming efficiency” was used to estimate the anchoring efficiency, based on the area of contact between the rivet-anchoring zone and the polymer partner.

$$e_{\text{mush}} = 100 \frac{(w - D)}{D} \quad (4.1)$$

#### 4.4. Temperature measurement

The process temperature evolution during FricRiveting was measured by infrared thermography on metallic-insert joints of short carbon fibre-reinforced PEEK and grade 3 titanium. The use of thermocouples was not considered, since their measurement principle is based on direct contact, meaning that high thermal conductivity would be required from the substrate in which the thermocouples would be positioned. Because of the very low thermal conductivity of the composite substrate compared to the metal, thermocouples would have to be placed so close to the rotating rivet that there would have been a high probability of them being destroyed. In such conditions, one could not be confident of obtaining reliable temperature evolution data during the FricRiveting process.

The infrared thermography system used in this work consisted of an ImageIR<sup>®</sup> 8300 thermographic camera (Infratech GmbH, Germany) (see Figure 4.8) and a computer handling the data acquisition and data analysis using the IRBIS 3 Professional software. The distance from the object lens to the touch-down region of the rivet was 321 mm. Measurement was conducted at an incidence angle of 45°. The data acquisition rate was set to 80 Hz and the camera calibration for the temperature range between 150 °C and 600 °C was used.

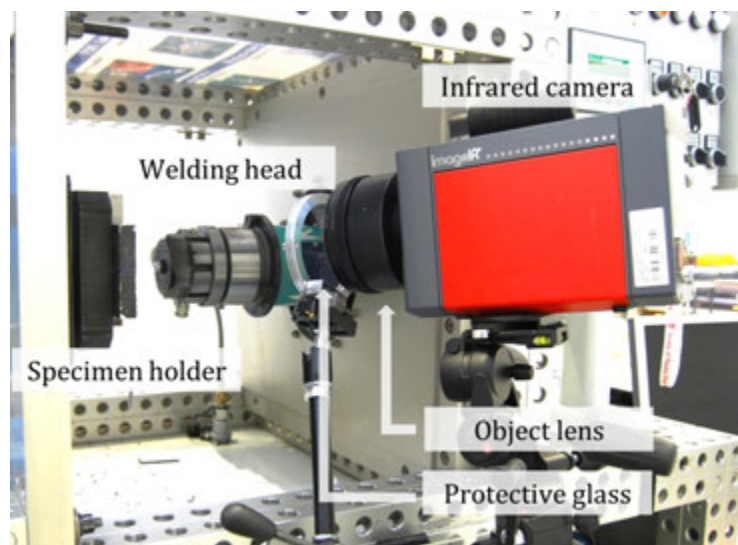


**Figure 4.8.** Setup of infrared thermography system, showing the camera and its positioning, the object lens and the protective glass

The arrangement of the temperature measuring system is displayed in Figure 4.8 which shows the infrared camera and its positioning, the object lens and the protective glass. The temperature evolution was measured from the expelled material accumulating around the rivet during the joining process. It can be assumed that as a result of the low thermal conductivity of the polymer, the expelled material

(flash material) was at almost the same average temperature as the molten polymer layer around the plasticised rivet tip inside the polymer base plate [24, 25, 43].

#### 4.5. Nondestructive testing by X-ray radiography

All of the samples evaluated in this work were non-destructively tested by X-ray radiography prior to mechanical testing and further analysis. X-ray radiography was performed according to standard EN 1435 [80] using a Seifert Isovolt 320/13 with a tube voltage of 60 kV and a tube current of 3.7 mA. The focus-to-film distance was 800 mm and the focal spot was 1.5 mm  $\times$  1.5 mm. This method allowed the geometry and the dimensions of the anchored rivet inside the substrate to be determined precisely without destroying the joint. The X-ray scans provided an exact measurement of the anchoring zone at the centre of the joints where the rivet penetration depth ( $T$ ) and the widening of the rivet tip ( $w$ ) were measured. An example of an X-ray scan with the measured anchoring zone dimensions is shown in Figure 4.9. The addition of this non-destructive testing step provided information about the relationship between the shape and size of the anchoring feature and its mechanical performance; this information was used in calculating mushrooming efficiency.

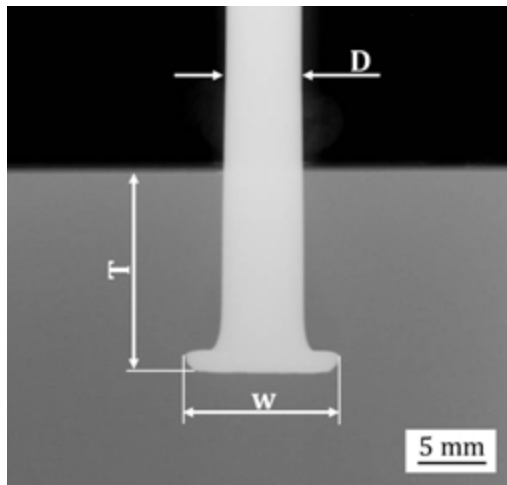


**Figure 4.9.** X-ray radiograph of a metallic-insert joint, indicating the initial diameter of the rivet ( $D$ ), the penetration depth ( $T$ ) and the widening of the rivet tip ( $w$ ) characterising the anchoring zone

## 4.6. Microstructural analysis

### 4.6.1. Light optical microscopy

Light optical microscopy (LOM) was chosen to analyse the microstructure of the base materials and the friction-riveted joints. The LOM samples were cross-sectioned at the mid-point of the rivet, across the whole thickness of the joint. The joints were sectioned using a precision cut-off machine (Struers Secotom 50 [81]) and were subsequently embedded in EpoFix, a cold mounting epoxy resin (Struers) to avoid structural thermal changes of the metallic-insert joint. The samples were prepared by mechanical grinding (TegraPoll-15, Struers) using silicon carbide paper with a particle size 320 mesh, followed by a fine-grinding step with a fine-grinding cloth and 9  $\mu\text{m}$  diamond suspension. Then the specimens were polished with a polishing cloth and a 3  $\mu\text{m}$  diamond solution. To attain the required quality of the pure titanium surface, the samples were further polished with a modified colloidal silica suspension containing 20% hydrogen peroxide and 5% ammonia. Additionally, chemical etching was required to reveal the microstructure of the titanium rivet inside the composite. The overview LOM samples were etched with a color etchant, modified Weck's reagent (100 mL distilled water, 25 mL ethanol and 2 g ammonium bifluoride) to reveal the alpha grains and twins according to their orientation [82]. The microscope used for the LOM images was a Leica DMI5000 M under reflective light.

### 4.6.2. Scanning electron microscopy

A scanning electron microscope (SEM) equipped with an electron backscatter diffraction (EBSD) detector were used to collect detailed microstructure data from different locations on the rivet, to give a better understanding of the microstructural evolution associated with the FricRiveting process. The specimens were prepared by following the same procedure adopted in Section 4.6.1 for LOM specimens up to and including the fine grinding step. In order to achieve the required surface quality for EBSD, the samples were further electropolished with an A3 electrolyte solution using a voltage of 60 V for 20 s at 10 °C [83]. The prepared specimens were subsequently analysed in a field emission gun scanning electron microscope (FEI Quanta FEG) operating at 30 kV. The SEM was equipped with an EDAX Hikari XP EBSD camera and the EBSD analysis software TSL OIM<sup>TM</sup> from EDAX. The generated EBSD maps had a size of 120  $\mu\text{m}$   $\times$  120  $\mu\text{m}$  and 270  $\mu\text{m}$   $\times$  270  $\mu\text{m}$  and a step size of 0.3  $\mu\text{m}$ . The average confidence index varied between 0.22 and 0.68. The quality of the obtained EBSD data was compared with that for face-centred cubic (fcc) metals, for which the fraction of correctly indexed patterns with confidence indices higher than 0.1 have been shown to be 95% (TSL OIM help). In order to eliminate false boundaries as a result of orientation noise, the lower limit for boundary misorientation was set to 2°. Misorientations between 2° and 15° were defined as low-angle boundaries (LABs), and above 15° as high-angle boundaries (HABs). In the EBSD maps, LABs and HABs are depicted as grey and black lines, respectively. The twin



boundaries are indicated by red lines. All grain-size measurements were made on the EBSD maps by the linear-intercept lengths method.

## 4.7. Thermal and physicochemical properties

### 4.7.1. Thermogravimetric analysis

Thermogravimetric analysis (TGA) was performed in order to evaluate the amount of thermomechanical decomposition of the flash material in an optimised friction riveted metallic-insert joint (configuration 0, see Chapter 6) compared to the base material. Figure 4.10 shows where samples of the material were removed for TGA. The flash material consists of the molten material experiencing the harshest thermomechanical processing conditions, thereby allowing an assessment of the maximum possible amount of degradation during processing. The tests and analyses of the results were performed according to ASTM E1131-08 [84]. The equipment used was a TG 209 F3 Tarsus (Netzsch, Germany). A nitrogen atmosphere with a flow rate of 20 mL/min was used to prevent oxidation of the specimen during testing. All samples were extracted using a scalpel; each sample weighed approximately 13 mg. A heating rate of 20 K/min was chosen and the maximum temperature was set to 800 °C. The collected data was then analysed using Proteus Analysis software (Netzsch, Germany) to determine the mass loss and residual mass of each specimen.

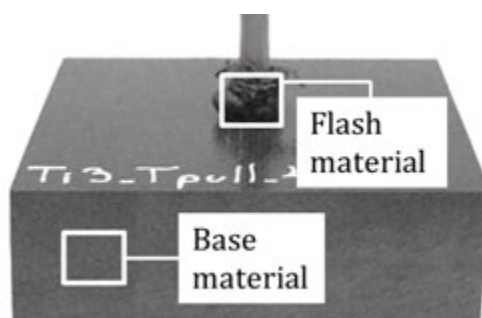


**Figure 4.10.** Metallic-insert joint made of PEEK reinforced with 30% short carbon fibres (PEEK-CA30), indicating where samples of the material were extracted for TGA

## 4.8. Global mechanical performance

### 4.8.1. Pull-out tensile testing

Pull-out tensile testing was selected for assessing the global mechanical strength of the metallic-insert joints (produced for PEEK/grade 3 titanium, PEEK-CA30/grade 3

titanium and TPCL PEEK/grade 3 titanium). Examples of these are shown in Figure 4.11. The dimensions of the pull-out test specimens were 70 mm × 70 mm; the thickness of the specimens depended on the substrate material.

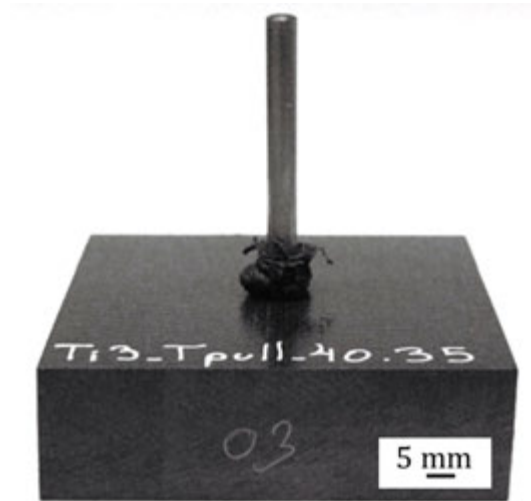


**Figure 4.11.** Pull-out tensile testing specimen for PEEK-CA30/grade 3 titanium joints

Tests were performed in accordance with EN 2591 [85] using a Zwick/Roell 1478 universal testing machine with a load range up to 100 kN. The tensile force and displacement were monitored in displacement control static loading mode, with a traverse speed of 1 mm/min at room temperature. A special clamping device was designed to ensure uniform stress distribution in the composite base plate during testing; see Figure 4.12. Three replicates were tested for each joint configuration and material combination. Load–displacement curves were recorded up to final failure; the specimens were then photographed for failure mode analysis.

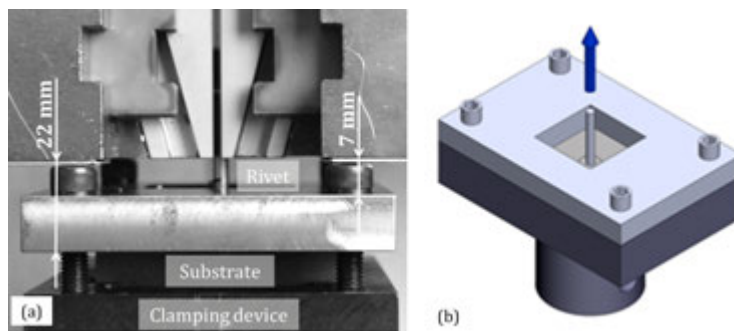


**Figure 4.12.** Clamping device for pull-out testing: (a) overview of the tensile pull-out testing device showing the specimen and clamping distances; (b) schematic 3D view of the clamping device (the window in the cover plate measured 45 mm × 45 mm)

### 4.8.2. Bearing testing

Bearing testing was chosen to determine a suitable edge distance for FricRiveted lap shear specimens. The specimens were manufactured by inserting a grade 3 titanium rivet (diameter 5 mm) through the woven fabric-reinforced PEEK laminate. FricRiveting was then performed on the rivet, with controlled joining parameters leading to reduced heat input (RS: 14000 rpm, FT: 1.5 s, FP: 0.3 MPa, FoP: 0.3 MPa and FoT: 1.5 s) to avoid plastic deformation of the rivet tip. (The reason for deciding to friction-rivet the specimen rather than drill a through-hole and manually insert the rivet was to emulate a rivet-composite interface, similar to that one present in the single lap shear joints. This aspect is enlarged upon in later discussion of friction riveted composite-composite joints.) A schematic overview of a bearing-test specimen, including the position of the hole caused by inserting the rivet, is shown in Figure 4.13. The edge distance and width of the specimens were varied in order to assess the effect of different dimensions on the mechanical performance and the failure mode.

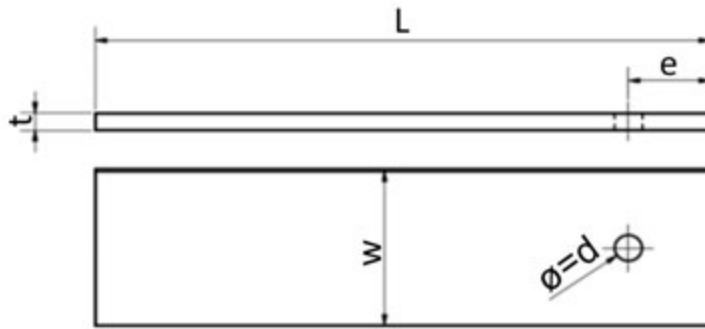


**Figure 4.13.** Schematic of bearing test coupons

The bearing tests were performed at room temperature in an adaptation of ASTM D5961M-08 [32], following procedure A (double shear, tension). Each friction-riveted test specimen was loaded by a bearing force applied at the hole by the rivet inside the specimen. A double shear force was applied through the clamping device shown in Figure 4.14 by a Zwick/Roell 1478 universal testing machine with a load capacity of 100 kN. The tests were performed in displacement control mode at a traverse speed of 2 mm/min. Figure 4.14 shows the bearing test setup, including the positioning of the bearing specimen in the clamping device and the MTS clip gage for precisely monitoring the displacement to allow the strain to be determined.

### 4.8.3. Torsion testing

The torsion tests were performed to identify both the clamping torque suitable for the friction-riveted lap shear specimens and the “break-loose” torque (the torque required to loosen the anchored rivet inside the composite base plate). Torsion test

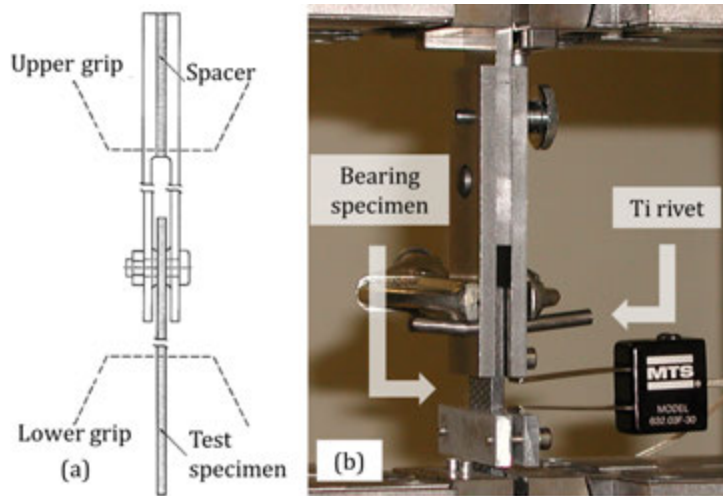


**Figure 4.14.** Bearing test arrangement: (a) schematic showing the test arrangement adapted from [32]; and (b) the actual test setup, showing the test coupon, double-shear clamping device and clip gage

coupons each consisted of a friction-riveted joint of two overlapping TPCL PEEK plates (i.e. lap joint configuration) measuring  $35\text{ mm} \times 35\text{ mm} \times 4.34\text{ mm}$ , resulting in a total thickness of  $8.68\text{ mm}$ . The titanium rivet was threaded for a length of  $16\text{ mm}$  measured from the upper surface of the composite base plate; see Figure 4.15. Two titanium nuts were then tightened against each other on the threaded rivet, with the lower nut being locked with a flat spanner while clamping torque was applied to the upper nut with a torque spanner. In this way the break-loose torque was determined, and a suitable clamping torque for the friction-riveted single-lap shear joints was also identified.

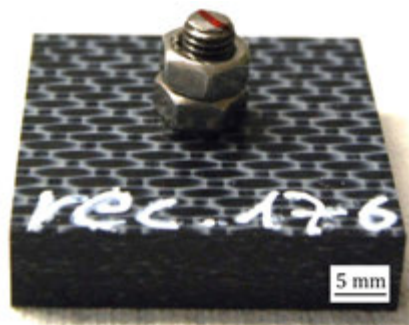


**Figure 4.15.** Specimen used for torsion testing, showing the overlap joint of two composite plates, the threaded rivet and the two nuts used to apply the clamping torque

#### 4.8.4. Lap shear testing

The lap shear tests were carried out using the Zwick/Roell 1478 universal testing machine used for the pull-out tensile and bearing tests. The tests were performed at room temperature with a traverse speed of 2 mm/min. The testing procedure was based on ASTM D5961M-08 [32]. The friction riveted composite-composite joints were manufactured using TPCL PEEK (the dimensions are detailed in the chapter discussing the test results) and a partially threaded grade 3 titanium rivet as described in subsection 4.8.3. The rivet was friction-riveted through the upper composite plate at the overlap area of the joint and into the lower composite part to form the anchoring zone (geometry shown in Figure 4.16 c). In the next step the unthreaded length of the rivet was removed and a titanium M5 nut and washer were screwed onto the remaining threaded part of the rivet, using a defined clamping torque determined from the torsion tests. An example of the single-lap shear specimens is illustrated in Figure 4.16 a, which shows an X-ray scan radiograph of a riveted specimen, and Figure 4.16 b which shows a photograph of the specimen. Figure 4.16 c is a sketch giving the relevant dimensions of the specimen.

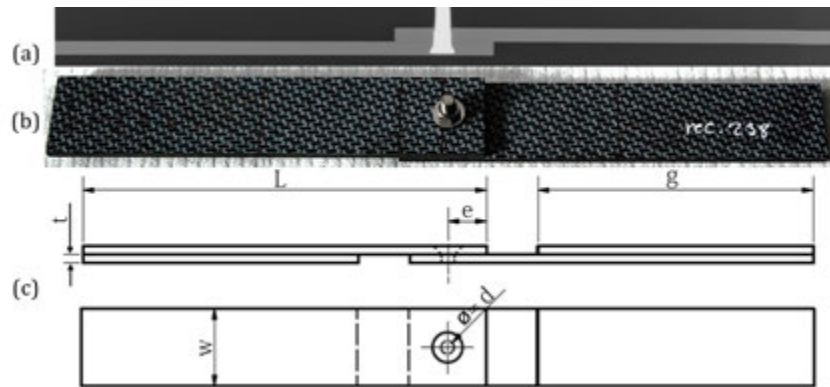


**Figure 4.16.** Single-lap shear specimen before testing, showing (a) an X-ray scan radiograph; (b) a photograph; and (c) a sketch giving the relevant dimensions

The strain distribution of the lap shear specimens was monitored during testing using a digital image correlation system (ARAMIS<sup>®</sup> GOM GmbH, Germany) which uses digital image correlation and tracking technology to calculate the strain on the surface of the tested material. For this purpose, the specimens were coated with a sprayed pattern comprising a uniform layer of white paint overlain by a fine dot pattern in black paint. The system monitors the relative movement of individual dots from which the surface strain distribution is calculated during the test. Figure 4.17 shows the arrangement of a coated specimen inside the clamping device and the ARAMIS<sup>®</sup> system. This method was used to graphically show details of the evolution of the different failure modes.

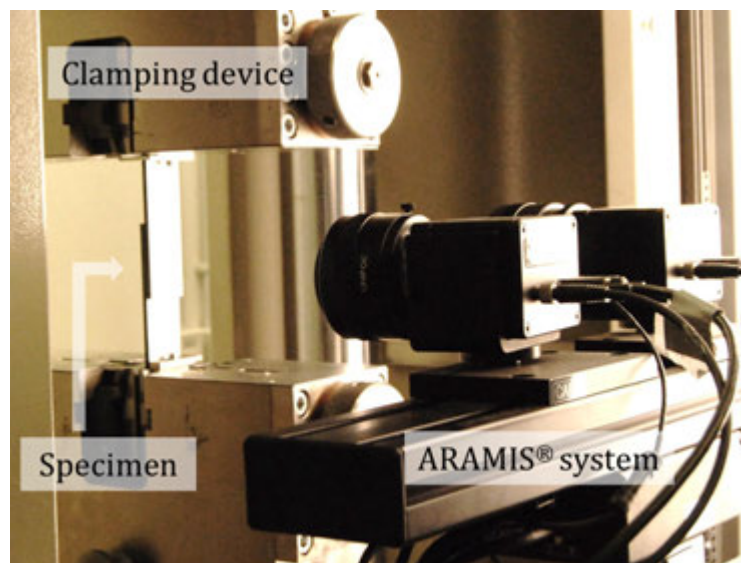


**Figure 4.17.** Test setup for the single-lap shear test, including the ARAMIS® system used to monitor the strain distribution at the joint surface during testing

# 5. Development of FricRiveting for PEEK/titanium joints

## 5.1. Selection of a suitable rivet material

At the beginning of this PhD research program, most of the available knowledge and published results had been focused on aluminum alloy AA2024 as rivet material. Although other studies showing the feasibility of Ti/GF-PEI joints have recently been published [53, 54, 86], no information was available as to the feasibility of using titanium or titanium alloys as the rivet material in the FricRiveting process for joining PEEK and carbon fibre-reinforced plastics. The titanium rivet materials chosen for this study differ from AA2024 regarding mechanical and thermal material properties. These properties are key factors influencing the heat generation and the deformation behaviour of the rivet tip [25] and therefore needed to be taken into account when selecting potential rivet materials for the FricRiveting process. The following challenges were identified for applying the FricRiveting technology in combination with titanium rivets as a substitute for AA2024 rivets.

- Titanium has a higher strength than AA2024, especially grade 5 titanium alloy (Ti6Al4V), as shown in Figure 5.1.
- The thermal conductivity of titanium is much lower than that of AA2024 (thermal conductivity of Ti6Al4V is 6.7 W/mK [55], and of AA2024 it is 151 W/mK [87]) which it was thought might lead to different heat dissipation and deformation behaviour of rivets made from these metals.

In a first step Ti6Al4V, grades 1, 2 and 3 titanium, commonly used in aircraft applications, were selected. Since the titanium materials and AA2024 have different properties, the strength evolution at different temperatures of the selected titanium material [55] and AA2024 [87] were compared: see Figure 5.1. The required information on grade 1 titanium was not found in the literature; however, it was assumed that the trend of grade 1 titanium might be similar to that of grades 2 and 3 titanium, but with an offset on the  $y$ -axis related to its lower strength (Table 4.1). The strength vs. temperature behaviour of Ti6Al4V is significantly different from that of AA2024 and grades 2 and 3 titanium. Additionally, the thermal conductivity of Ti6Al4V (6.7 W/mK) is about 20 times lower than the thermal conductivity of AA2024 (151 W/mK). Therefore, it was believed that it would be highly unlikely that a rivet made of Ti6Al4V would behave during the process similarly to an AA2024 rivet.

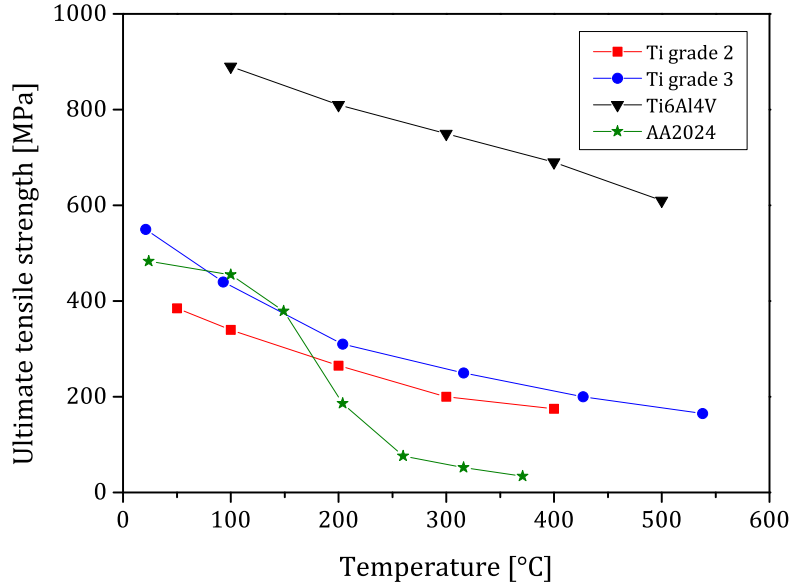


**Figure 5.1.** Evolution of strength at different temperatures of the selected titanium materials [55] compared to AA2024 [87]

In order to be able to confirm these assumptions, experiments were conducted using unreinforced PEEK and Ti6Al4V and titanium grades 1, 2 and 3. As the starting point for the first joining experiments, a parameter set was adopted from a 2007 study of unreinforced PEI and AA2024 [25] (RS: 19000 rpm, FT: 1.5 s, FP: 0.4 MPa, FoP: 0.7 MPa and FoT: 1.5 s). The process parameter combinations tested for each titanium rivet material are shown in Appendix A. The specimens were successfully riveted, in the sense that nothing unusual was observed during the process (such as development of smoke or ash). The anchoring of the rivets was assessed manually by attempting to move each rivet backwards and forwards perpendicular to its longitudinal axis. In this way, a first evaluation of the joint quality was conducted by qualitative inspection [42]. It was found that it was not possible to break the rivet out of the polymer substrate for any of the investigated conditions, which was taken as an indication that the rivets had formed an anchoring feature inside the polymer. The joints were then sectioned at the centre and macrographic photographs were taken of the mid-cross-section; the results were then evaluated by visually inspecting the macrographs. The penetration depth ( $T$ ) and the widening of the rivet tip ( $w$ ) were also measured, followed by calculation of the mushrooming efficiency ( $e_{\text{mush}}$ ) using Equation 4.1. The results of this first feasibility study on PEEK in combination with Ti6Al4V and titanium grades 1, 2 and 3 are given in Appendix A. The results obtained in the course of this preliminary investigation indicated that it would not be possible to deform Ti6Al4V rivets to create anchoring features inside



PEEK substrate material using the FricRiveting equipment that was then available (RSM 400 system, shown in Figure 4.5). In addition to the challenges mentioned above, it was by now clear that the strength of Ti6Al4V at the process temperature was so high that the energy input from the process would be insufficient to deform the rivet tip and create an anchoring feature inside the polymer substrate.

However, the feasibility of FricRiveting process on PEEK and grades 1, 2 and 3 titanium had been demonstrated. Considering the findings of the three feasibility studies with commercially pure titanium, and since grade 3 titanium possessed the highest tensile strength of the three materials (Table 4.1), grade 3 titanium was chosen to be the rivet material for all further investigations within the framework of this thesis. Grade 3 titanium displays good mechanical performance, including high strength, which is very important for structural applications. Additionally, promising first results had been obtained in terms of forming an anchoring feature in the polymer substrate, essential for the successful application of the FricRiveting technology.

## 5.2. Feasibility study on PEEK/grade 3 titanium joints

The reproducibility and robustness of the process was essential when assessing the effect of the process parameters on the joint formation or its performance. Therefore, an assessment was carried out of the reproducibility of the FricRiveting process using the RSM 400 equipment in its original configuration when operating with an FP up to 0.7 MPa for metallic-insert joints made of PEEK and grade 3 titanium, based on the process parameter ranges established in the previous section.

The standard deviation of the results might be reduced by selecting an appropriate measurement and examination method. Therefore, scans obtained by X-ray radiography – a non-destructive testing (NDT) technology with higher precision and lower standard deviation than LOM measurements – were taken of all specimens analysed in the investigation. The use of X-ray radiography allowed the measurement of  $T$  and  $w$ , and thereby the calculation of  $e_{\text{mush}}$ , prior to mechanical testing. This feature was a major advantage of X-ray radiography over the previously used LOM method, which entailed physically sectioning the riveted joints and measuring  $T$  and  $w$  from the mid-cross-sections. X-ray scans gave a more precise measurement of the anchoring zone, since the exact centre of the rivet could be determined and measured graphically.

The metallic-insert joints were produced according to the configurations shown in Table 5.1. In this initial phase of the work, joints were produced without the implementation of the differential pressure switch (see description in Section 4.2.1). Therefore joints produced at values above 0.6 MPa were prone to process abnormalities, which may explain the large standard deviation of some joining conditions. The levels of the different process parameters were chosen by taking into account the above feasibility study carried out with this material combination. For each

process parameter, minimum and maximum values were selected, except for FoT, which was kept constant at 10s to ensure a sufficient and uniform joint consolidation. Due to the low thermal conductivity of the thermoplastic material and the titanium rivet, cooling and joint consolidation takes several seconds. Therefore the longer FoT of 10s was adopted to ensure that the joint was fully consolidated under pressure, and to prevent shrinkage of the polymer which could rupture the bond line between the consolidating polymer layer at the interface of the metallic rivet and the thermoplastic substrate. These 16 configurations were chosen to assess the replicability of the joints and the robustness of the process by assessing the following output parameters describing the joint characteristics: the penetration depth  $T$ , the deformed width of the rivet tip  $w$ , the mushrooming efficiency  $e_{\text{mush}}$  and the pull-out force  $F_{\text{pull-out}}$ . Three replicates were produced for each configuration.

**Table 5.1.** Parameter configurations selected for the FricRiveting of grade3 titanium and PEEK (three replications for each configuration)

Configuration	Process setting parameters			
	RS [rpm]	FT [s]	FP [MPa]	FoP [MPa]
1	18000	1	0.5	0.7
2	18000	1.5	0.5	0.7
3	18000	1	0.5	0.9
4	18000	1.5	0.5	0.9
5	18000	1	0.7	0.7
6	18000	1.5	0.7	0.7
7	18000	1	0.7	0.9
8	18000	1.5	0.7	0.9
9	20000	1	0.5	0.7
10	20000	1.5	0.5	0.7
11	20000	1	0.5	0.9
12	20000	1.5	0.5	0.9
13	20000	1	0.7	0.7
14	20000	1.5	0.7	0.7
15	20000	1	0.7	0.9
16	20000	1.5	0.7	0.9

All of the configurations in Table 5.1 were successfully riveted, which is to say that no unusual effects, such as the development of smoke or ashes, were observed during the process. Visual inspection of the joints showed that the rivet did not penetrate the whole substrate for any of the riveted joints. An example of the metallic-insert joints is shown in Figure 5.2 a.

Figure 5.2 b is a sample X-ray scan (scans of all specimens in this study are shown in Appendix B). The results from measuring the penetration depth of the rivet and the widening of the rivet tip are listed in Table 5.2. The penetration-depth range, depending on the process parameter configuration, was from 6.4 mm to 12.1 mm and

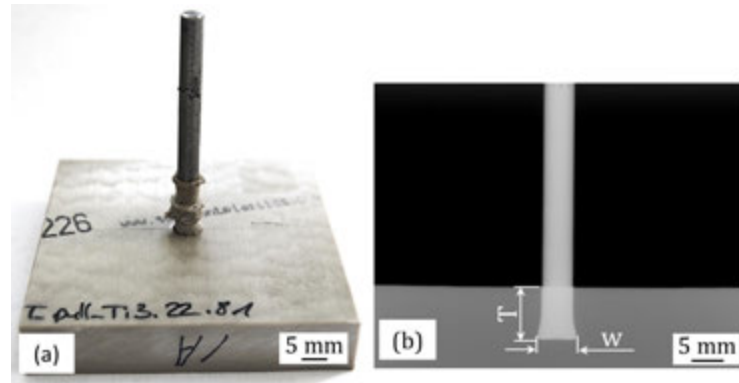


**Figure 5.2.** Friction Riveted metallic-insert joint of PEEK/grade 3 Ti: (a) photograph of the joint; (b) X-ray scan radiograph of the joint, indicating penetration depth ( $T$ ) and deformed width ( $w$ )

shows a maximum standard deviation of 13%. The widening of the rivet tip ranged between 5.3 mm and 7.9 mm, with a maximum standard deviation of 12%.

**Table 5.2.** Summary of test results for all 16 configurations (including three replicates in each configuration)

Configuration	$T$ [mm]	$w$ [mm]	$\epsilon_{\text{mush}}$ [%]	$F_{\text{pull-out}}$ [kN]	Failure mode
1	$7.1 \pm 0.5$	$5.3 \pm 0.2$	$5.7 \pm 3.9$	$0.7 \pm 0.3$	III
2	$9.1 \pm 0.6$	$5.4 \pm 0.04$	$7.2 \pm 1.0$	$1.1 \pm 0.04$	III
3	$7.2 \pm 0.3$	$5.7 \pm 0.2$	$14.5 \pm 5.0$	$2.2 \pm 0.3$	III
4	$9.5 \pm 0.2$	$7.2 \pm 0.8$	$44.1 \pm 19.9$	$6.7 \pm 2.8$	III
5	$6.1 \pm 0.4$	$6.0 \pm 0.6$	$20.2 \pm 14$	$2.6 \pm 1.9$	III
6	$8.9 \pm 0.3$	$5.3 \pm 0.1$	$6 \pm 1.8$	$1.3 \pm 0.6$	III
7	$6.4 \pm 0.3$	$6.6 \pm 0.8$	$31.5 \pm 18.9$	$4.3 \pm 2.5$	III
8	$9.1 \pm 0.2$	$7.3 \pm 0.9$	$46.9 \pm 21$	$6.5 \pm 2.4$	III, III, I
9	$9.4 \pm 1.0$	$5.4 \pm 0.1$	$7.1 \pm 1.4$	$0.9 \pm 0.1$	III
10	$12.1 \pm 0.4$	$5.6 \pm 0.1$	$11.3 \pm 3.4$	$2 \pm 0.8$	III
11	$9.8 \pm 0.2$	$6.0 \pm 0.1$	$19 \pm 1.9$	$3.7 \pm 0.6$	III
12	$10.5 \pm 0.2$	$7.9 \pm 0.3$	$57.2 \pm 6.4$	$9.2 \pm 1.1$	I, I, IV
13	$8.5 \pm 0.8$	$5.3 \pm 0.1$	$6.1 \pm 1.3$	$0.9 \pm 0.1$	III
14	$10.2 \pm 0.6$	$5.4 \pm 0.1$	$8.5 \pm 2.8$	$1.4 \pm 0.2$	III
15	$8.7 \pm 0.4$	$6.0 \pm 0.1$	$19.3 \pm 2$	$3.4 \pm 0.1$	III
16	$11.1 \pm 0.3$	$7.8 \pm 0.8$	$55.7 \pm 20.6$	$8 \pm 1.8$	III, III, I

### 5.2.1. Assessment of the joint formation

In the following, the collected data has been reordered to show how the process parameters tended to affect the joint formation, represented by the penetration depth

and the widening of the rivet. Due to the large standard deviation, the following analysis was only used to indicate the tendency of the process parameters to affect the joint formation. The data set was divided into 8 configuration pairs; each pair represented two process parameter configurations, in which only one parameter was changed (i.e., the investigated process parameter) while the remaining process parameters were held constant for that pair.

The graph in Figure 5.3 a displays the changes in penetration depth for eight process parameter-set pairs when RS was increased from 18000 rpm (blue bar) to 20000 rpm (red bar). It is seen that this increase in RS led to an increased penetration depth for all eight configuration pairs.

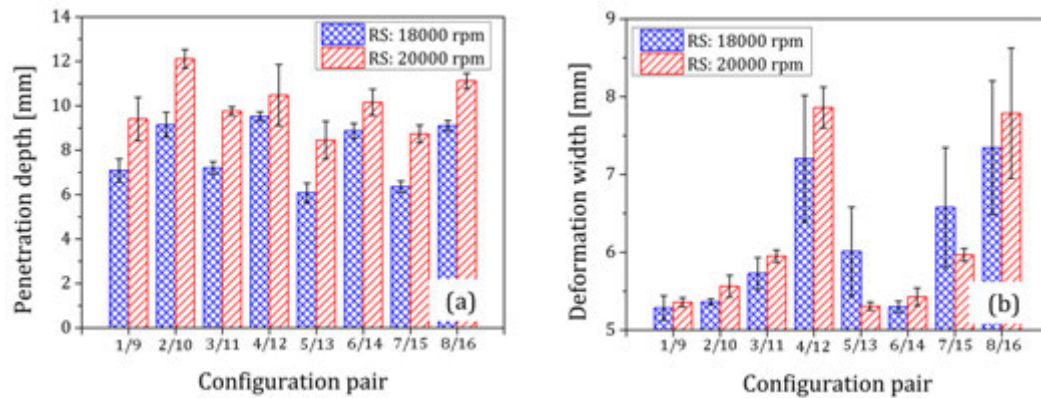


**Figure 5.3.** Influence of the rotational speed (RS) on (a) penetration depth of the rivet, and (b) widening of the rivet tip

Figure 5.3 b shows the changes of the widening of the rivet tip associated with the same increase in RS. The widening of the rivet tip increased in most of the configuration pairs, with the exception of pairs 5/13 and 7/15, considering that these were produced with FP values higher than the calibration range of 0.6 MPa. In these pairs the widening tended to decrease with increasing the RS. Such inconsistencies might be explained by the high standard deviation in these configuration pairs. At higher rotational speeds, the internal shearing was also greater (perhaps by viscous dissipation), leading to a higher energy input. Thus, increasing the RS increased the thermal energy, leading to more softening of the polymer as well as plasticising the rivet tip, allowing both increased penetration depth and widening of the rivet tip [50]. This behaviour explains the tendency of increased penetration depth and widening of the rivet tip when the RS was increased.

Amancio-Filho and dos Santos [50] investigated the influence of the RS on the microstructure of PEI/AA2024 friction-riveted metallic-insert joints. They discovered that increasing the RS increased the widening of the rivet tip and increased the penetration depth of the rivet inside the polymer substrate, which is consistent with the findings of the present study. A different explanation of the tendency to increase deformation width with increased RS is to consider the influence of the RS

on the theoretical heat input. Amancio-Filho [25] proposed a method of estimating the heat evolution due to the FricRiveting process; see Equation 5.1, where  $\mu$  is the kinematic friction coefficient,  $P(r)$  the normal friction pressure,  $\eta$  the polymer viscosity in the molten state,  $V_{\max}$  the maximum tangential speed of the rivet and  $H$  the average width of the consolidated polymer layer. Equation 5.1 shows that increasing the RS (i.e.,  $V_{\max}$ ) increases the total heat input. It also shows that the total energy input increases geometrically as  $V_{\max}$  increases – that is, doubling the tangential speed of the rivet increases the total heat input by a factor of four. Thus the relationship demonstrated by this equation links the increased deformation width to increased RS.

$$Q_{\text{total}} = \left[ \left( \frac{2}{3} \mu P(r) \right) + \frac{\eta V_{\max}}{H} \right] V_{\max} \quad (5.1)$$

The variation in penetration depth and widening of the rivet tip by changing FT is displayed in Figure 5.4. These graphs also show the eight configuration pairs, where each pair stands for two process parameter configurations differing only in one parameter (the investigated process parameter; here, FT) while the remaining process parameters were kept constant, as discussed above. Increasing FT from 1 s (blue bar) to 1.5 s (red bar) resulted in an increased penetration depth for all eight configuration pairs; see Figure 5.4 a. The increased FT was related to increased mechanical energy input, because the longer the FricRiveting process took to complete, the longer the mechanical energy was generated and thus the greater the accumulated energy; more thermal energy led to more softening of the polymer, and the penetration depth therefore increased [50]. Figure 5.4 b reveals that increasing the FT from 1 s (blue bar) to 1.5 s (red bar) increased the deformation width of the rivet in all configuration pairs except 5/6; this inconsistency might be the result of the relatively high standard deviation of the analysed data set. Therefore, the tendency for the rivet widening to increase is also explained by the increase in thermal energy related to the longer duration of the FricRiveting process associated with higher FT.

The trend of the effect of FP on joint formation is shown in Figure 5.5. In Figure 5.5 a it is seen that increasing the FP from 0.5 MPa (blue bar) to 0.7 MPa (red bar) decreased the penetration depth, except in the configuration pair 12/16. Amancio-Filho [25] demonstrated in a case study on PEI/AA2024 metallic-insert joints that increasing the joining pressure tended to raise the local temperature during the FricRiveting process. Higher temperatures are an indicator of increased thermal energy, which might lead to more plasticisation of the rivet tip. The current understanding of heat input theory is that the rate of shear deformation is much greater than the deformation rate due to the penetration of the rivet. Therefore the FP contributes far less heat (by viscous dissipation) than does the RS [25]. For specimens joined with the same heat input, an increase in FP usually creates smaller volumes of molten polymer than an increased RS does. Although the peak temperature in the molten polymer volumes for two specimens with equal heat input should, in theory, be the same, the transfer of heat from the molten polymeric pool

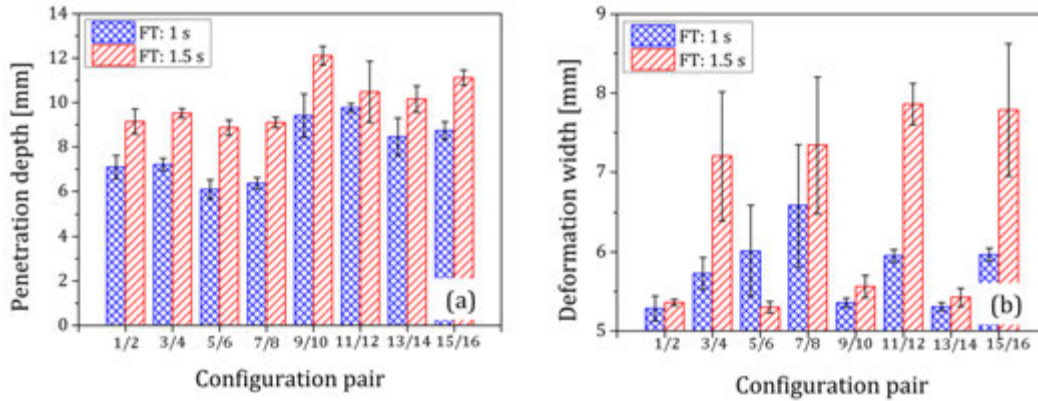


**Figure 5.4.** Influence of friction time (FT) on (a) penetration depth of the rivet, and (b) widening of the rivet tip

to the rivet may be more efficient in the case of the FP increments owing to the smaller volume involved. This theory may explain the current results since, an increased FP from 0.5 MPa to 0.7 MPa would increase the temperature of the molten layer; however, due to the small volume in the proximity of the rivet tip, the rivet would plasticise more rapidly. The more highly plasticised – that is, softer – rivet tip would exert less mechanical resistance to the reaction force exerted by the solid substrate, hindering the rivet from penetrating any further. This may also explain the behaviour observed in some of the configuration pairs shown in Figure 5.5 b, where increasing the FP from 0.5 MPa (blue bar) to 0.7 MPa (red bar) led to an increase in the deformation width in four of the configuration pairs (1/5, 3/7, 4/8 and 11/15) but a decrease in the other four pairs. Thus no clear pattern emerged as to the effect of the FP on the deformation width of the rivet tip. However this might be also explained by a lack in replicability and robustness in the process due to the initial lack calibration of the RSM 400 equipment leading to inconsistencies related to the large standard deviation of the analyzed data set. This preliminary analysis showed the importance of the use of a differential pressure switch for the next phase of the work.

The graphs in Figure 5.6 show variations in penetration depth and widening of the rivet tip depending on different levels of FoP. Increasing the FoP from 0.7 MPa (blue bar) to 0.9 MPa (red bar) tended to increase penetration depth in all configuration pairs except 10/12: see Figure 5.6 a. The FricRiveting process generates heat, resulting in a softened polymer region in the vicinity of the metallic rivet [50]. Higher FoP allows deeper rivet penetration in the softened polymer. Figure 5.6 b shows that increasing the FoP from 0.7 MPa (blue bar) to 0.9 MPa (red bar) tended to increase the deformation width significantly in all configuration pairs. Since FricRiveting process generates heat, it also results in plasticising the rivet tip [50]. It was assumed that higher FoP would cause the plasticised rivet tip to be further widened. This assumption may explain the behaviour shown in Figure 5.6 b.

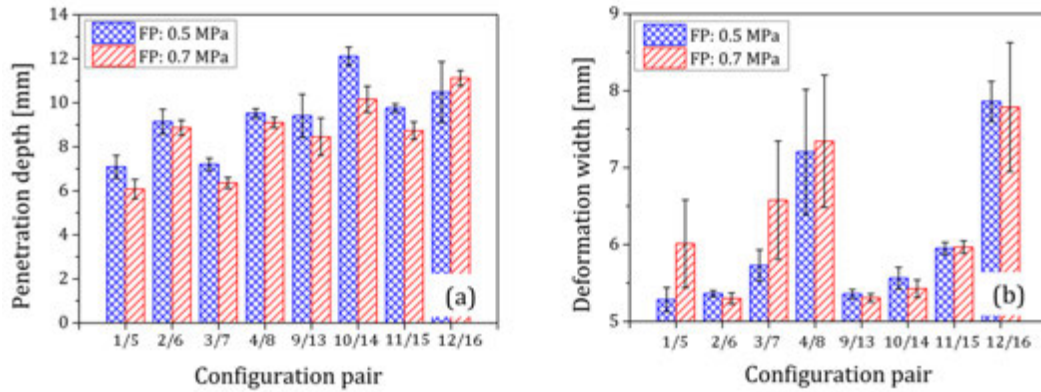


**Figure 5.5.** Influence of friction pressure (FP) on (a) rivet penetration depth, and (b) widening of the rivet tip

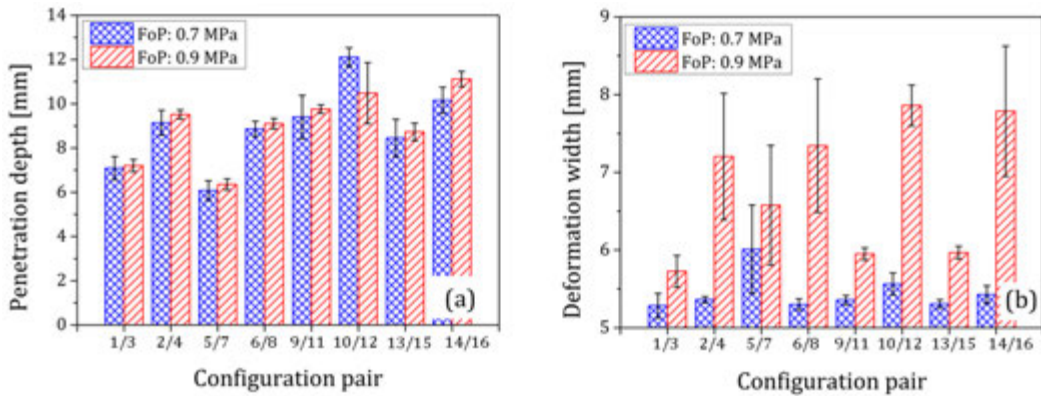


**Figure 5.6.** Influence of forging pressure (FoP) on (a) rivet penetration depth, and (b) widening of the rivet tip

### 5.2.2. Assessment of the joint mechanical performance

All the specimens were subjected to pull-out tensile tests to assess the mechanical strength of the metallic-insert joints. The tests were performed using the equipment arrangement and procedure described in Section 4.8.1. The force–displacement curves for all tested specimens are given in Appendix C. The measurements obtained from the X-ray scans were used to calculate the mushrooming efficiency using Equation 4.1. The results of the pull-out tensile tests and the values of the mushrooming efficiency are listed in Table 5.2 and shown in Figure 5.7, which also indicate the standard deviation. The mushrooming efficiency ranged from 5.7% to 57.2%, with a maximum standard deviation of 69%. The pull-out force ranged between 0.7 kN and 9.2 kN with a maximum standard deviation of 73%.

Figure 5.7 shows that the standard deviation was relatively high for both mushrooming efficiency and pull-out force. In general, the standard deviation of the

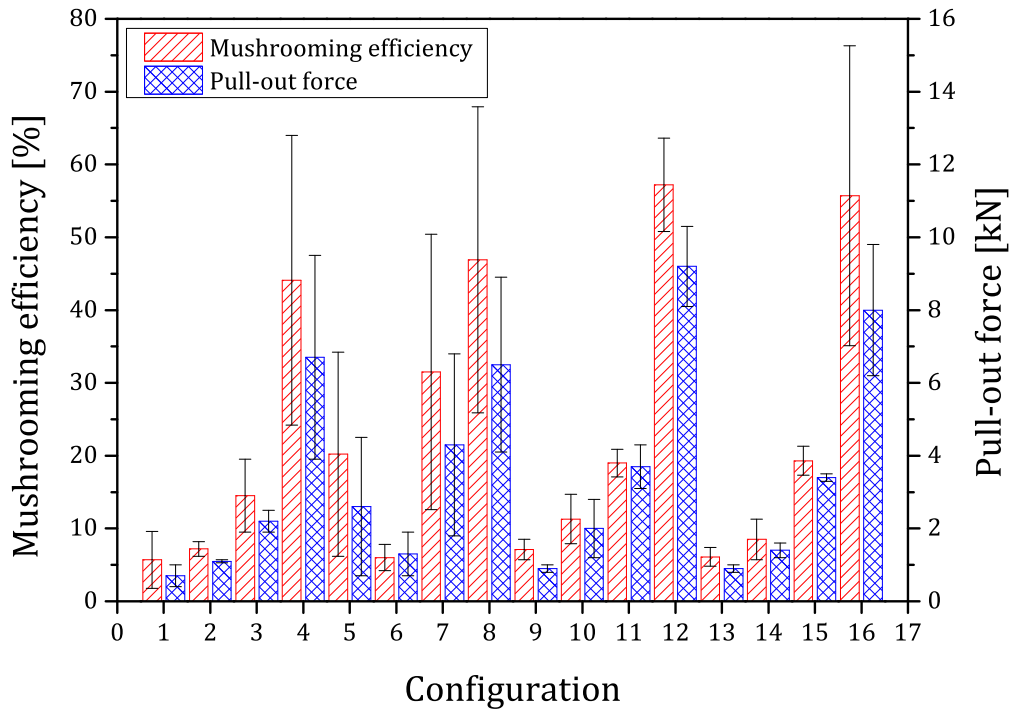


**Figure 5.7.** Overview of the results of mushrooming efficiency and pull-out force for all test configurations (Table 5.1) for PEEK/grade 3 Ti joints

tensile strength in polymer welding lies within  $\pm 10\%$  [54]. The high standard deviation observed for mushrooming efficiency and pull-out force was associated with the standard deviation in the penetration depth and the widening of the rivet tip. It is assumed that if the joint formation showed variations within one parameter set, the performance also varied. However, it was found difficult to analyse the data set with regard to the impact of the process parameters on the joint because the standard deviations of the observations were too pronounced.

In the present study, no further investigation was carried out on this relationship because, as seen in Table 5.2 and Figure 5.7, the standard deviation in this data set was too large. Therefore, the reproducibility of the process first needed to be improved to allow further investigations.

As a result of the pull-out tests, three failure modes were observed (see Table 5.2), defined as type I, or “through the rivet” failure; type III, or “full rivet pull-out” failure; and type IV, or “rivet pull-out” failure, introduced earlier in Section 2.2.8. Examples of these failure modes are shown in Figure 5.8.

At the beginning of this chapter it was proposed that improved measurement and examination methods using X-ray radiography might reduce the standard devi-



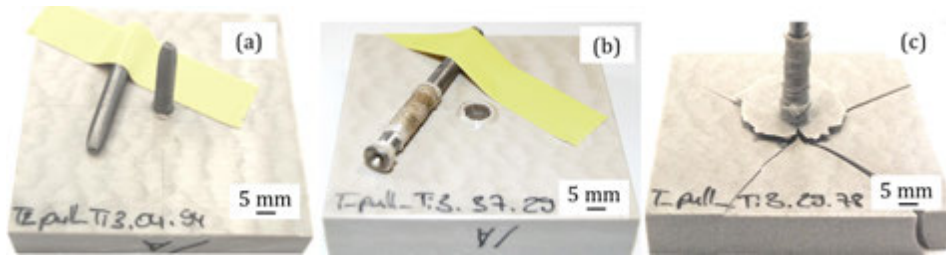


**Figure 5.8.** Example of the failure modes observed after the tensile pull-out tests: (a) type I, “through the rivet” failure; (b) III, “full rivet pull-out” failure; and (c) type IV, “rivet pull-out” failure

ation. The results of this investigation did not support this proposition. The main reason for the low level of reproducibility was related to the limitations of the RSM 400 FricRiveting equipment (Section 4.2) without the differential pressure switch required for the calibration of pressures above 0.6 MPa. The joining parameters adopted in the study demanded that the joining equipment operates at the upper limit of its capability, as explained in detail in Section 4.2. The results of implementing the differential pressure sensor and the calibration of higher friction pressure levels, as well as the selection of a design-of-experiment methodology to evaluate the joint formation and performance, are shown in Chapter 6.

### 5.3. Summary and conclusion

In this chapter the feasibility of the application of the FricRiveting process to PEEK and titanium has been demonstrated. Furthermore, a titanium rivet material suitable for the FricRiveting process has been identified and an assessment of the joint formation and the joint mechanical performance has been also carried out. The results obtained by these investigations are summarised in the following:

- The Ti6Al4V rivet could not be deformed to produce an anchoring feature inside a PEEK substrate, using the RSM 400 FricRiveting equipment (Figure 4.5) that was available at that time. It was assumed that the high strength of the Ti6Al4V rivet was such that the energy input generated by the RSM 400 equipment was insufficient to produce widening of the rivet tip.
- The feasibility of applying the FricRiveting process on PEEK and grades 1, 2 and 3 titanium rivets was successfully demonstrated.
- Grade 3 titanium was chosen as a suitable rivet material for all further investigations in the framework of this thesis. The material was known to possess relatively high strength, and it was also possible to form a pronounced anchoring feature inside the PEEK substrate.
- The most promising results regarding widening of the rivet tip and mechanical performance were shown in configuration 12 (RS: 20000 rpm, FT: 1.5 s,

FP: 0.5 MPa, FoP: 0.9 MPa and FoT: 10 s) leading to a mean mushrooming efficiency of 57.2% and reaching an average pull-out force of 9.2 kN.

- The standard deviations for the obtained results were appreciably large: the maximum standard deviation for the penetration depth was 13%, and for the widening of the rivet tip the maximum was 13%. The maximum standard deviation for the mushrooming efficiency was 69%, and for the pull-out force it was as high as 73%. Due to these high standard deviations, the assessment of the joint formation and mechanical performance so far revealed only the tendencies of the process parameters to affect rivet penetration depth, widening of the rivet tip, mushrooming efficiency and pull-out force.
- As a result of the pull-out tests, three different failure modes were observed. The failure modes were identified as type I, “through the rivet” failure; type III, “full rivet pull-out” failure; and type IV, “rivet pull-out” failure. Most of the specimens failed in type III, where the crack started to form around the anchoring zone of the polymer and the rivet was completely removed, leaving a hole with the same diameter as the deformed rivet tip.

## 6. Relationship between process, microstructure and mechanical performance

It is known that the thermomechanical phenomena during FricRiveting affect the properties of the joining partners. In this chapter the feasibility of the application of the FricRiveting process to PEEK reinforced with 30% short carbon fibres and grade 3 titanium will be demonstrated. DoE was used to assess the effect of the FricRiveting process parameters on joint formation and the quasi-static mechanical performance of metallic-insert joints. In the following, an investigation of the thermomechanical impact of the process is described. The temperature evolution and the effect during joining of the mechanical energy input on the resulting microstructural changes and material flow were assessed. Finally, the degree of process-related thermal degradation in the PEEK-CA30 composite matrix was evaluated by thermal analysis.

### 6.1. FricRiveting of short carbon fibre-reinforced PEEK and grade 3 titanium

A full-factorial design of experiments (DoE), including an additional centre point, was chosen to evaluate the feasibility of the process on the material combination PEEK reinforced with 30% short carbon fibres and grade 3 titanium. The DoE analysis was performed to determine correlation between the process parameters and the joint formation associated with the mushrooming efficiency, rivet penetration depth and mechanical energy input, as well as the joint performance as represented by the pull-out force. The input parameters (factors) were the process parameters RS, FT, FP and FoP. The output parameters (responses) were the mushrooming efficiency – representing the anchoring efficiency of the rivet in the polymeric base plate – the rivet penetration depth  $T$ , the mechanical energy input and the pull-out force  $F_{pull-out}$ . The DoE test matrix is shown in Table 6.1 with low and high levels as well as the centre point configuration of the process parameters. Full-factorial design contains four factors on two levels, so the number of configurations is  $N = 2^4 = 16$  together with a centre point on the intermediate position of all factors, making a total of 17 different joining conditions: see Table 6.2. The metallic-insert joints were FricRiveted according to the parameter configurations resulting from the  $2^4$  full factorial design, including the additional centre point (configuration 9), also

shown in Table 6.2. In this designed experiment the RS varied between 18000 rpm and 20000 rpm, the FT between 1 s and 1.5 s, the FP between 0.7 MPa and 0.9 MPa, the FoP between 0.9 MPa and 1 MPa and the FoT was kept constant at 10 s to ensure a sufficient and uniform joint consolidation, as done in the previous study (Section 5.2). The parameter levels were chosen from consideration of the results obtained from the previous investigations. Three replicates were produced for the corner points and six replicates for the centre point for statistical analysis of variance (ANOVA).

**Table 6.1.** Full factorial design matrix, showing the two levels  $(-1, 1)$  of the investigated factors and the centre point configuration (0) corresponding to the intermediate position of all factors

Factors	Level		
	-1	0	1
RS [rpm]	18000	19000	20000
FT [s]	1	1.25	1.5
FP [MPa]	0.7	0.8	0.9
FoP [MPa]	0.9	0.95	1
<i>FoT</i> [s]	10		

In order to calculate the mechanical energy input during the FricRiveting process, Equations 2.2 and 2.3 introduced in Section 2.2) were used. After applying the values given in Tables 6.2 and 6.3 in Equation 2.2, the second term (translational energy component) was neglected, because its contribution to the total mechanical energy input was about 20 times lower than the contribution from the first term (rotational energy component), as shown in Figure 6.1. Therefore, the mechanical energy input was calculated from Equation 2.3.

In order to allow the calibration of higher FP levels for the working ranges needed for titanium rivets, the FricRiveting system (RSM 400; see Figure 4.5) was augmented by incorporating a differential pressure sensor as discussed in Section 4.2. It was observed in Section 5.2 that high FP and FoP levels offered the most promising results regarding the mushrooming efficiency and the pull-out force. Therefore high FP and FoP levels were chosen for the current investigation. To obtain additional information about the joint formation, during the joining action the torque was measured with the torque measurement platform described in Section 4.2. The acquired torque data is to be utilised to calculate the mechanical energy input associated with rivet rotation.

All of the configurations were successfully riveted – that is to say, no unusual events such as the development of smoke or ashes were observed during the process. Visual inspection of the metallic-insert joints showed that the rivet did not penetrate the whole substrate in any of the specimens. An example of a metallic-insert joint is shown in Figure 4.11 b.

**Table 6.2.** Parameter configurations as a result of the  $2^4$  full factorial design, including the additional centre point (configuration 9)

Configuration	Process setting parameters			
	RS [rpm]	FT [s]	FP [MPa]	FoP [MPa]
1	18000	1.5	0.7	0.9
2	20000	1.5	0.7	0.9
3	18000	1.5	0.9	1
4	20000	1.5	0.9	1
5	18000	1	0.7	1
6	18000	1.5	0.9	0.9
7	18000	1	0.9	1
8	18000	1.5	0.7	1
9 (centre point)	19000	1.25	0.8	0.95
10	20000	1	0.9	1
11	20000	1.5	0.7	1
12	20000	1	0.7	0.9
13	20000	1	0.7	1
14	18000	1	0.7	0.9
15	20000	1	0.9	0.9
16	18000	1	0.9	0.9
17	20000	1.5	0.9	0.9

The friction-riveted PEEK-CA30/grade3 titanium specimens were X-rayed using the procedure described in Section 4.5. An example of an X-ray scan is shown in Figure 4.9. The penetration depth and the widening of the rivet tip at the centre of the joint were precisely measured in this way. (The X-ray scans of all specimens are included as Appendix D.) The results of these measurements are listed in Table 6.3. Depending on the process parameter configuration, the penetration depth varied between 7.4 mm and 12.6 mm, with a maximum standard deviation of 6%. Comparing these results with those discussed in Section 5.2, the maximum standard deviation of the penetration depth was more than halved. The widening of the rivet tip varied between 6.7 mm and 9.7 mm, with a maximum standard deviation of 3%, four times lower than in the previous study. These findings demonstrate that the improvement of the RSM 400 FricRiveting system by incorporating the differential pressure sensor reduced the maximum standard deviation considerably.

The acquired torque data was used to calculate the mechanical energy input from Equation 2.3. The results are given in Table 6.3. The mechanical energy input varied between 685 J and 1525 J, depending on the combination of process parameters. The measurements of the deformation width of the rivet tip obtained from the X-ray scans were used to calculate the mushrooming efficiency using Equation 4.1. In order to assess the mechanical strength of the metallic-insert joints, the specimens were

**Table 6.3.** Summary of the test results of all 17 configurations (with 6 replicates for the centre point in configuration 9 and 3 replicates for all other configurations), differentiating between responses for joint formation and joint performance

Configuration	Joint formation				Joint performance
	$E_{\text{mech}}$ [J]	$T$ [mm]	$w$ [mm]	$e_{\text{much}}$ [%]	$F_{\text{pull-out}}$ [kN]
1	777 ± 48	9.7 ± 0.0	7.1 ± 0.1	41.5 ± 0.9	7.8 ± 0.9
2	1201 ± 64	12.0 ± 0.1	8.2 ± 0.2	63.7 ± 4.6	10.0 ± 0.6
3	825 ± 16	11.8 ± 0.3	9.0 ± 0.1	80.2 ± 1.5	10.7 ± 0.0
4	1525 ± 44	12.0 ± 0.3	9.7 ± 0.1	93.6 ± 1.0	10.4 ± 0.1
5	708 ± 16	8.1 ± 0.2	7.2 ± 0.0	43.6 ± 0.4	7.9 ± 0.2
6	960 ± 92	11.4 ± 0.3	8.1 ± 0.0	61.8 ± 1.0	9.6 ± 0.2
7	795 ± 52	7.9 ± 0.2	7.5 ± 0.0	50.0 ± 0.5	8.5 ± 0.4
8	973 ± 63	9.4 ± 0.3	7.5 ± 0.0	50.2 ± 1.1	9.8 ± 0.4
9	1042 ± 53	10.2 ± 0.3	8.0 ± 0.1	61.0 ± 2.5	9.6 ± 0.5
10	1131 ± 51	10.5 ± 0.0	8.6 ± 0.0	71.1 ± 0.4	10.7 ± 0.0
11	1220 ± 38	12.1 ± 0.3	8.6 ± 0.1	73.1 ± 2.3	10.7 ± 0.1
12	918 ± 31	9.1 ± 0.1	7.2 ± 0.0	44.7 ± 0.4	7.7 ± 0.3
13	923 ± 54	9.1 ± 0.5	7.7 ± 0.2	55.3 ± 3.5	9.7 ± 0.6
14	685 ± 14	7.4 ± 0.1	6.7 ± 0.0	34.4 ± 0.2	6.3 ± 0.1
15	1117 ± 20	10.5 ± 0.2	7.6 ± 0.0	52.1 ± 0.1	8.3 ± 0.2
16	737 ± 10	8.7 ± 0.2	7.1 ± 0.0	41.7 ± 0.8	6.5 ± 0.3
17	1474 ± 55	12.6 ± 0.1	9.1 ± 0.0	81.7 ± 0.7	10.7 ± 0.1

mechanically tested using pull-out tests. The testing arrangement and procedure used were as described in Subsection 4.8.1. The values of mushrooming efficiency and the results of the pull-out tests are given in Table 6.3, also indicating the standard deviation. The mushrooming efficiency varied between 34.4% and 93.6%, with a maximum standard deviation of 7%. The pull-out force varied between 6.3 kN and 10.7 kN, with a maximum standard deviation of 11%. These results show that the maximum standard deviation was significantly reduced from those obtained in the previous study discussed in Section 5.2. The improvements to the RSM 400 FricRiveting system decreased the maximum standard deviation for mushrooming efficiency from 69% (Section 5.2) to 7%. The maximum standard deviation for the pull-out force was reduced from 73% to 11%. The significant reduction of the standard deviation in all of the investigated responses indicates that the improvement to the equipment led to a robust FricRiveting process, including high FP levels. This allowed the use of the acquired data set for assessing the effect of the process parameters on the joint formation and the joint mechanical performance.

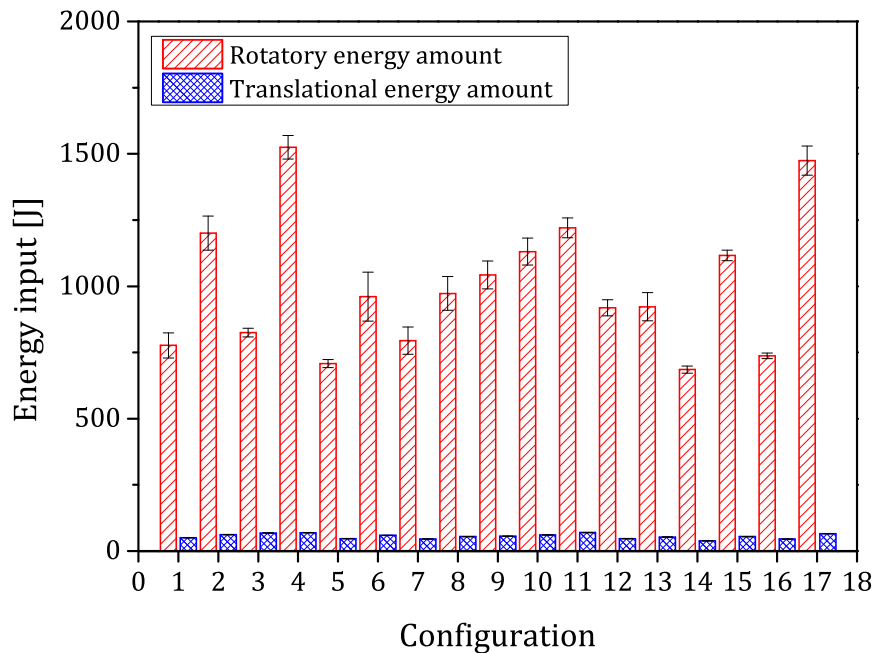


**Figure 6.1.** Comparison of the contribution of the rotational and translational energies to the total mechanical energy input

## 6.2. Influence of the process parameters on joint formation

The influence of the process parameters on joint formation was investigated by analysing the effect of the process parameters on the mushrooming efficiency, the rivet penetration depth and the mechanical energy input. The results are discussed in the following sections.

### 6.2.1. Mushrooming efficiency of the deformed rivet

The main effects for mushrooming efficiency given in Table 6.3 are plotted in Figure 6.2. These summarise the effect of the process parameters on the mushrooming efficiency response. The plots show that each factor strongly affected the mushrooming efficiency. Steeper slopes in the diagrams indicate a greater impact of the process parameter on the effect being investigated. The increases in RS, FT and FoP also increased the mushrooming efficiency (Figure 6.2 a, b, d) and the deformation width at the rivet tip. This behaviour is explained by the mechanical energy input (Equation 2.2). It is seen that an increase in RS, FT or FoP increases the total mechanical energy input, providing additional energy for the plastic deformation of

## 6. Relationship between process, microstructure and mechanical performance

the titanium rivet and widening the rivet tip. The results parallel the findings of [50] in their investigation of the influence of the rotational speed on the microstructure and the properties of friction riveted metallic-insert joints made of PEI and AA2024 aluminum rivets, where they reported that increases in the rotational speed led to higher levels of deformation at the tip of the rivet.

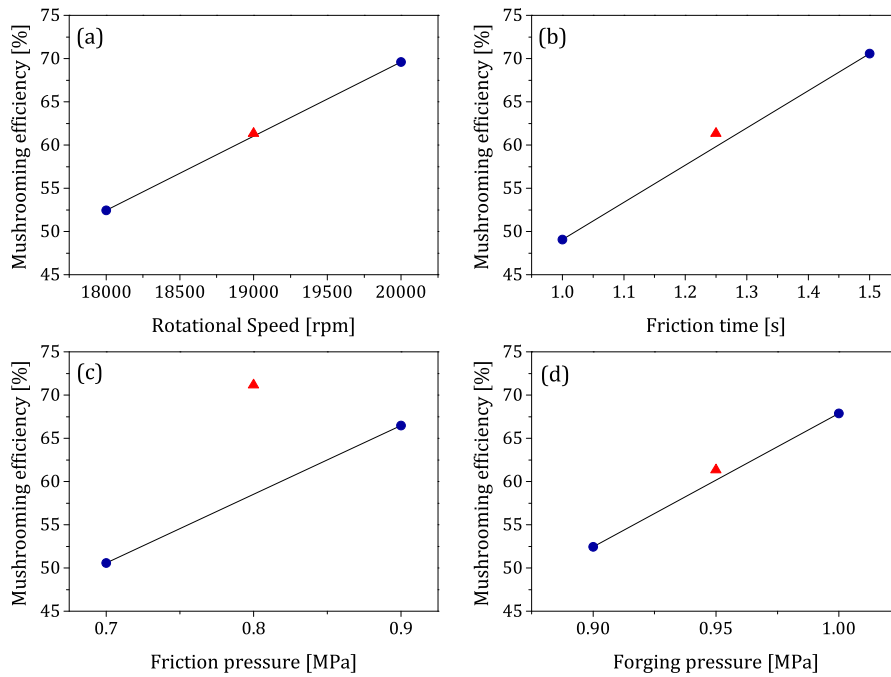


**Figure 6.2.** Main effects plots and relationships between the riveting conditions and mushrooming efficiency for (a) RS, (b) FT, (c) FP, (d) FoP

The mushrooming efficiency increases with FP, reaching a maximum response of approximately 70% at 0.8 MPa (i.e. the centre point, Figure 6.2 c). This trend might indicate a nonlinear correlation between the FP and mushrooming efficiency. The highest mushrooming efficiency (approximately 70% in the main effects plot) was obtained at an FP of 0.8 MPa; exceeding this threshold cannot increase the mushrooming efficiency due to the deformability of the titanium, which is somewhat limited and is independent of additional energy provided. The widening of the rivet tip by 70% of its initial diameter appears to be the upper limit of deformability, regardless of the additional mechanical energy introduced into the joint.

An analysis of variance (ANOVA) carried out on this data set showed that the studied process parameters significantly influenced the mushrooming efficiency ( $p$ -value for RS, FT, FP and FoP was 0.000) and the second-order interactions  $RS*FT$ ,  $FT * FP$  ( $p$ -value: 0.000) and  $FP * FoP$  ( $p$ -value: 0.001) with an error rate  $\alpha$  of 5%. The significance of a factor or an interaction on the response being examined



is described by its  $p$ -value. An effect is considered insignificant if  $p > 0.10$ , mildly significant if  $0.05 < p < 0.10$  and significant if  $p < 0.05$  [88, 89].

### 6.2.2. Rivet penetration depth

The results obtained for rivet penetration depth are listed in Table 6.3. Penetration depth varied between 7.9 mm and 12.6 mm. The main effects plots in Figure 6.3 display the effect of the process parameters on the rivet penetration depth. Only RS, FT and FP had a pronounced impact on the rivet penetration depth. Increasing the RS and FT over the investigated parameter range increased the rivet penetration depth (Figure 6.3 a, b and d). Increasing RS and FT increased the energy input, melting a larger volume of polymer around the rivet to enable a higher penetration depth. This is in accordance with the observations previously discussed in [50]. Those authors showed that the higher the thermal energy is, for instance as a result of increased RS, the larger the penetration depth will be. The FP peaked at an intermediate level (0.8 MPa), as demonstrated in Figure 6.3. Therefore, a nonlinear dependency exists between the FP and the rivet penetration depth. Consequently, FP exceeding 0.8 MPa usually does not increase the rivet penetration depth, and Figure 6.3 c shows a plateau for the penetration depth starting at 0.8 MPa. This occurs because there are no large changes in the penetration depth for the investigated parameter combinations, suggesting that, within this energy input range, the penetration depth cannot be increased further for the configurations that were studied. Figure 6.3 suggests that, to obtain significant increases in penetration depth, RS and FT should be selected at levels above the parameter range investigated in this study. The main effects plots also show that the FoP has no significant impact on the rivet penetration depth for the chosen parameter range.

The ANOVA performed with the acquired data set confirmed the significant impact of RS, FT and FP (RS, FT and FP  $p$ -value of 0.000) on the rivet penetration depth and the second-order interactions  $RS*FP$  ( $p$ -value of 0.011) and  $FP*FoP$  ( $p$ -value of 0.024). The relevance of  $RS*FP$  and  $FP*FoP$  is associated with the combined contributions of the individual variables on heat generation and polymer melting; the higher the heat generated and the axial pressure applied, the easier the rivet insertion will be. The ANOVA was performed using the error rates indicated above.

### 6.2.3. Mechanical energy input

The mechanical energy input was calculated from Equation 2.3; the resulting energy input values are listed in Table 6.3. Depending on the process parameter combination, the energy input varied between 685 J and 1525 J. The relationship between the process parameters and the mechanical energy input are shown in the main effects plots in Figure 6.4. RS, FT and FP exerted a pronounced effect on the energy input; the higher these parameters were, the higher the energy input was. Equation 2.2 accounts for this behaviour, since increasing RS, FT or FP increases the

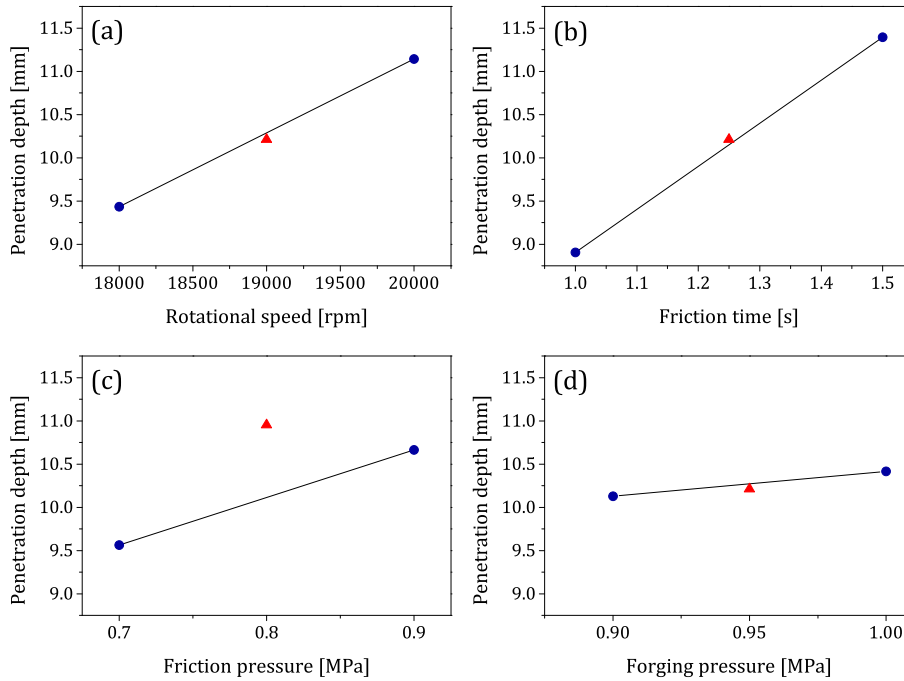


**Figure 6.3.** Main effects plots showing the relationships between the riveting conditions and rivet penetration depth: (a) RS, (b) FT, (c) FP, (d) FoP

energy input. The effect of the FP was slightly less significant than that of RS and FT due to the contribution of normal forces resulting from the FP, thus exerting a less pronounced effect on heat generation. The increase in the mechanical energy input was also related to the increase in RS, corresponding to the results found by Amancio-Filho *et al.* [50]. At higher rotational speeds, the internal shearing was also higher (through viscous dissipation), leading to a higher energy input. The increase in mechanical energy input is related to the increase in FT because the longer the FricRiveting process takes, the longer the mechanical energy is generated. However, the FoP main effects plot shows almost no variation in the energy input within the investigated FoP range because the forging step generally does not contribute to the mechanical energy input. The RS reached zero shortly after forging began, and the heat production was almost null during forging (see Equations 2.2 and 2.3).

These findings were also validated by the ANOVA performed on this data set. RS, FT and FP ( $p$ -value 0.000) significantly influenced the energy input and the second-order interactions, especially  $RS * FT$  ( $p$ -value 0.000) and  $RS * FP$  ( $p$ -value 0.000).

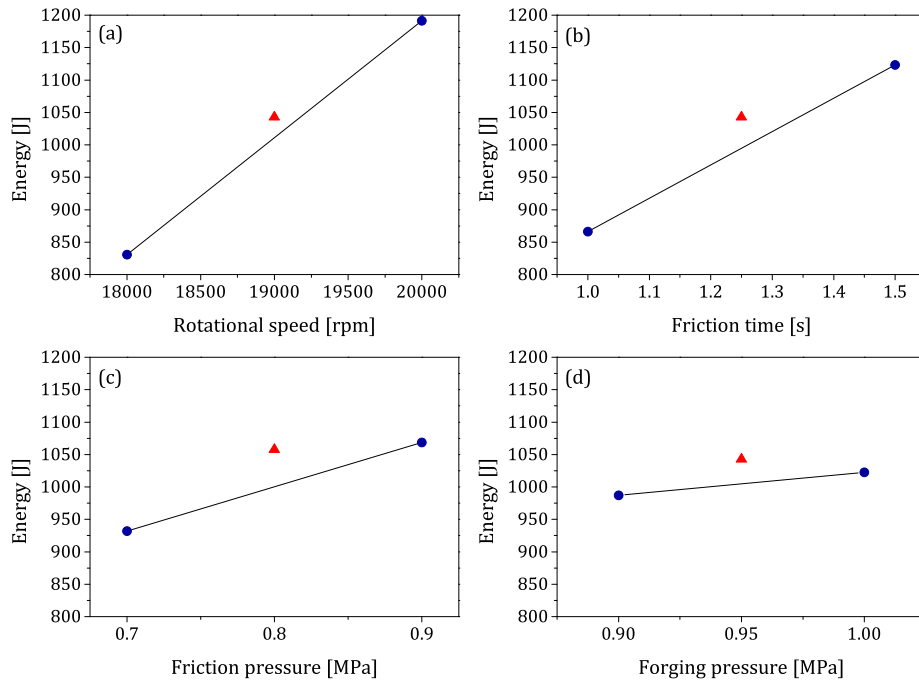


**Figure 6.4.** Main effects plots showing the relationship between riveting conditions and energy input: (a) RS, (b) FT, (c) FP, (d) FoP

### 6.3. Influence of the process parameters on joint performance

The effects of the four process parameters RS, FT, FP and FoP on the joint mechanical performance are now examined by analysing the impact of the process parameters on the pull-out force.

#### 6.3.1. Ultimate pull-out tensile force

The ultimate tensile forces for all of the tested specimens are given in Table 6.3. Depending on the combination of process parameters, the results varied from 6.3 kN to 10.7 kN. When analysing the main effects plots in Figure 6.5, it was seen that the pull-out force followed a trend similar to that of the mushrooming efficiency in Figure 6.2, indicating a relationship between the geometry of the deformed titanium rivet tip inside the reinforced polymer and the mechanical performance of the metallic-insert joint, which is consistent with the findings for unreinforced PEI/Al 2024 [25] and glass fibre-reinforced PEI/titanium grade 2 metallic insert joints [53, 86]. This correlation will be discussed further in Section 6.5. Figure 6.5 shows the significance of all four process parameters on the ultimate tensile force.

## 6. Relationship between process, microstructure and mechanical performance

Higher RS, FT and FoP resulted in higher pull-out force. In Equation 2.2, increases in RS, FT and FoP yield higher mechanical energy input values, leaving additional heat available for deforming and widening the rivet tip. Thus a more widely deformed rivet tip (mushrooming efficiency) is reflected by a larger volume of polymer above the deformed rivet tip and more force is then required to pull the rivet out of the composite substrate. The deviation in the mean value of the intermediate level of the FP indicates a nonlinear relationship between FP and pull-out force.

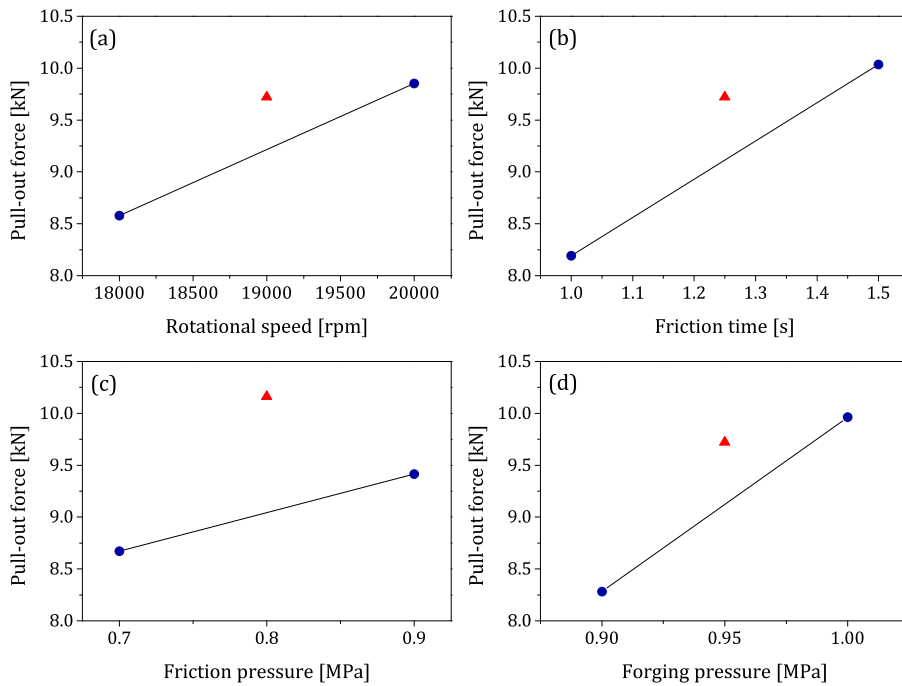


**Figure 6.5.** Main effects plots showing the relationship between the riveting conditions and pull-out force: (a) RS, (b) FT, (c) FP, (d) FoP

These observations were also supported by the ANOVA, which confirmed the significant effect exerted by all four process parameters ( $p$ -value for RS, FT, FP and FoP was 0.000) on the pull-out force and a pronounced influence of the second-order interactions  $FT * FoP$  ( $p$ -value of 0.001) and  $RS * FT$  ( $p$ -value of 0.022).

The summary of the four main effects plots of the effects of the process parameters on joint formation and performance provided the opportunity to define an optimized parameter set for the process that would increase the mushrooming efficiency and the pull-out force. In such an optimized parameter set, RS, FT and FoP must be at high levels (RS: 20000 rpm, FT: 1.5 s, FoP: 1 MPa), while FP should be at an intermediate level (FP: 0.8 MPa), since these were the levels giving the highest mushrooming efficiency. Since this parameter set was not part of the DoE analysis,

three samples were produced and tested to validate the findings and the results were compared with the conclusions drawn from the main effect plots.

Metallic-insert joints were produced using the optimized process parameter set. The mechanical energy was also calculated using Equation 2.3 and, in order to measure the penetration depth and the widening of the rivet tip prior to mechanical testing, the specimens were X-rayed as described in Section 4.5. In the next step, the pull-out performance of each joint was analysed and compared with the strength of the grade 3 titanium of which the rivet was made. The tests were performed using the arrangement and procedure described in Section 4.8.1.

The results are reported in Table 6.4 and the resulting force–displacement curves of the metallic-insert joints and the titanium base material are shown in Figure 6.6. The graph shows that the pull-out performance of the metallic-insert joints is almost identical to the tensile strength of the grade 3 titanium base material. The average ultimate tensile strength of the base material and the joints both reached 10.6 kN. Therefore, the optimized process parameter set resulted in a metallic-insert joint showing base material strength and toughness, which are always the desired outcome for a joining process.

**Table 6.4.** Test results for specimens using the optimized parameter set (RS: 20000 rpm, FT: 1.5 s, FP: 0.8 MPa and FoP: 1 MPa), configuration 0

Joint formation			Joint performance
$E_{\text{mech}}$ [J]	$T$ [mm]	$e_{\text{mush}}$ [%]	$F_{\text{pull-out}}$ [kN]
$1185 \pm 12$	$12.9 \pm 0.56$	$91.4 \pm 0.11$	$10.6 \pm 0.09$

These results basically confirmed the expected behaviour and tensile loading. The specimens friction-riveted using the optimized process parameter combination resulted in a high mushrooming efficiency of 91.4%. Only one configuration in the initial study gave a slightly higher mushrooming efficiency (93.6%): that is, configuration 4 (RS: 20000 rpm, FT: 1.5 s, FP: 0.9 MPa and FoP: 1 MPa). Configuration 4 also showed a higher standard deviation (1%) than the optimized configuration (0.11%), making the optimized configuration the more robust process parameter combination that still led to a very high mushrooming efficiency. Moreover, configuration 4 produced a much higher energy input ( $E_{\text{mech}} = 1525$  J) than the optimized combination ( $E_{\text{mech}} = 1185$  J), which may increase the risk of larger volumes of thermally affected polymer matrix and thus a higher degree of thermal degradation of the matrix.

The characterisation of the metallic-insert joints produced using the optimized process parameter combination is presented in Section 6.6. This includes a microstructural analysis, an assessment of the thermomechanical impact on the joint, and an assessment of the global mechanical performance.

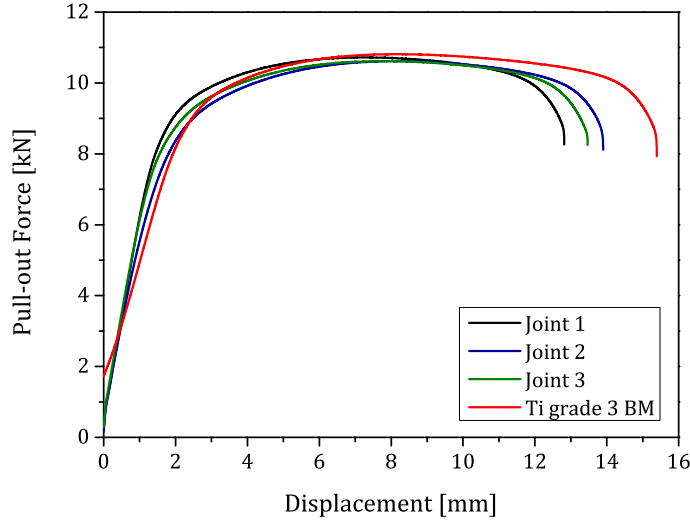


**Figure 6.6.** Force–displacement curves for the rivet base material and the metallic-insert joints, friction riveted using the optimized process parameter set (configuration 0)

The optimized metallic-insert joints failed in failure mode I, the “through the rivet” failure (Figure 6.10 b in Section 6.5). A summary of the failure modes reported for FricRiveting in the literature is given in Section 2.2.8. Failure mode I is the preferred failure mode, since failure occurs outside the joining region and the joints fail at high applied forces close to the strength of the rivet base material itself [54].

#### 6.4. Statistical model validation

The acquired data sets were analysed using parametric analyses of variance (ANOVA) to validate statistical models used to evaluate the impact of the process parameters on the properties of the joints. The four responses were analysed separately. Therefore, the dependent variables were the mushrooming efficiency, the penetration depth, the mechanical energy and the pull-out force; RS, FT, FP and FoP were the independent variables. The ANOVA model was modified to include the independent variables and the relevant second-order interactions. Regression analysis of the collected data could then be used to predict the impact on the responses as a function of the significant process parameters and their interactions. The multiple regression equation used was a two-way interaction, Equation 6.1:

$$R = \beta_0 + \beta_1x_1 + \beta_2x_2 + \beta_3x_3 + \beta_4x_4 + \beta_{12}x_1x_2 + \beta_{13}x_1x_3 + \beta_{14}x_1x_4 + \beta_{23}x_2x_3 + \beta_{24}x_2x_4 + \beta_{34}x_3x_4 \quad (6.1)$$

where  $R$  is the response (mechanical energy input, penetration depth, mushrooming efficiency and pull-out force), while the predictor variables include rotational speed ( $x_1$ ), friction time ( $x_2$ ), friction pressure ( $x_3$ ) and forging pressure ( $x_4$ ). The effect of the different factors and their interactions on the four responses are shown in the Pareto charts in Figure 6.7. The effects of all of the factors and their interactions were standardised (i.e. each effect was divided by its standard error). The length of each bar in the charts is directly related to the absolute value of its associated regression coefficient; the ordering of the factors corresponds to the size of its effect, starting with the factor having the greatest influence on the evaluated response. The vertical line in each Pareto chart corresponds to the 95% limit indicating statistical significance. Therefore, the effect of a factor is considered significant if its corresponding bar crosses this line. The multiple regression equations for the responses, including only the significant process parameters and interactions, are:

$$E_{\text{mech}} = 8174 \text{ J} - 0.44 \text{ J min} * RS - 2.94 \frac{\text{J}}{\text{ms}} * FT - 889 \frac{\text{J}}{\text{bar}} * FP + 0.0506 \frac{\text{J min}}{\text{ms}} * RS * FP + 0.00018 \frac{\text{J min}}{\text{ms}} * FT * RS \quad (6.2)$$

$$T = -16.7 \text{ mm} + 0.000861 \text{ mm min} * RS + 0.00483 \frac{\text{mm}}{\text{ms}} * FT + 0.55 \frac{\text{mm}}{\text{bar}} * FP \quad (6.3)$$

$$e_{\text{mush}} = -31.5 \% - 0.00009 \% \text{ min} * RS - 0.198 \frac{\%}{\text{ms}} * FT - 8.86 \frac{\%}{\text{bar}} * FP + 12.2 \frac{\%}{\text{bar}} * FoP + 0.0134 \frac{\%}{\text{bar ms}} * FT * FP + 0.0506 \frac{\% \text{ min}}{\text{bar}} * RS * FP + 0.000007 \frac{\% \text{ min}}{\text{ms}} * FT * RS \quad (6.4)$$

$$F_{\text{pull-out}} = -49.7 \text{ kN} + 0.000723 \text{ kN min} * RS + 0.0221 \frac{\text{kN}}{\text{ms}} * FT + 0.371 \frac{\text{kN}}{\text{bar}} * FP + 3.98 \frac{\text{kN}}{\text{bar}} * FoP - 0.00197 \frac{\text{kN}}{\text{ms bar}} * FT * FoP \quad (6.5)$$

The individual regression equations contain only the factors proven to be significant by using their  $p$ -values and the Pareto charts in Figure 6.7. The scatter plots in Figure 6.8 compare the predictions calculated from the above equations with the measured data for all four responses. The 45° line in Figure 6.8 represents a perfectly linear relationship between the measured and the predicted data, as well as the ±10% deviation lines commonly used during polymer welding. A standard deviation

6. Relationship between process, microstructure and mechanical performance

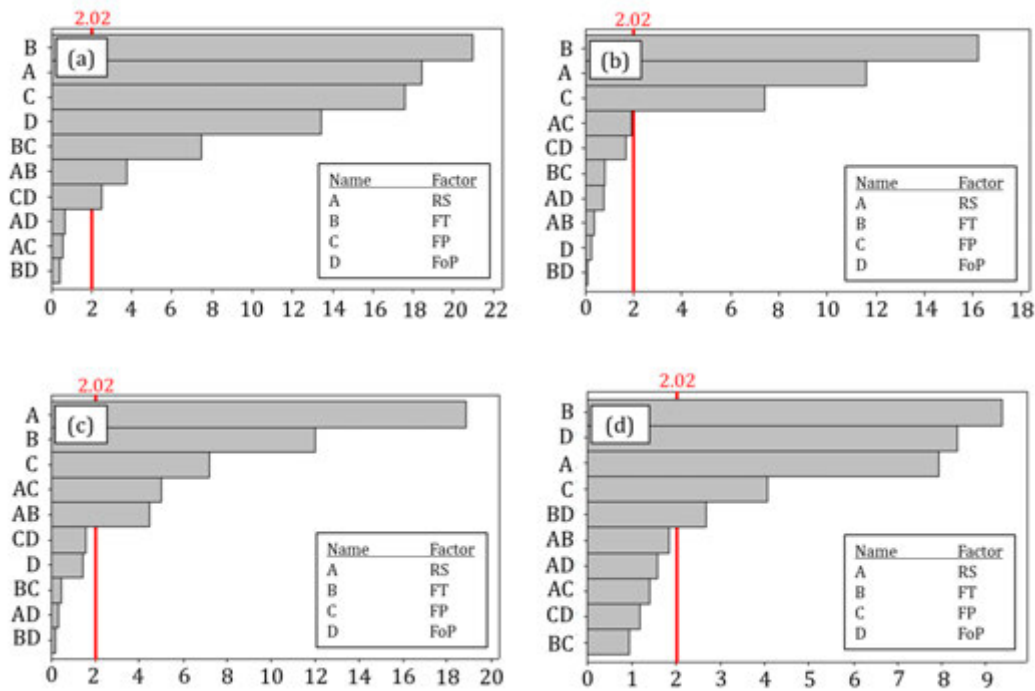


**Figure 6.7.** Pareto charts of the standardised effects for (a) mushrooming efficiency; (b) penetration depth; (c) mechanical energy; (d) pull-out force

of 10% is a common value associated with the mechanical property variations in different production batches of the same plastic part.

An hypothesis test of the regression analysis was performed at an error rate of 5%. Figure 6.8 showed good agreement between predicted and measured data for all four responses, as fitted by the linear relationship between the measured and predicted data sets. This result proved that the regression equations Equations 6.2 to 6.5 could be used to predict mushrooming efficiency, rivet penetration depth, mechanical energy input and pull-out force as a function of the significant process parameters and their first-order interactions. The accuracy levels of the predictions are given in Table 6.5. Equations 6.2 to 6.5 gave very good accuracy levels, varying between 80.7% and 96.1%.

**Table 6.5.** Accuracy levels of mechanical energy input, penetration depth, mushrooming efficiency and pull-out force predicted by their respective regression equations

Response	$E_{\text{mech}}$ [J]	$T$ [mm]	$e_{\text{mush}}$ [%]	$F_{\text{pull-out}}$ [kN]
Accuracy level [%]	92.4	90.0	96.1	80.7



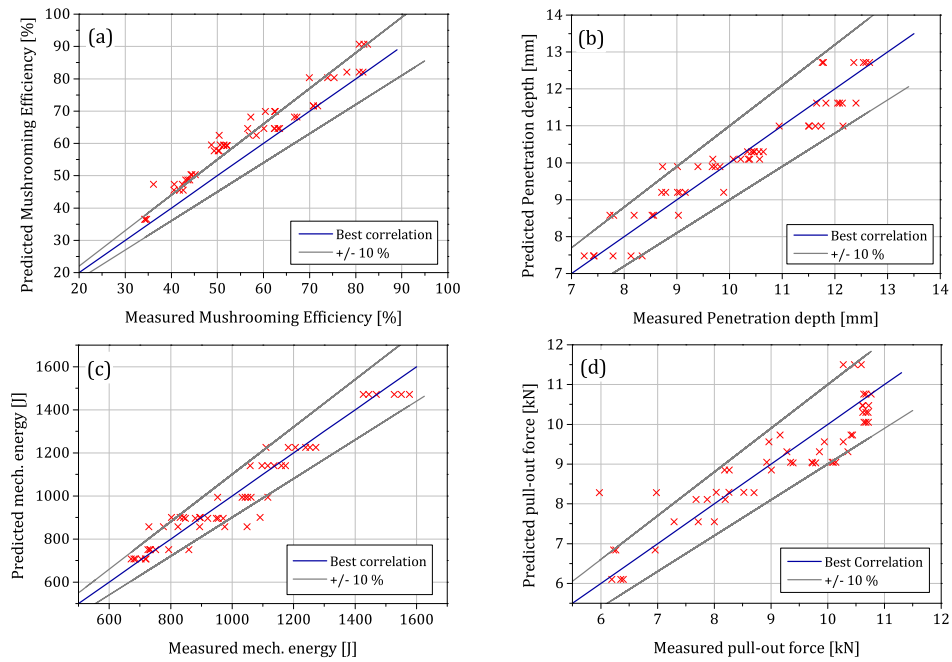


**Figure 6.8.** Predicted vs. measured responses for: (a) mushrooming efficiency; (b) rivet penetration depth; (c) mechanical energy input; and (d) pull-out force

## 6.5. Influence of rivet anchoring performance on tensile strength

The main effects plots for mushrooming efficiency and pull-out force (Figures 6.2 and 6.5) show similar trends, suggesting a relationship between these two responses. Figure 6.9 presents the relationship between mushrooming efficiency and pull-out force, indicating that a wider rivet tip requires a greater pull-out force. Rodrigues *et al.* [52] demonstrated that the tensile load at failure of metallic-insert joints made of polycarbonate and AA2024 was mainly influenced by the size of the anchoring feature inside the polymer substrate. The implication that greater mushrooming efficiency leads to a higher pull-out strength was, however, only valid up to a mushrooming efficiency of 70% for the material combination in this study. Exceeding this mushrooming efficiency threshold did not further increase the pull-out strength, which reached a plateau at 10.6 kN, the ultimate tensile strength of titanium grade 3 rivets (Figure 6.9).

Furthermore this threshold and the formation of the plateau are also associated with a change in the failure mode from “full rivet pull-out” (failure mode III) to “through the rivet” failure (failure mode I): see Figure 6.10. These failure types were observed

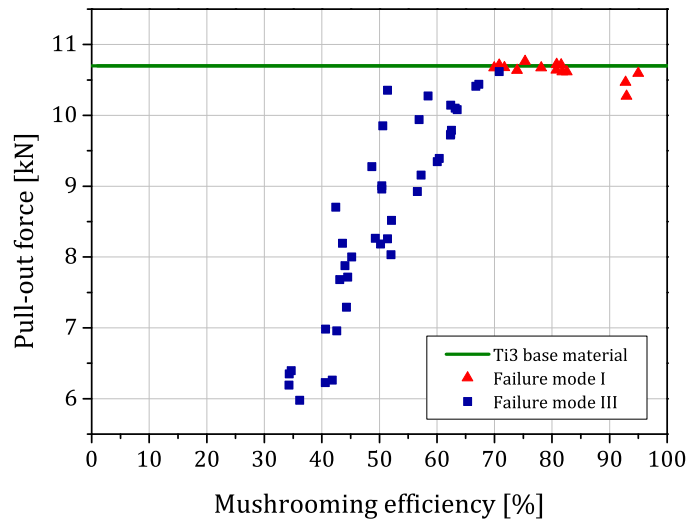


**Figure 6.9.** Relationship between mushrooming efficiency and pull-out force, including the observed failure modes of the joints

in previous studies of unreinforced polymer/aluminium [51] and GF-PEI/grade 2 titanium ([52] and [53]). As described in Section 2.2, the “full rivet pull-out” failure (failure mode III, Figure 6.10 a) is a fracture mode typically found in highly ductile joints, or where the deformation of the rivet is relatively low (corresponding to low mushrooming efficiency), leading to lower mechanical strength of the joint. For failure mode III, lower mushrooming efficiency implies lower pull-out force; the pull-out force of joints exhibiting failure mode III is always lower than for joints that fail in mode I (Figure 6.10 b). Failure mode I, “through the rivet” failure, corresponds to ductile fracture of the rivet outside the joint. The maximum tensile strength of the joint (high mushrooming efficiency) is similar to the base material strength of the titanium rivet (Figure 6.9).

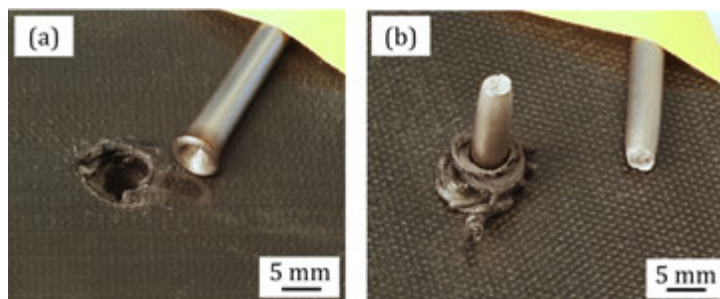


**Figure 6.10.** Failure modes of the metallic-insert joints: (a) “full rivet pull-out” (pull-out of the deformed Ti rivet, failure mode III); (b) “through the rivet” (rivet failure in the Ti base material, failure mode I)

## 6.6. Thermal history, microstructure and local mechanical properties

It is known that the thermomechanical phenomena during FricRiveting affects the properties of the joining partners. The microstructure and the mechanical performance of FricRiveted joints are significantly influenced by the temperature history and high deformation rates experienced during the joining process. The influence of the FricRiveting process on the titanium rivet and on the composite substrate are addressed in this section by evaluating selected metallic-insert joints from the previous section. This section includes an investigation of the thermomechanical impact of the process by assessing the temperature evolution and the mechanical energy input during joining, the resulting microstructure and material flow related to the process. The degree of process-related thermal degradation in the PEEK-CA30 composite matrix is evaluated by thermal analysis.

### 6.6.1. Temperature evolution during joining

The base material properties of the polymer substrate and the metallic rivet affect the processing temperature. In addition to these is the mechanical energy input, and thereby the process parameters that are directly related to the temperature evolution during the FricRiveting process. The process temperature has been found to affect the softening and plasticising of the components to be joined [43]. This would be expected to result in structural changes of the materials [24].

The average peak process temperature of three different parameter configurations on the material combination of PEEK reinforced with 30% short carbon fibres and grade 3 titanium, was investigated by adopting the procedure described in Section 4.4. The three selected process parameters sets were configurations 0 (see Table 6.4), 4 and 14 (see Table 6.2) from the process optimisation study discussed in Section 6.2. These configurations were chosen because of their different energy-input levels to facilitate the analysis of the correlation between energy input and process temperature. Configuration 14 has the lowest energy-input level in this comparison (energy input of 685 J). Configuration 0 is the optimized process parameter set derived through the process development in Section 6.2, with an intermediate level of energy input (1185 J), and finally, configuration 4 has the highest energy-input level (1525 J).

The temperature measurement was carried out on the expelled composite flash. Amancio-Filho [24, 25] reported that, due to the low thermal conductivity of the polymer, the flash material has almost the same average temperature as the molten polymer layer around the plasticised rivet tip inside the polymer base plate. A typical infrared thermogram, extracted as a snapshot from an IR video acquired during joining, is shown in Figure 6.11. The image shows the temperature distribution over the flash material expelled during the process; the location of the measurement area is highlighted.

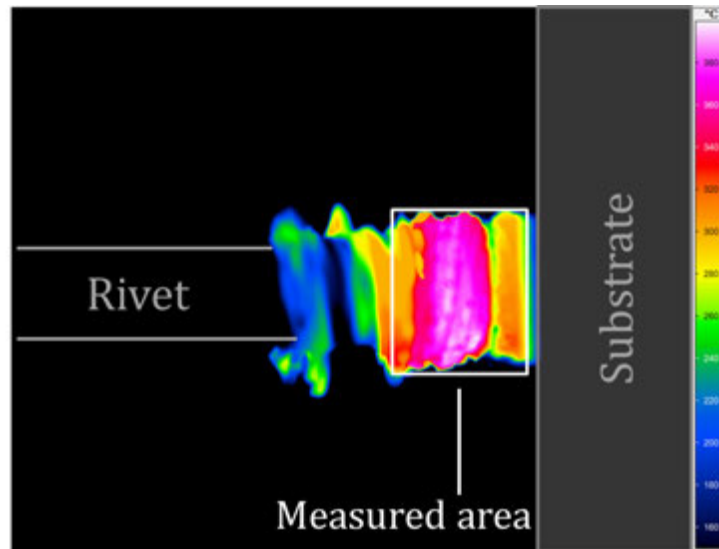


**Figure 6.11.** Thermogram (IR snapshot) showing the temperature distribution within the softened PEEK composite flash material being expelled from the joining region and pushed to the surface, and the location of the measurement area

An example of the temperature evolution during the process is shown in Figure 6.12 for configuration 4. The temperature evolution over time of the other two configurations are shown in Appendix E. The graph in Figure 6.12 shows that the heating rate is very rapid, since it is related to the short friction phase of the FricRiveting process. The peak process temperature is reached after approximately 1.5 s, corresponding exactly to the friction time that was set for this parameter configuration. Figure 6.12 also shows that the temperature then decreases at a very slow rate associated with the low thermal conductivity of the PEEK composite (see Table 4.4).

The average peak temperatures for the three joining configurations are presented in Table 6.6 and Figure 6.13. The mean peak temperatures varied between  $415\text{ }^{\circ}\text{C} \pm 9\text{ }^{\circ}\text{C}$  (for the configuration producing the lowest energy input) and  $478\text{ }^{\circ}\text{C} \pm 7\text{ }^{\circ}\text{C}$  (for configuration 4 representing the highest energy input). These temperatures are only 25% to 28% of the melting point of grade 3 titanium (see Table 4.3) but they are high enough to plasticise the titanium rivet and form the anchoring zone in the composite substrate. These temperatures, combined with the imposed plastic deformation, are also high enough to cause severe metallurgical changes in the titanium rivet (see discussion in Section 6.6.2). Such changes are consistent with observations of titanium joints reported for other friction-based joining processes [90].

PEEK is a thermally stable thermoplastic. The temperature of the onset of loss of mass associated with thermal degradation has been reported to vary from  $534\text{ }^{\circ}\text{C}$  to  $552\text{ }^{\circ}\text{C}$  [91]; however, appreciable losses of mass do not usually take place below  $700\text{ }^{\circ}\text{C}$  [92]. Therefore thermal degradation was not expected to be extensive in the

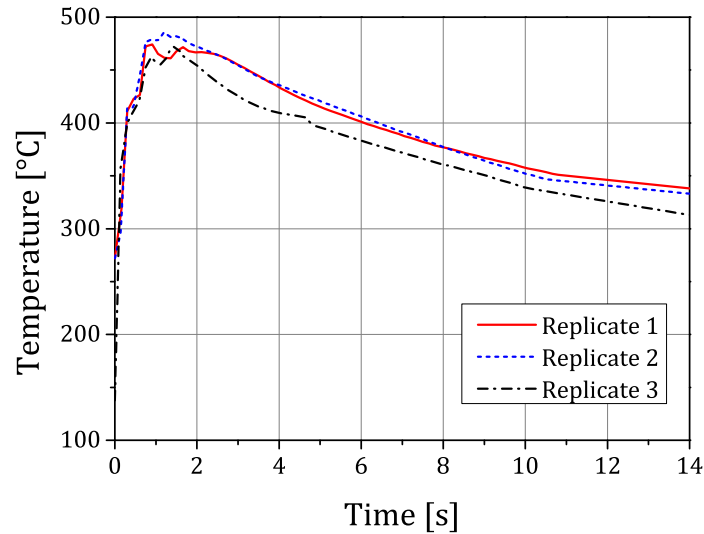


**Figure 6.12.** Example of the process temperature evolution during FricRiveting of a metallic-insert joint for configuration 4 (the configuration with the highest energy input; see table 6.2)

**Table 6.6.** Results of temperature measurements for the three configurations, with standard deviation and energy input

	Low energy level (configuration 14)	Medium energy level (configuration 0)	High energy level (configuration 4)
Temperature [°C]	$415 \pm 9$	$460 \pm 20$	$478 \pm 7$
$E_{\text{mech}}$ [J]	$685 \pm 14$	$1185 \pm 12$	$1525 \pm 44$

current study. Nevertheless, the process temperature exceeded  $334^\circ\text{C}$ , the melting point of the PEEK composite, so that certain changes in the physicochemical properties of the PEEK matrix, such as crystallinity, were expected. These phenomena will be discussed in Section 6.6.5.

Analysing the process temperature and the energy input of the three studied parameter sets together, a correlation was identified between them. Figure 6.13 shows that higher energy input produced higher temperatures, which is consistent with the findings of Amancio-Filho [25] who discussed the relationship between the peak temperature and the process parameters for PEI/AA2024 metallic-insert joints. He reported that increasing RS, FT and FP, which are associated with an increase of the energy input, also increased the peak temperature.

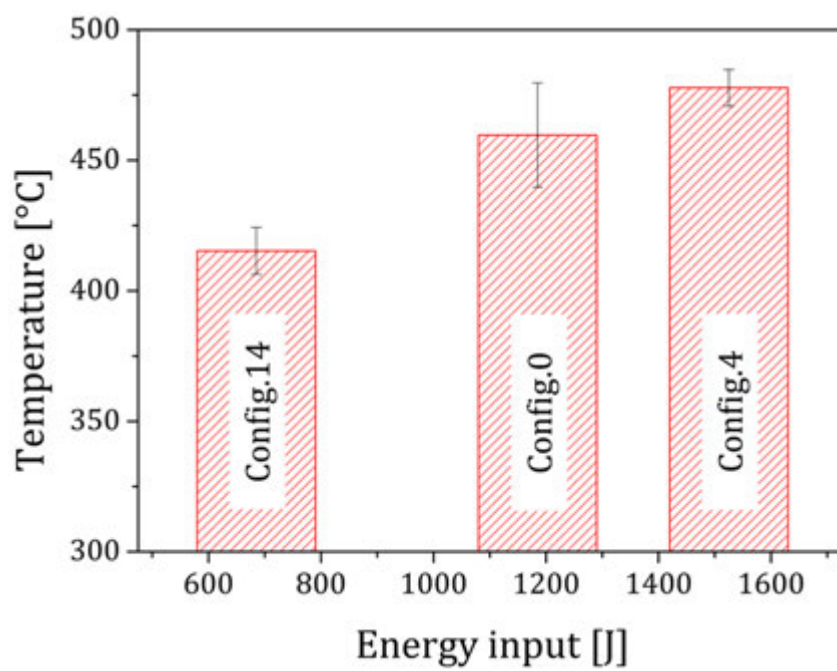


**Figure 6.13.** Correlation of energy input and the average process peak temperatures for configurations 14, 0 and 4 (from right to left)

### 6.6.2. Microstructural analysis of the titanium rivet

As discussed in the previous section, the tip of the titanium rivet undergoes a severe plastic deformation regime at high deformation rates and elevated temperature during the FricRiveting process resulting in a mushroom-shaped anchoring of the metallic rivet inside the carbon fibre-reinforced polymeric base plate, see Figure 6.14. It is shown in Figure 6.14 that the diameter of the rivet inside the composite increased from the initial diameter  $D$  of 5 mm to  $D_1$  of 5.4 mm in the proximity of the anchoring zone. This phenomenon, known as “barreling” [93], is also seen in hot forging. Barreling is a thickening of the specimen and has also been observed in commercially pure titanium deformed under hot compression [94]. This behaviour can most likely be explained by the axial force prevailing during the process causing hot compressive deformation during the FricRiveting process associated with the heat generated by the rotation of the rivet and the axial pressure applied to it. In order to better understand the evolution of the microstructure due to the FricRiveting process, detailed microstructural data was obtained from the areas indicated in Figure 6.14.

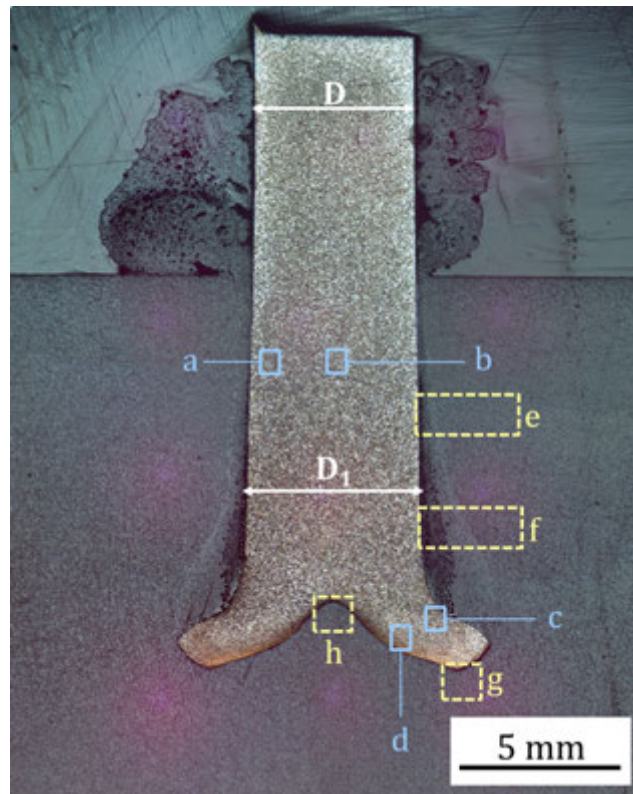


**Figure 6.14.** LOM from the mid-cross-section of a metallic-insert joint, showing the locations of areas a, b, c and d in the rivet and e, f, g and h in the PEEK composite

An EBSD map of the microstructure of the titanium rivet base material is shown in Figure 6.15. The grains are coloured according to their crystallographic orientation; the orientation code triangle is shown in the bottom right-hand corner (Figure 6.15 a). One can observe that the microstructure consisted of fine and large equiaxed alpha titanium grains with an average grain size of approximately 22.5  $\mu\text{m}$ . The structure of the base material shows a high density (95%) of high-angle boundaries (HABs) indicated in black in Figure 6.15. The fraction of low-angle boundaries (LABs) shown in light grey in Figure 6.15 is about 5%. A summary of the microstructural data obtained for regions a to d in Figure 6.14 is given in Table 6.7.

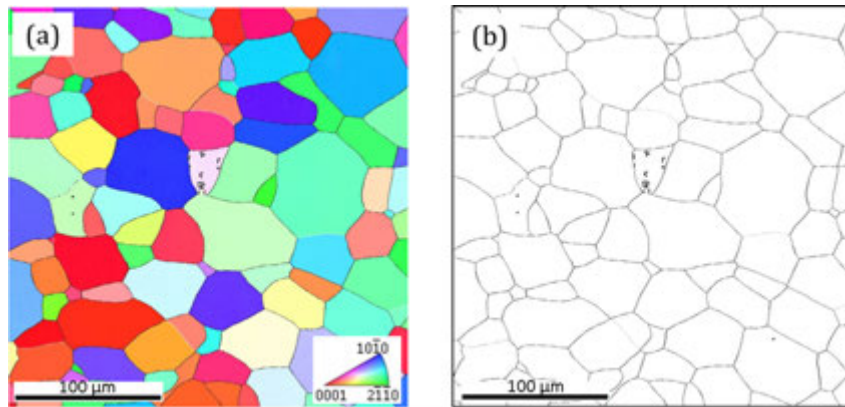


**Figure 6.15.** Microstructure of the grade 3 titanium base material of the rivet parallel to the extrusion direction: (a) grain boundaries and their crystallographic orientation, and (b) high-angle grain boundaries (dark lines) and low-angle grain boundaries (light grey lines)

**Table 6.7.** Average grain size and HAB fraction of the titanium base material and the regions shown in Figure 6.14

Microstructural region	Grain size [ $\mu\text{m}$ ]	HAB fraction [%]
Base material	22.5	95
Region a	5.5	71
Region b	5.5	71
Region c	4.7	25
Region d	0.7	47

The microstructure of areas a (the outer diametral region of the rivet) and b (centre of the rivet cross-section) can be seen in detail in Figures 6.16 and 6.17 respectively. The microstructural data derived from areas a and b (indicated in Figure 6.14) is given in Table 6.7. It is seen that the grain size and the HAB fraction are similar in both areas a and b, which indicates that the temperature was distributed evenly across the rivet diameter. Thus it was assumed that these regions were exposed to the same temperature and experienced the same degree of deformation. The par-



ent grains in these figures showed a large number of  $85^\circ \langle 1\bar{2}10 \rangle$  twin boundaries (indicated by red lines in Figures 6.16 b and 6.17 b) formed inside the grains, indicating the presence of  $\{10\bar{1}2\} \langle 1010 \rangle$  twins. Some of these  $85^\circ$  twin boundaries had begun to transform into random HABs due to the interaction with dislocations (some examples are pointed out by the black arrows in Figures 6.16 and 6.17) as observed in correlated friction-based welding process of commercially pure titanium [90]. Zeng *et al.* [94] reported that similar twinning was predominant in deformations up to 15% during hot compression of commercially pure titanium at temperatures up to  $450^\circ\text{C}$ . This temperature range is very close to the maximum temperature ( $T=478^\circ\text{C}$ , Section 6.6.1) recorded during the FricRiveting process. This type of twinning in the hexagonal structure accommodates the deformation, since such a structure lacks slip systems that would otherwise allow the deformation to take place [95].

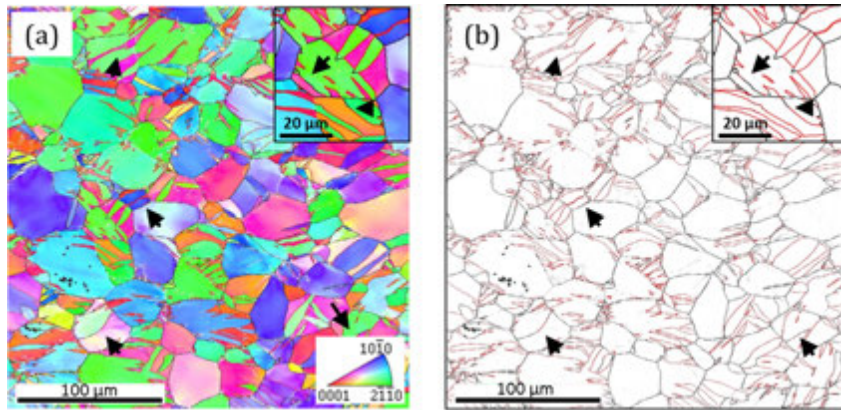


**Figure 6.16.** EBSD map showing the microstructure of region a, where (a) represents the grain boundaries including their crystallographic orientation and (b) represents only the grain boundaries

In addition, the proportion of LABs was observed to increase dramatically up to 29% due to dislocation activity. The formation of both  $85^\circ \langle 1\bar{2}10 \rangle$  twin boundaries and LABs reflects plastic compression-related deformation in these regions. The formation of twin boundaries led to a significant decrease in the average grain size to  $5.5\ \mu\text{m}$ . From this it is concluded that areas a and b may be characterised as metal thermomechanically affected zones (MTMAZ). These results are inconsistent with the findings in [25,43] which were that for PEI/AA2024 joints, no rivet barreling was observed in the rivet volume above the AZ; in other words no plastic deformation occurred in the region under investigation. Those authors defined the region where areas a and b are located as MHAZs, while MTMAZs were found at the edges and in the rivet AZ for the AA2024 rivet.

In area c, the parent grains were deformed in a specific direction, as shown in Figure 6.18. The formation of LAB boundaries inside the grains increased the number of LABs up to 75%, some of them being transformed into HABs, dividing the large grains into thinner lamellar grains as indicated by the black arrows in Figure 6.18.

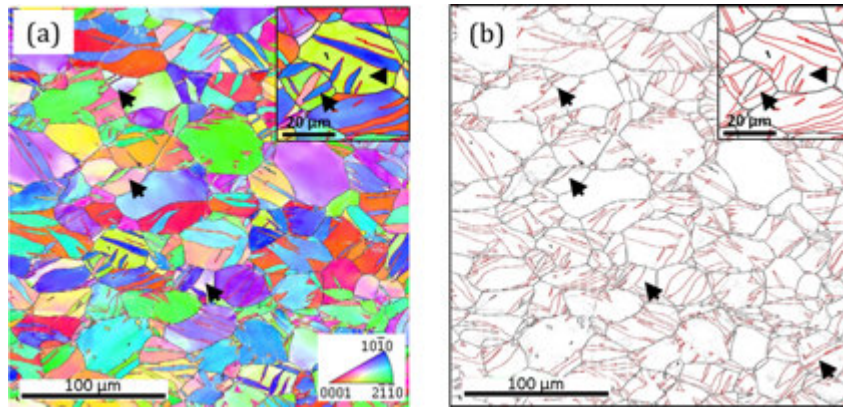


**Figure 6.17.** EBSD map showing the microstructure of region b, where (a) represents the grain boundaries including their crystallographic orientation and (b) represents only the grain boundaries

New small grains at the boundaries of large grains can be observed forming a “necklace” structure [90]. Most of the small grains contained an inner substructure, although some small grains with no substructure were also observed. The formation of the small grains with a substructure is probably due to the gradual increase of grain boundary reorientation. Grain boundary bulging was also observed, leading to the formation of small grains containing no substructure, evidence that the region had been exposed to high temperature [96]. Most of the  $85^\circ \langle 1\bar{2}10 \rangle$  twin boundaries were transformed into random HABs because of the interaction with dislocations; some examples are highlighted by the red arrows in Figure 6.18 [90]. Disappearance of the  $85^\circ \langle 1\bar{2}10 \rangle$  twin boundaries has also been observed in the microstructure of hot compressed specimens experiencing substantially high deformations and temperatures [94,97]. The average grain size in this region was reduced to  $4.7 \mu\text{m}$ . These findings indicate that this region experienced plastic deformation and was exposed to elevated temperatures during the FricRiveting process but only limited dynamic recrystallisation took place. The characterisation of this region indicates that area c was also within an MTMAZ. Therefore, the current findings have pointed out the presence of two distinct zones in the MTMAZ of the grade 3 titanium rivet, with areas a and b comprising MTMAZ-1 and area c the MTMAZ-2, whereby the former occurred within the AZ of the PEEK/grade 3 Ti joints.

In area d, the grain structure was transformed into a new microstructure with an average grain size of about  $0.7 \mu\text{m}$  (Figure 6.19). The figure shows that the microstructure was dominated by the fine grains and by irregular grains shown at the upper right-hand corner of the figure. The high proportion of LABs (53%) indicates that the region experienced plastic deformation. Grain boundary bulging, as well as small grains not containing LABs, indicate that discontinuous recrystallisation also took place during the FricRiveting process. The formation of a fine-grained structure is most likely due to recrystallisation induced by frictional heating and plastic deformation as a result of the friction between the rivet tip and the com-

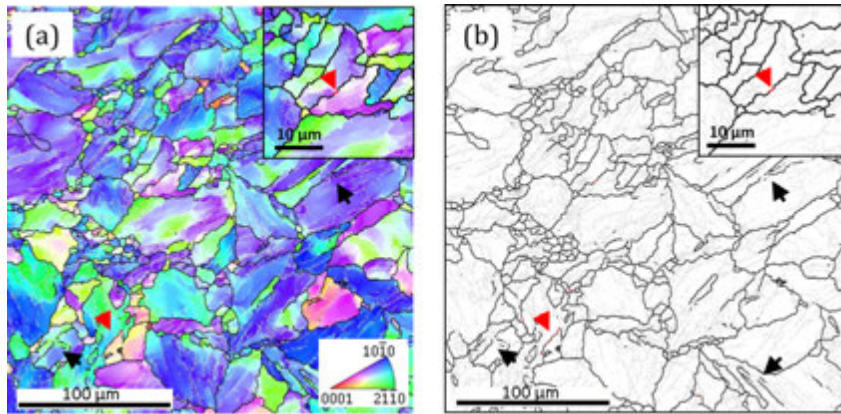


**Figure 6.18.** EBSD map showing the microstructure of region c, where (a) represents the grain boundaries including their crystallographic orientation and (b) represents only the grain boundaries

posite substrate; however, it is unclear which of these mechanisms was dominant. On the basis of the results obtained here, this region can be classified as the metal friction zone (MFZ), the zone where the friction between the metallic rivet and the PEEK composite substrate took place close to the surface of the rivet tip. The presence of a friction zone has also been proposed by Suhuddin *et al.* [98] in the friction surfacing of an aluminium alloy 6082-T6 rod on an aluminium alloy 2024-T351 substrate. Both processes are similar, in that the consumable material or rod (or rivet, in the FricRiveting case) rotates at high speed under pressure, rubbing the substrate surface and producing frictional heating at the contact interface of the rod end (or rivet tip) with the substrate.

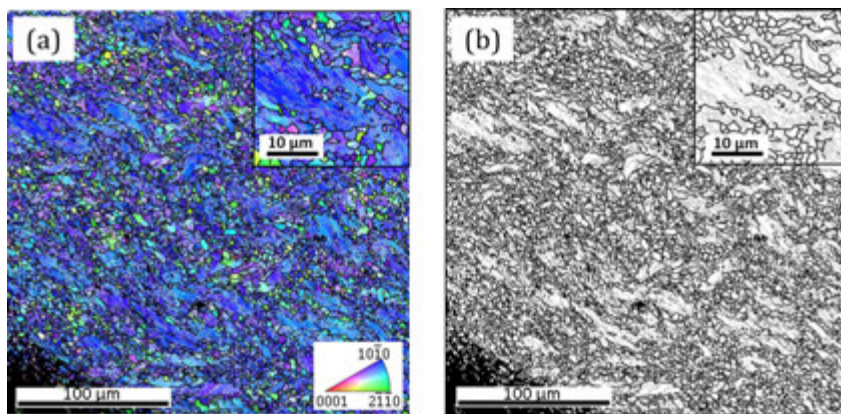


**Figure 6.19.** EBSD map showing the microstructure of region d, where (a) represents the grain boundaries including their crystallographic orientation and (b) represents only the grain boundaries

In order to obtain a detailed insight into the evolution of the microstructure, the calculated relationship between the misorientation angle and density of grain boundaries is presented in Figure 6.20. The grain boundary density is defined as the total boundary length in the region divided by the region area. The large deformation and high temperatures experienced during the process generated new high- and low-angle boundaries, as reported by [90] in friction-stir welding of pure titanium. It was also found that the misorientation angle changed progressively from the LABs towards the HABs, as shown in Figure 6.20. In areas a and b, an increase in the proportion of LABs and the formation of  $85^\circ \langle 1\bar{2}10 \rangle$  twin boundaries are seen, caused by the compressive deformation induced by the axial force applied to the rivet, as mentioned earlier. In area c, the number of LABs and HABs increased greatly at the same time as the  $85^\circ \langle 1\bar{2}10 \rangle$  twin boundaries vanished. This kind of change was mainly due to the interaction of the boundaries with the dislocations caused by the geometrical effect of strain induced by the forged mushroom-shaped head on the rivet. In area d, the number of boundaries progressively increased, as shown in Figure 6.20. It is likely that this phenomenon is related to the formation of deformation-induced boundaries and the subsequent accumulation of misorientation angles. Previous studies on friction-stir welding and friction surfacing of aluminum alloys [98] have interpreted this manner of progressive boundary movement in terms of continuous rather than discontinuous recrystallisation. From the present data, it is evident that continuous recrystallisation played an important role in the development of the microstructure of the rivets during the FricRiveting process.

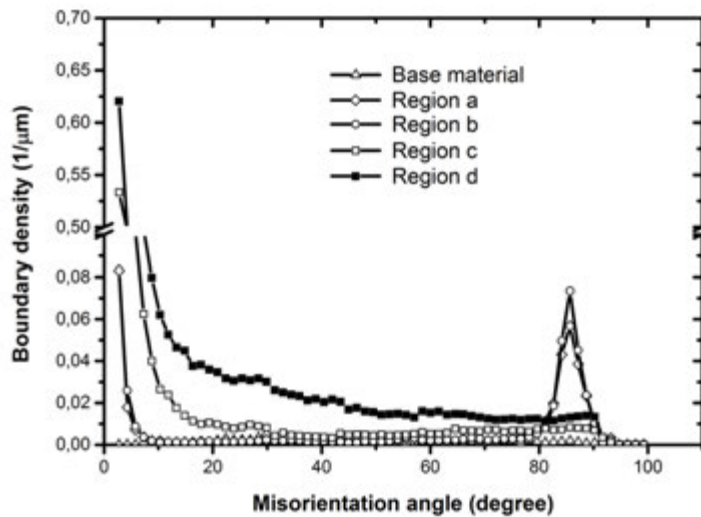


**Figure 6.20.** Grain boundary densities calculated for the base material and areas a, b, c and d

No metal heat-affected zones (MHAZ) were observed within the investigated joining area. There are two possible explanations for the absence or non-observation of this zone. First, it may be possible that the MHAZ had been shifted to the non-barreled

volume outside the composite substrate, meaning that there would be an MHAZ outside the investigated region. Alternatively, it may be argued that no MHAZ was formed by the FricRiveting process, simply a transition from the MTMAZ directly to the base material (BM). This latter phenomenon has been reported for other friction-based welding processes; for example Mironov *et al.* [90] described a direct transition from the MTMAZ to the BM in friction-stir welding of commercially pure titanium.

The observation of the microstructure in all of the investigated regions revealed that finer grain structures was indicative of a higher degree of deformation [94]. For example, the degree of deformation in area a is similar to that in area b, and the grain size and the HAB fraction are also similar in both areas. Additionally, the degree of deformation in area c was greater than in areas a and b, and the grains in area c were smaller, and the HAB fraction was lower, than in areas a and b. Area d experienced more severe deformation than areas a, b and c, and showed significant reduction of grain size. These results indicate that area d was highly affected by friction between the PEEK composite and the titanium rivet as a result of the increased temperature evolution at the composite–metal interface in the lower part of the metallic rivet tip.

### 6.6.3. Microstructural analysis of the PEEK composite

Amancio-Filho [25, 43] reported the presence of two different microstructural zones in the unreinforced polymer substrate of metallic-insert joints. These two zones, the polymer heat-affected zone (PHAZ) and the polymer thermomechanically affected zone (PTMAZ), were identified by their different exposures to temperature and deformation during the FricRiveting process. As a simplification, those authors associated the molten layer around the rivet with the PTMAZ, while the volumes of the polymer affected by heat but at temperatures below  $T_g$  (solid state) were associated with the PHAZ. No detailed investigation on material flow was carried out in that study. The microstructure of the PEEK-CA30 in the joining area in the present study was evaluated by LOM under reflective light as described in Section 4.6.1 to observe the presence of polymer degradation-related volumetric flaws from thermomechanical processing, and changes in fibre orientation as result of material flow. To better understand the microstructural evolution in the PEEK composite, detailed micrographs were taken of four areas (areas e, f, g and h) at the mid-cross-section of the metallic-insert joint, as indicated in Figure 6.14.

The microstructure of area e, located at the upper right-hand side region next to the metallic rivet in Figure 6.14 is shown in Figure 6.21. The microstructure of area f, located below area e in the lower region of the PEEK composite (Figure 6.14) is shown in Figure 6.22. Based on the morphology – that is, the porosity and fibre orientation of the PEEK composite – areas e and f (shown in Figures 6.21 and 6.22) were divided into four regions (regions 1 to 4).

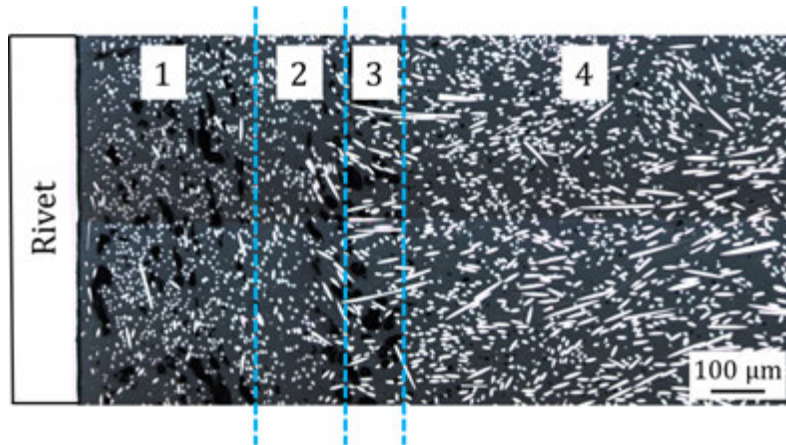


**Figure 6.21.** Detail of light optical micrograph of area e, shown in Figure 6.14

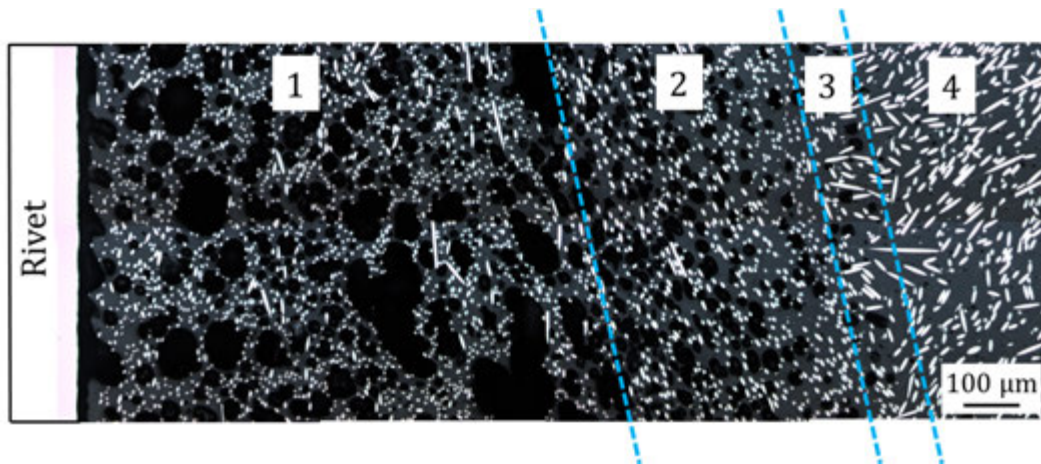


**Figure 6.22.** Detail of light optical micrograph of area f, shown in Figure 6.14

An enlarged map of region 1 in Figures 6.21 and 6.22 is shown in Figure 6.23 a. The porosity fraction in this region is higher than in the other three regions. The formation of pores resulted from the exposure to the high temperatures and shear rates close to the rotating rivet. The temperature in this region was well above  $T_g$  or  $T_m$ , which may have led to thermal degradation [41,43]. Most of the fibres in region 1 were realigned into a direction perpendicular to the observation plane, as can be seen in Figure 6.23 a by the dot-like circular appearance of the fibres. Figure 6.23 b is a schematic of the fibre orientation in region 1. It indicates that material flowed in a circular movement around the rivet (stirring), causing the fibres to be realigned parallel to the rivet as it rotated; region 1 was strongly affected by the rotation of the rivet in this way. From this evidence, region 1 was classified as the composite stir zone (CSZ). It should be noted that there is no evidence for significant changes in the microstructure of the cylindrical part of the rivet, as shown in areas a and b, which are the counterpart on the metallic side to region 1 in Figures 6.21 and 6.22.

The highest degree of deformation was observed in the vicinity of area d (within the titanium rivet). This indicates that, during the process, the main frictional heat was generated at the interface of the rivet tip and the composite material, and not at the surface area of the cylindrical part of the rivet.

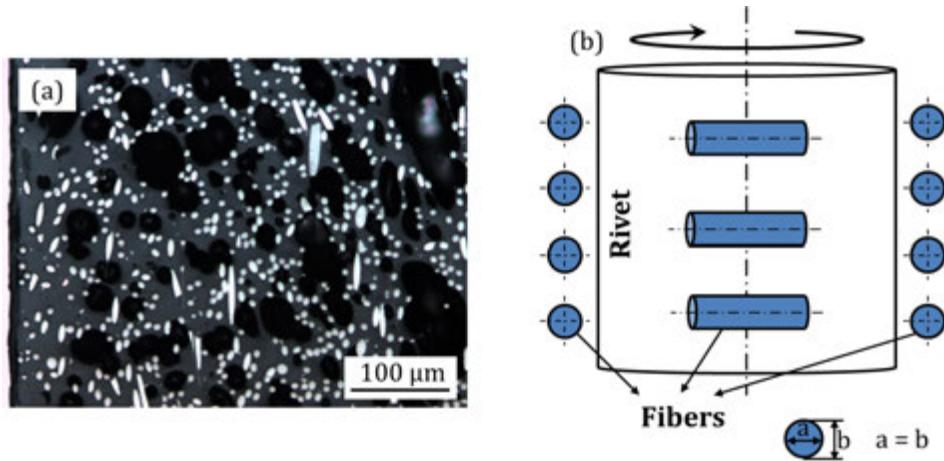


**Figure 6.23.** Composite stir zone (CSZ): (a) enlarged map of region 1, identified in Figures 6.21 and 6.22; (b) schematic of the fibre orientation in this region

An enlarged image of region 2 (Figures 6.21 and 6.22) is shown in Figure 6.24 a. The porosity fraction was lower than in the CSZ (region 1), indicating that the composite experienced lower temperatures here than in the CSZ. This can be explained by the fact that this region is further from the rotating rivet and, since the thermal conductivity of the PEEK substrate is low, the thermal impact on this region was also low. It is also seen that the fibres were reorientated such that they are seen in the cross-section as elliptical dots (Figure 6.24 a). The elliptical shape is the result of helical realignment, as shown in Figure 6.24 b. Two factors may have been responsible for this form of fibre orientation: the rotation of the rivet and the upward movement of the softened composite squeezed out by the penetration of the rivet.

First, rotation caused the fibres to move around the rivet and become realigned, as for the CSZ but to a lesser extent since this region was further from the rotating rivet and may have experienced lower temperatures; also the melting viscosity was probably higher. Second, the upward material flow of the molten composite as a result of the rivet penetrating the substrate and pushing this molten material towards the surface. The combination of these two factors led to the fibres being tilted as shown in the schematic presented in Figure 6.24 b. The details of the material flow inside the PEEK composite material will be discussed in Section 6.6.4. The findings show that this region experienced slightly lower temperatures and deformation rates than the CSZ; it was therefore classified as composite thermomechanically affected zone (CTMAZ). The presence of such a zone was also reported by Amancio-Filho [25,43],

but without the presence of a stirring zone, shown in this work by the difference in realignment of the short carbon fibres.

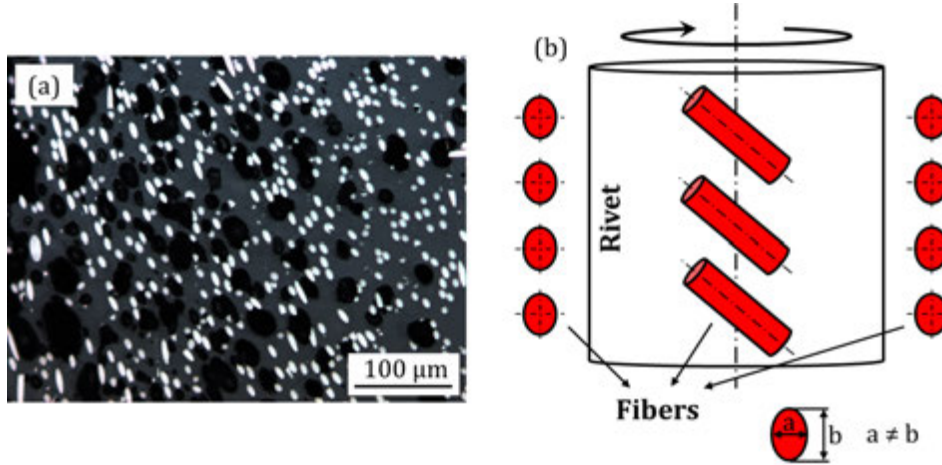


**Figure 6.24.** Composite thermomechanically affected zone (CTMAZ): (a) enlarged map of region 2, indicated in Figures 6.21 and 6.22; (b) schematic of the fibre orientation in this region

Comparing Figures 6.21 and 6.22, it is seen that both the CSZ and the CTMAZ in area f (Figure 6.22) were broader than in area e (Figure 6.21). This is possibly due to the differences in temperature experienced by the two areas. It is believed that the temperature was higher in area f than in area e, since it is likely that most of the heat was generated by friction between the tip of the rivet and the composite. Material closest to the heat source at the rivet tip would therefore be expected to show larger thermomechanically affected volumes.

Region 3, located between regions 2 and 4, was very narrow (Figure 6.25). The presence of pores indicate that, although the region had been exposed to high temperatures, the porosity fraction was much lower than in the CTMAZ and the CSZ. The local temperature affecting this region was probably lower than in the regions discussed above; the temperature was probably below  $T_m$  of the PEEK matrix, resulting in somewhat higher melting viscosities. The fibre orientation shown in Figure 6.25 differs from that in both the CSZ and the CTMAZ, and appears similar to the base material (see Figure 4.3). This implies that the fibre orientation in region 3 was not affected by either the rotation of the rivet or the upward flow of the softened composite. The information gleaned from the morphology of the analysed region showed that, while the matrix of the composite was affected by the elevated temperature (shown by the pores present in the microstructure), the fibres were not reorientated; therefore this region was identified as the composite heat affected zone (CHAZ).

Figure 6.26 is an enlarged micrograph of region 4 showing that the fraction of pores is minimal and the fibre orientation was similar, and therefore comparable, to the microstructure of the PEEK composite base material (see Figure 4.3). On the basis



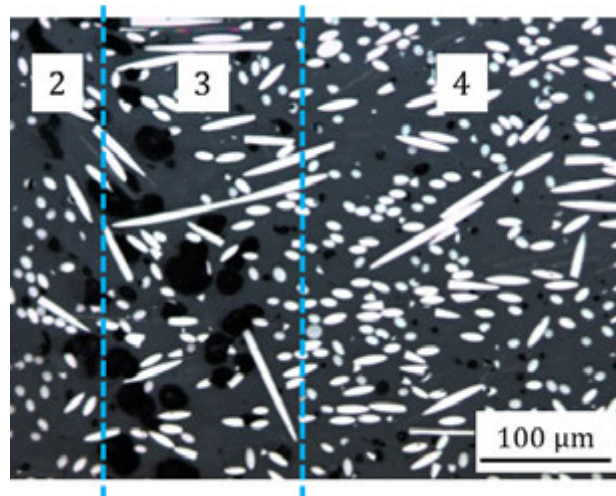


**Figure 6.25.** Enlarged map of region 3, the composite heat affected zone (CHAZ), located as shown in Figures 6.21 and 6.22

of the results obtained from the morphology, region 4 was classified as composite base material (CBM).

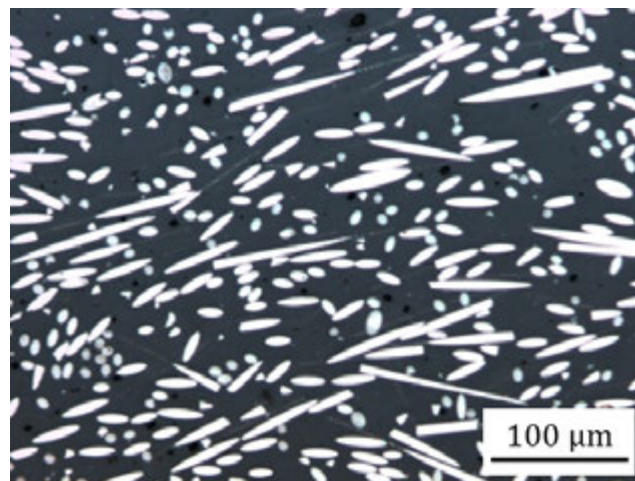


**Figure 6.26.** Enlarged map of region 4, the PEEK composite base material (CBM), located as shown in Figures 6.21, 6.22 and 6.27

To better understand the composite microstructure immediately beneath the rivet, areas g and f in Figure 6.14 were chosen for analysis. A gap can be seen in both areas between the rivet and the PEEK composite (indicated by a red arrow in Figure 6.27 and red broken lines in Figure 6.28). The gap was probably caused by the differential contraction (shrinkage) experienced by the materials during cooling. From the morphology of the PEEK composite, in particular the fibre orientation, each area was subdivided into two regions (regions 2 and 4). In region 2, the fibres

were reorientated, probably due to the material flow during the joining process. In area g, most of the fibres are seen to be aligned almost horizontally or parallel to the rivet surface. In region 2 of area h, most of the fibres were reorientated in a direction perpendicular to the observation plane. In both areas g and h, the porosity densities in regions 2 and 4 were identical. From this information, the evolution of the PEEK composite microstructure may be explained as follows.

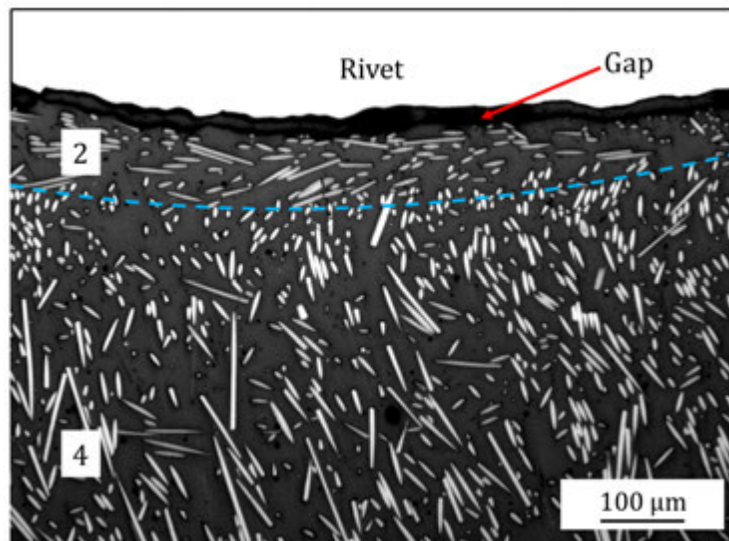


**Figure 6.27.** Higher-magnification micrograph of area g, which is located below the outer right-hand region of the deformed rivet tip, as shown in Figure 6.14

Figure 6.27 (area g) shows that the fibres in region 2 were reorientated and realigned following material flow in this region. The fibres were aligned almost horizontally in region 2, consistent with outward flow of the softened polymer during the forging step. The fibres are seen to be long and elongated, but they differ in appearance from those aligned parallel to the rivet. The reorientation in this case occurred as a result both of rotation and penetration of the rivet. During the forging step, increased axial force was applied to the rivet as rotation speed slowed, causing the material to flow outwards. This also explains the narrow region 2, the thermomechanically affected zone. The lack of porosity due to polymer degradation within the composite may be explained by the pressure experienced in this region leading to a displacement of the pores developed during joining as a result of the compressive state, which differs from the observations in areas e and f. The lack of pores due to the compressive state below the rivet also explains why it was not possible to observe and identify a composite heat affected zone (CHAZ) within areas g and h. In order to obtain detailed information on the microstructural changes, an intensive microhardness investigation would be required which is very difficult due to the fibre content; such analysis was not included within the framework of the thesis and will be a topic

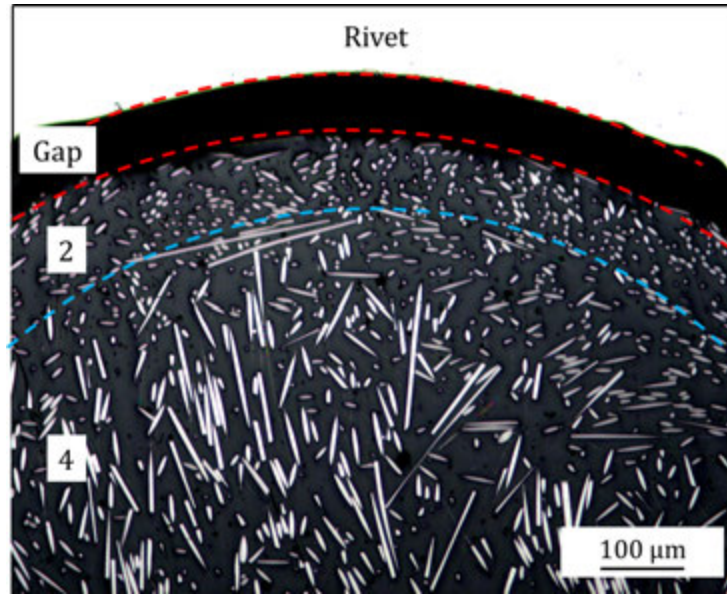


**Figure 6.28.** Higher-magnification micrograph of area h, which is located below the centre of the deformed rivet tip, as shown in Figure 6.14

for future work. The findings demonstrate that region 2 was exposed to elevated temperatures and experienced deformation; thus it was classified as CTMAZ [25,43].

In region 2 of area h (Figure 6.28), the fibres were reorientated and realigned as a result of the material flow. The orientation appears to be almost perpendicular to the observation plane. The fibres in the cross-sectional view resemble elliptical dots. Unlike region 2 of area g, however, the material is believed to have been only slightly affected by outward material flow, since it was trapped in the bell-shaped pocket created at the centre of the rivet tip by the forging action, and the fibres were tilted as shown in Figure 6.24. This indicates that region 2 was exposed to high temperatures and was considerably deformed; thus it was also characterised as CTMAZ [25, 43].

In areas g and h, region 4 was located beneath region 2. There is no evidence that region 4 contained more pores than the CBM (see Figure 4.3 b), or that the fibres had been reorientated. Considered together, these observations indicate that region 4 in areas g and h was neither heated to elevated temperatures nor deformed. Since no indication for differences from the composite base material were observed by studying only the morphology of these regions, region 4 was classified as CBM.

The reason for not being able to observe and identify a region 1, with a high level of pores, in areas g and h might be the compressive state due to the pushing action of the rivet, where degraded material was displaced upward during the forging step.

Summarising the findings from the microstructural analysis of the joining region, the schematic in Figure 6.29 is introduced to explain the microstructural zones found in the joints.

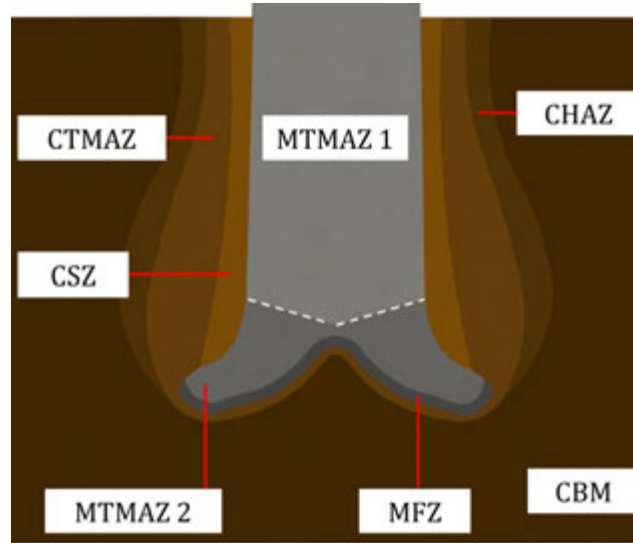


**Figure 6.29.** Schematic representation of the microstructural zones in friction-riveted joints: composite base material (CBM); composite heat-affected zone (CHAZ); composite thermomechanically affected zone (CTMAZ); composite stir zone (CSZ); metal thermomechanically affected zone 1 (MTMAZ 1); metal thermomechanically affected zone 2 (MTMAZ 2); and metal friction zone (MFZ)

Seven zones were identified in the vicinity of the joining area. In the composite, these are the composite base material (CBM), the composite heat-affected zone (CHAZ), the composite thermomechanically affected zone (CTMAZ) and the composite stir zone (CSZ). The zones identified in the rivet are the metal thermomechanically affected zone 1 (MTMAZ-1), the metal thermomechanically affected zone (MTMAZ-2) and the metal friction zone (MFZ). It was not possible to observe the precise shape and location of the boundary between the MTMAZ-1 and MTMAZ-2, using the LOM from the mid-cross-section of the metallic-insert joint (see Figure 6.14) because the grain size in both zones is too small (between  $0.7\ \mu\text{m}$  and  $4.7\ \mu\text{m}$ , see Table 6.7). However, a V-shaped boundary between the MTMAZ-1 and MTMAZ-2 is proposed since it is believed that such a boundary might have developed due to the radial speed of the rivet during the FricRiveting process. The radial speed is zero at the central (rotational) axis of the rivet, and increases from the centre outward to the circumference. Thus the frictional heat generated also increases in this manner, resulting in an increase in the volume affected by the process. Similar observations have been reported for friction-based joining processes. Suhuddin *et al.* [98] observed a V-shaped boundary between the BM and the TMAZ in the aluminum alloy 6082-T6 rod after friction surfacing on an aluminum alloy 2024-T351 substrate. Since both processes are similar, in that the consumable material or the rod (or rivet) is rotated at high speed under pressure, rubbing the substrate surface and producing frictional heating at the contact surface between the rod end

(or rivet tip) and the substrate surface, a similar V-shaped boundary line was also assumed to develop during FricRiveting. For more detailed information about the shape of the MTMAZ-1 / MTMAZ-2 boundary, a large EBSD scan covering the whole boundary region of both zones would be required. This analysis was outside the scope of the present work and presents a topic for future work.

#### 6.6.4. Simplified material flow model for PEEK composite

As mentioned earlier, although the tip of the rivet was severely deformed and was exposed to high temperatures, the polymer at the interface was not altered to any great extent. However, the composite material in contact with the rotating rivet was thermally degraded, as evidenced by an increased porosity ratio. To better understand this, it was important to study the material flow of the composite during the FricRiveting process.

The frictional heat generated by the tip of the rotating rivet interacting with the composite material softens the matrix of the composite; the drag (centrifugal) force generated by the rotation combined with the applied axial force causes the softened material to flow around the rivet. As the rotating rivet penetrates the composite substrate, its tip deforms until it assumes the desired mushroom-like shape. The penetration also causes the softened composite to flow toward the substrate surface. The fibres in the composite matrix are reorientated and, due to their very high aspect ratio, are aligned parallel to the material flow. The extent of material flow and fibre reorientation depends on the distance from the rotating rivet. From this overview, the material flow with respect to fibre reorientation is summarised in Figure 6.30; the blue-coloured fibres are in the CSZ and the red-coloured fibres are in the CTMAZ.

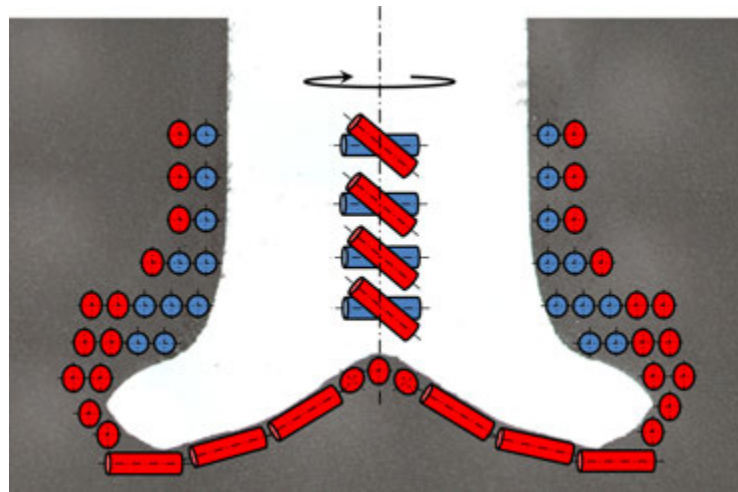


**Figure 6.30.** Material flow during FricRiveting. Blue fibres indicate material flow in the CSZ; red fibres indicate flow in the CTMAZ

### 6.6.5. Process-related thermomechanical degradation of the composite

Thermogravimetric analysis (TGA) was used to assess the thermal stability of PEEK reinforced with 30% short carbon fibres and the process-related changes in the softened composite volume in the joints. TGA evaluates changes in the weight of a known amount of a material, monitored as a function of temperature (or time). In this way, TGA can offer quantitative information, resulting from any reaction or thermal transition causing detectable changes in the weight during a controlled heating ramp. The measurement arrangement and procedure used to perform the TGA is described in detail in Section 4.7.1. Figure 6.31 shows the thermogram with the TG curve and the DTG curve for the PEEK composite base material. The TG curve shows the thermal decomposition behaviour of the material, indicating the loss of weight as a percentage of the original weight. The DTG curve represents the first derivative of the TG curve with respect to time, in this case the decomposition rate in terms of weight loss per minute. The temperature at the peak of the DTG curve is therefore the temperature at which the maximum rate of weight loss occurs ((dm/dt)<sub>max</sub>).

Zhang *et al.* [91] showed that the mass of unreinforced PEEK does not significantly change until a temperature of 534 °C is reached, and that the reaction rate is fastest at 548 °C. Meenan *et al.* [92] observed little or no change in the mass of their PEEK specimen until a temperature of about 552 °C. Immediately above this temperature they also observed a rapid decrease in mass. By 700 °C the mass was decreased by 50%. The TG curve in Figure 6.31 shows that the onset of the decomposition ( $T_{Onset}$ ) occurs at 586 °C. Below this temperature, the material seems to be stable and no significant mass loss is observed. The figure also shows that the decomposition is a two-step process. The first step is centred at 603 °C ( $T_{Peak}$ ), which means that the maximum reaction rate of -16.6 %/min is at that temperature. The decomposition in this first step is a result of random chain scission of the ether and ketone bonds of the polymer chain [63, 92, 99, 100] as described in Figure 6.32, showing the locations of the chain scission. The main products of the PEEK decomposition are CO, CO<sub>2</sub>, phenols and some aromatic ethers [63]. The first decomposition step ends at 619 °C ( $T_{End}$ ), at which point the second decomposition step begins (Figure 6.31). The thermal decomposition in this second step is attributed to the breaking and dehydrogenation of the cross-linked residue produced during the first step of decomposition, and leads to a thermally stable carbonaceous char [63, 100]. In the first stage of decomposition, there is a rapid and significant mass loss. The mass decreases by 20.5%, within a 33 °C window. The thermal decomposition in the second stage is much slower. Between 619 °C and the end temperature of 800 °C, the mass is reduced by only 8.7% of the initial mass. The residual mass at 800 °C is 65.6%. Similar results have been reported in the literature. Patel *et al.* [63, 100] reported the onset temperature of the first decomposition step as being about 565 °C for PEEK reinforced with 30% short carbon fibres, and that 30% of the mass was lost in a 30 °C window. In the second step they observed a mass loss of 10% up to

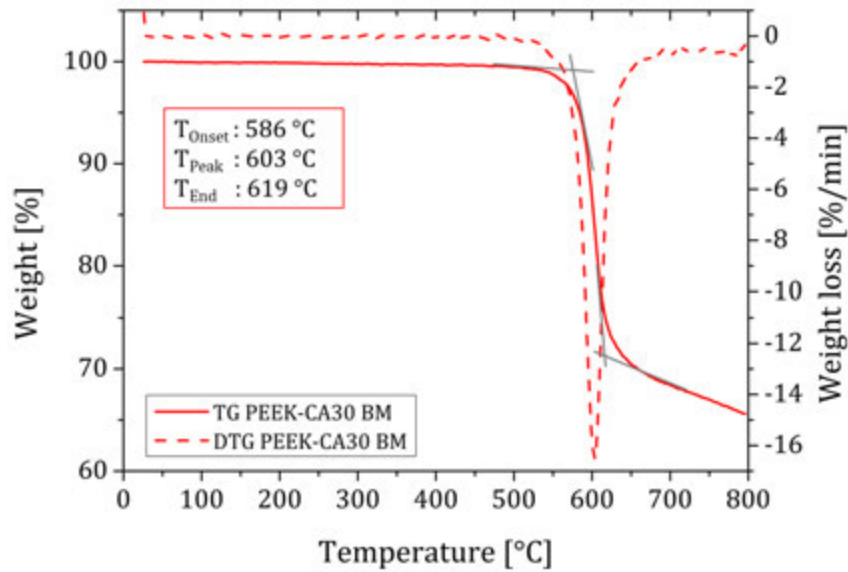


**Figure 6.31.** Thermogravimetric analysis thermogram of short carbon fibre-reinforced PEEK BM

900 °C. They also reported that a mass loss of 21% in the first decomposition stage was related to chain scission and the release of the ether and ketone groups, which is in good agreement with the findings in the course of this investigation (20.5% of mass loss in the first thermal decomposition step).

Since the onset of thermal decomposition was identified at 586 °C for the PEEK composite base material, and the peak temperature measured was  $460 \pm 20$  °C (Table 6.6, Section 6.6.1), the changes in the TG- and DTG curves for the flash material extracted from the friction-riveted joints was expected to be small.

The curves of the decomposition (TG curves) and the decomposition rate (DTG curves) for both the flash material and the BM were plotted together in Figure 6.33 for comparison. The figure shows that the decomposition behaviour of the BM and the flash material were very similar, supporting the assumption that the FricRiveting process only has a minor effect on the composite in the joining area. The TG curve of the flash material shows two steps of decomposition. The onset of the first decomposition step was shifted to the slightly lower temperature of 574 °C). The temperature at the peak of the DTG curve was also shifted to the lower temperature

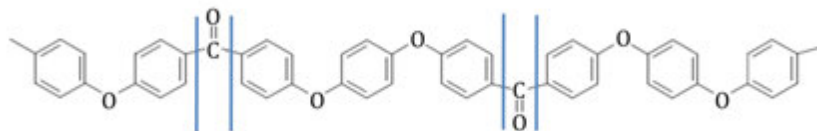


**Figure 6.32.** Chain scission of PEEK, adapted from [63]

of 593 °C, displaying a decomposition rate of -13.6 %/min. The end temperature of the first decomposition stage was decreased to 612 °C, leading to a mass loss of only 18.5% in the first step. The second decomposition step was much slower, with the mass decreasing by only 9.5% in the 188 °C window from 612 °C to 800 °C. The residual mass of the flash material (68%) was slightly higher than for the BM (66%).

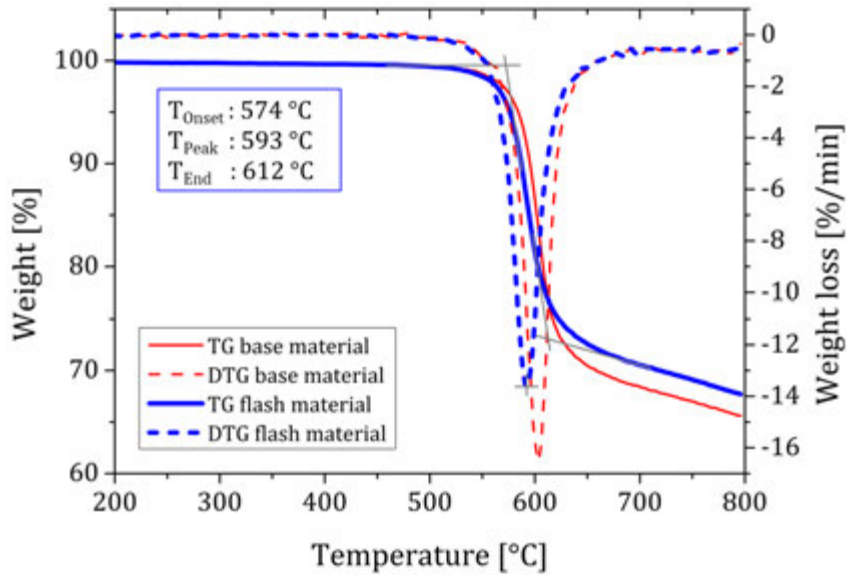


**Figure 6.33.** Comparison of the decomposition behaviour of the PEEK 30C BM (in red) and the flash material (in blue)

If there are no significant differences in the results compared to those for the base material, it can be assumed that the FricRiveting process has only a minor thermomechanical effect on the PEEK composite. Lower onset and peak temperatures indicate an overall decrease in the pyrolytic (thermal decomposition) stability [91]. However, the very small decrease (approx. 2.0%) for the FricRiveting specimen ( $T_{Onset} = 574\text{ °C}$ ) compared to the base material ( $T_{Onset} = 586\text{ °C}$ ) suggests that thermomechanical degradation for the analysed joint was limited. The results indicate that the FricRiveting process did not significantly affect the composite in the vicinity of the rotating titanium rivet. These findings are explained by considering the results of the temperature measurements discussed in Section 6.6.1 and the high thermal stability of the PEEK matrix material. The highest temperature measured for the selected joining configuration was 480 °C, which is far below the onset temperature for the first decomposition step (586 °C) identified for the base material.



## 6.7. Summary and conclusions

DoE was used to investigate the impact of four process parameters (RS, FT, FP and FoP) on the joint formation and joint performance. The joint formation was studied in terms of the mushrooming efficiency, the rivet penetration depth and the mechanical energy input. The tensile pull-out force was chosen to describe the mechanical performance of the investigated metallic-insert joints. Titanium grade 3 and short carbon fibre-reinforced PEEK were used to manufacture the friction-riveted metallic-insert joints in this study. To acquire the dimensions of the anchored rivet inside the reinforced polymer, the joints manufactured according to the DoE test matrix were X-ray scanned before the tensile pull-out test was conducted, enabling the correlation between the dimensions of the deformed rivet and the mechanical performance of the joint to be analysed. The results obtained within the framework of this investigation led to the following conclusions.

- The feasibility of FricRiveting was proved for the challenging material combination of short carbon fibre-reinforced PEEK and grade 3 titanium.
- Improvement to the FricRiveting RSM 400 system by incorporating a differential pressure sensor allowed the calibration of high FP levels. This resulted in a significantly decreased maximum standard deviation. This improvement enabled the impact of the process parameters on the joint formation and the joint mechanical performance to be assessed.
- The analysis of the DoE model can be used to identify optimized process parameter sets for diverse joint requirements. Therefore, for this material combination and for the investigated parameter range, joint formation and performance can be tailored to the specific needs of the intended application. To obtain shallower rivet penetration depths or lower mechanical energy input (e.g., to avoid possible thermal degradation of polymer matrix), the RS, FT and FP must be set to a low value (Figure 6.3 a, b, c and Figure 6.4 a, b, c). FoP (Figure 6.3 d and Figure 6.4 d) has a lower impact on these responses, and therefore should not be varied for this purpose. To increase the mushrooming efficiency and the pull-out force, the RS, FT and FoP must be set to high levels (Figure 6.2 a, b, d and Figure 6.5 a, b, d), and the FP should be set at an intermediate level (0.8 MPa); see Figure 6.2 c and Figure 6.5 c.
- An optimized parameter set that improves pull-out performance was developed using ANOVA statistical techniques. For this parameter set, the RS, FT and FoP need to be set to their highest levels (RS: 20000 rpm, FT: 1.5 s, FoP: 1 MPa), while the FP must remain at its intermediate level (FP: 0.8 MPa).
- The regression equations given in Equations 6.2 to 6.5 were used to predict the mushrooming efficiency, the rivet penetration depth, the mechanical energy input as a function of the four process parameters RS, FT, FP and FoP and their second-order interactions. These equations predicted the mechanical energy input with an accuracy between 80.7% and 96.1%.

- Increasing RS, FT and FoP (Figure 6.2) increased the total mechanical energy input, providing more energy for the plastic deformation of the rivet and widening of the rivet tip (increased mushrooming efficiency). The FP produced the highest mushrooming efficiency at its intermediate level (0.8 MPa). The additional energy input over and above this level did not contribute to further plastic deformation of the titanium rivet. Widening the rivet tip by 70% seems to be the upper limit for the deformability of the titanium.
- When RS, FT and FP were increased, the energy input also increased (Figure 6.4). At higher RS, the internal shearing was larger, resulting in a higher viscous dissipation (viscous heating) and an increasing energy input. Greater FT means longer joining times, increasing the total energy input. The FP had a less pronounced effect on the energy input because the normal forces can be neglected when determining the energy input (Figure 6.1). By contrast, the energy input showed only minor changes with increased FoP. The forging step contributed almost no additional mechanical energy input; rotation of the rivet stopped shortly after the forging step began, with the result that virtually no heat was produced during the forging step.
- The pull-out force represents the tensile strength of the joint. It presented a trend similar to the main effects plots for mushrooming efficiency, indicating a correlation between the geometry of the deformed rivet tip and the mechanical performance of the metallic-insert joints. Higher RS, FT and FoP produced higher pull-out force (Figure 6.5). This trend was associated with an increase in the mechanical energy input, resulting in a greater widening of the rivet tip. The wider the rivet tip is, the larger is the volume of polymer above the deformed tip, increasing the rivet anchoring.
- A mushrooming efficiency of 70% led to the maximum mechanical performance of the metallic-insert joint. At this threshold, the failure mode changed from failure mode III (“pull-out of rivet”) to failure mode I (“rivet failure”). Joints which failed by fracturing of the titanium rivet gave values similar to the ultimate tensile strength of titanium base material, achieving values of 10.6 kN. Therefore, the strength of these joints could only be further improved by using a higher tensile strength rivet material.
- The analysis of the process temperature and energy input allowed their relationship to be identified. Higher energy input produced higher process temperatures. The average peak temperature of the configuration with the highest energy input was 478 °C, which is less than 30% of the melting point of the grade3 titanium rivet but sufficient to plasticise the rivet tip inside the composite substrate.
- The microstructure of FricRiveted joints was significantly affected by the high heating and deformation rates related to the FricRiveting process. The influence of the process on the titanium rivet and on the composite substrate were investigated using the optimised FricRiveted metallic-insert joint made of PEEK reinforced with 30% short carbon fibres and grade3 titanium. The

microstructural characterisation of the joining region led to the identification of seven microstructural zones in the metallic and in the composite part of the joint; in the composite part are the composite base material (CBM), the composite heat-affected zone (CHAZ), the composite thermomechanically affected zone (CTMAZ) and the composite stir zone (CSZ); in the metal part are the metal thermomechanically affected zone 1 (MTMAZ-1), the metal thermomechanically affected zone (MTMAZ-2) and the metal friction zone (MFZ).

- A simplified model representing the material flow was introduced, developed by taking account of the observed levels of reorientation of the short carbon fibres during the process, as shown in Figure 6.30.
- A thermal analysis was performed by comparing the flash material produced during the process to the PEEK composite base material. The results indicated that FricRiveting did not significantly affect the composite in the vicinity of the rotating titanium rivet. These findings are explained in terms of the results of the temperature measurements discussed in Section 6.6.1. The highest average temperature measured for the selected joining configuration was 478 °C, which is far below the onset temperature of the first decomposition step identified using TGA (586 °C).

## 7. Determination of key design parameters for friction-riveted joints

In this chapter, the findings and research accomplished so far with the RSM 400 FricRiveting system will be transferred to the new RNA system. In order to do so, the main microstructural characteristics, the pull-out tensile properties as well as the superposition of the process monitoring curves for the optimised set of process parameters, obtained for PEEK-CA30/grade 3 Ti metallic-insert joints, need to be reproduced. Following that, the application of the FricRiveting process to woven fabric-reinforced PEEK laminates will be investigated by adjusting the optimised process parameter set for the new material combination. Finally, the key design parameters for friction-riveted single-lap shear joints will be evaluated and the mechanical performance of these friction-riveted joints will be compared to state-of-the-art mechanically fastened joints.

### 7.1. Comparison of PEEK-CA30/Ti joints produced using the RSM and RNA systems

The FricRiveted metallic-insert joints and the lap shear specimens made of fabric-reinforced PEEK and grade 3 titanium were joined using the new RNA FricRiveting system (Figure 4.6, Section 4.2), which was commissioned and constructed in the course of this work. As previously discussed, this new machine was designed to join thin composite/high-strength alloy multi-material structures. The RNA system was equipped with force and position sensors to allow precise control of the rivet penetration and deformation, a fundamental feature for avoiding mechanical damage of thin structures that was not available in the RSM 400 system. Considering this, and the future application of FricRiveting in thin carbon fibre-reinforced composite structures, a study of the key design parameters was carried out in the RNA system. In order to benefit from the research and the findings accomplished so far with the RSM 400 FricRiveting equipment (Figure 4.5, Section 4.2), it was necessary to ensure the transferability of the optimised process parameter set obtained using the RSM 400 system (for PEEK-CA30/grade 3 Ti metallic-insert joints) to the new RNA FricRiveting system prior to investigating the joinability of composite laminate/Ti single-lap shear joints. The transferability from one system to the other was demonstrated by reproducing the main microstructural characteristics and ten-

sile pull-out properties, and by superposition of the process monitoring parameter curves.

The specimens were joined using the optimised parameter set identified in Section 6.2 (RS: 20000 rpm, FT: 1.5 s, FoP: 1 MPa and FP: 0.8 MPa). Three key prerequisites were identified to demonstrate the transferability of the results:

- Monitoring of the process parameters RS, FT, FoT, FP, FoP and torque during joining
- Geometry of the rivet anchoring zone (the dimensions and shape of the mushroom-shaped anchoring feature of the titanium rivet), which was studied by X-ray scanning
- Quasi-static mechanical performance by pull-out tensile testing of the metallic insert joints.

In the case of the RSM400 system it was necessary to distinguish between the nominal process parameters and the actual process parameters, because the nominal parameter for rotational speed did not correspond to the actual process parameter. The nominal parameter for rotational speed was 20000 rpm but the actual value was 19000 rpm. The nominal process parameters for FT and FoT were identical to the actual parameters. In the RSM400 system, the FP and FoP were set in bars (1 bar = 1 MPa), and were transformed here into force values to facilitate the setting-up in the RNA system, where the FP and FoP parameters were set directly as forces. An overview of the nominal and actual process parameters for both systems is given in Table 7.1.

**Table 7.1.** Optimised process parameter set used in the study of the transferability from the RSM400 system to the RNA system, distinguishing between nominal parameters and actual parameters

	RSM 400		RNA	
	Nominal param	Actual param	Nominal param	Actual param
RS	20000 rpm	19000 rpm	19000 rpm	19000 rpm
FT	1.5 s	1.5 s	1.5 s	1.5 s
FP/FF	0.8 MPa	4.6 kN	4.6 kN	4.6 kN
FoP/FoF	1 MPa	5.8 kN	5.8 kN	5.8 kN
FoT	10 s	10 s	10 s	10 s

### 7.1.1. Monitoring process parameters and torque

The evolution of torque, rotational speed and force in the  $z$ -direction over time for both systems is shown in Figure 7.1. The curves from both machines demonstrated reasonably good matching of the process parameters and torque. The small deviations between the process monitoring curves were basically related to the hardware

type. The analysis of the influence of the differences in the hardware on the monitoring curves is outside the scope of this work. The basic differences of both systems were discussed in Section 4.2 and further information can be found in Appendix F.

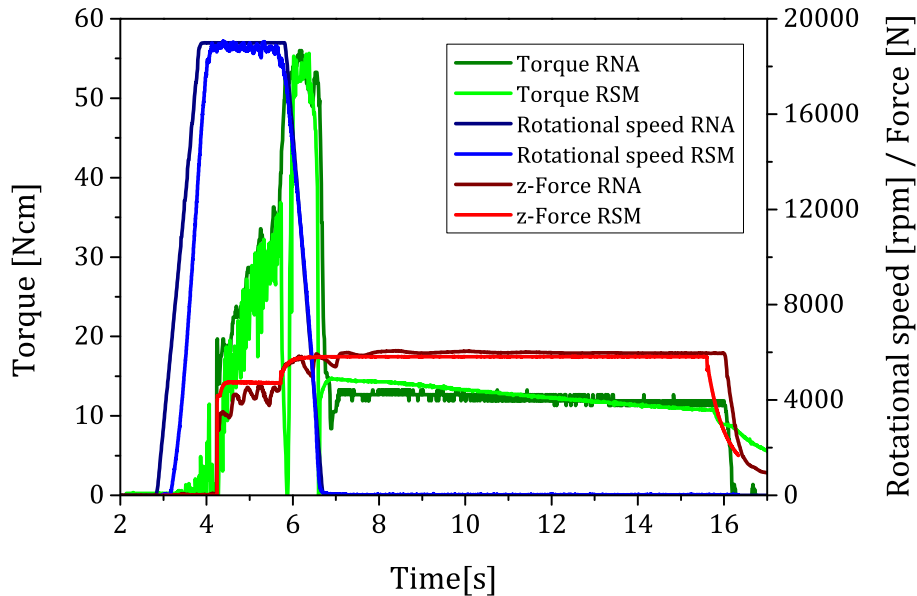


**Figure 7.1.** Comparison of the process parameter evolution over time for the RNA system (dark colours) and the RSM system (bright colours)

The results from figure 7.1, indicated the first pre-requisite for transferability, the comparability in "monitoring of the process parameters and torque", has been fulfilled.

### 7.1.2. Geometry of the rivet anchoring zone

In this section, joints produced by the two systems were assessed by comparing the geometry and the dimensions of the rivet anchoring zone. Since there were only minor differences in rotational speed, the axial force and the torque were observed. No significant changes were expected in the joint formation regime or mechanical performance of the joint. X-ray scans of the metallic-insert joints were taken to assess the shape of the anchoring feature and to measure its dimensions, using the procedure described in Section 4.5; examples for joints produced by both systems are shown in Figure 7.2. The scans showed similar geometries and shape for the RSM 400 (Figure 7.2 a) and the RNA system (Figure 7.2 b).

Penetration depth ( $T$ ) and widening of the rivet tip ( $w$ ) were measured for quantitative assessment and comparison of the dimensions of the anchoring features. The dimensions of the anchoring features of the joints produced by both systems are

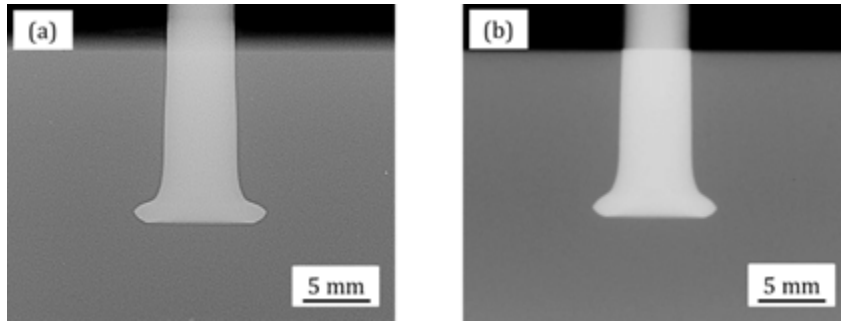


**Figure 7.2.** X-ray scans of FricRiveted metallic-insert joints produced by (a) RSM 400 system, and (b) RNA system

given in Table 7.2. The average values of ( $T$ ) and ( $w$ ) for both systems were comparable, with mean values in the range of the standard deviation. It was observed that the RNA system gave a smaller standard deviation for  $T$ , which indicated better control of the rivet penetration, very important in the case of thin joining partners. The difference was attributed to the differences in the linear drive concepts of the two systems, and the fact that the RNA system operated with the closed-loop control system described in Appendix F.

**Table 7.2.** Comparison of the dimensions of the rivet anchoring zone and the pull-out force of the PEEK-CA30/grade 3 Ti metallic-insert joints produced by the RSM 400 and RNA systems

	RSM 400 system	RNA system
$T$ [mm]	$12.9 \pm 0.6$	$12.6 \pm 0.1$
$w$ [mm]	$9.5 \pm 0.0$	$9.4 \pm 0.1$
$F_{\text{pull-out}}$ [kN]	$10.6 \pm 0.1$	$10.5 \pm 0.0$

Negligible differences were observed in the shape and dimensions of the anchoring zone for both systems; therefore the process parameter settings did not significantly alter the joint formation regime. Hence, it could now be said that the second prerequisite for transferability – the compatibility in “geometry of the rivet anchoring zone” – was fulfilled.

### 7.1.3. Quasi-static mechanical performance

The compatibility of the joint performance was investigated by comparing the pull-out performance of the metallic-insert joints obtained from the two systems. It was assumed that the pull-out behaviour of the joints would be similar, since no significant difference in either the shape or the dimensions of the anchoring features had been observed.

Pull-out tensile testing was performed following the procedure described in Section 4.8.1. An example of the force–displacement curve obtained from the joints produced by both FricRiveting systems is shown in Figure 7.3. The graph shows no significant differences in the pull-out behaviour of the joints produced by the two systems. This observation was supported by the mean values of the ultimate tensile force given in Table 7.2.

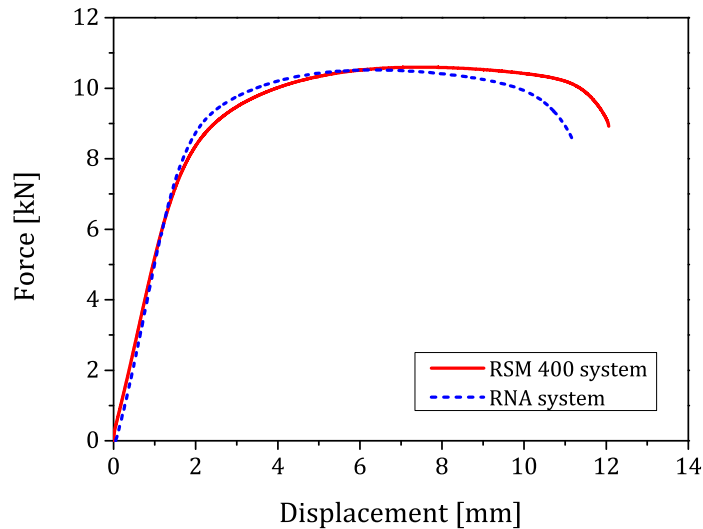


**Figure 7.3.** Force–displacement diagram comparing the pull-out performance of metallic-insert joints produced by the RSM 400 and RNA systems

In demonstrating the equality in “quasi-static mechanical performance”, the third prerequisite for transferability, it was concluded that the optimised parameters developed using the RSM 400 were proven to be transferable to the RNA system. Therefore, the RNA system was used to produce the single-lap shear joints made of woven fabric-reinforced PEEK and grade 3 titanium.

## 7.2. FricRiveting of fabric-reinforced PEEK/grade 3 Ti joints

In this section, the application of the FricRiveting process to woven fabric-reinforced PEEK and grade 3 titanium is addressed. The material properties and the dimensions of the fabric-reinforced PEEK substrate are shown in Section 4.1.4. For the metallic-insert joint configuration, two composite laminate plates were used to resemble a single-lap shear joint configuration.



### 7.2.1. Adjustment of the optimised process parameter set for composite PEEK laminates

Initially, the optimised process parameter set for PEEK-CA30/grade3 Ti (RS: 19000 rpm, FT: 1.5 s, FP: 4.6 kN, FoT: 10 s and FoP: 5.8 kN) was tested on woven fabric-reinforced PEEK composite laminates. The woven fabric-reinforced composite substrate differs on two ways from the short carbon fibre-reinforced PEEK composite used in the previous investigations: the type of reinforcement (from short carbon fibres to woven fabric reinforcement) and the fibre content (from PEEK-CA30 with 30 wt% to TPCL PEEK with 58 wt%). These differences led to changes in the material properties (see Tables 4.4 and 4.5) which had to be taken into account, requiring adjustments to the process parameters.

When the joining operation was carried out using the parameters obtained for PEEK-CA30, the rivet perforated both of the overlapping substrates and came in contact with the backing plate of the RNA system (see Figure 7.4). Considering that the combined thickness of the TPCL PEEK substrates was 8.68 mm and the average penetration depth in case of the PEEK-CA30/Ti grade 3 joints was 12.9 mm, the process parameter set needed to be adjusted to avoid completely piercing the substrates.

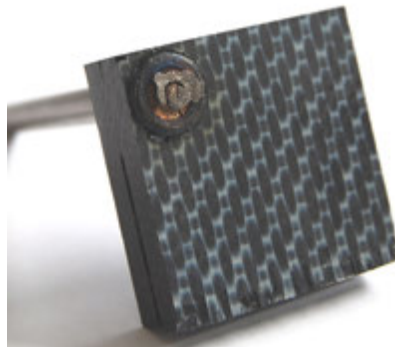


**Figure 7.4.** Preliminary evaluation of FricRiveting fabric-reinforced PEEK with grade 3 titanium using the optimised parameter set adopted for short carbon fibre-reinforced PEEK (RS: 19000 rpm, FT: 1.5 s, FP: 4.6 kN, FoT: 10 s and FoP: 5.8 kN)

The process parameter set needed to be modified for the thinner substrate. With the aim of achieving high rivet anchoring efficiency (high mushrooming efficiency), penetration for this material combination should be as deep as possible, but complete piercing of the substrate must be avoided. In Chapter 6 describing the process development, the influence of each process parameter on the penetration depth was analysed. These findings will now be used to modify the preliminary parameter set. The new substrate material contained different quantities and distribution of fibres, and was therefore expected to possess different frictional and rheological properties that would affect heat generation. Nevertheless, it was expected that the trends in

the relationships established earlier between the process parameters and joint properties were reasonably valid, considering that the same reinforcement materials – carbon fibre and polymeric matrix (PEEK) – were used. The friction time had been demonstrated to have the highest impact on the penetration depth (Figures 6.3 and 6.7b). A shorter friction time would therefore reduce the penetration depth. The statistical model (Equation 6.3 in Chapter 6) was used to determine the friction time needed for the required reduction in penetration depth. As a result, the friction time was reduced by one-third to 1 s in order to provide less heat input. The remaining process parameters remained unchanged, and three replicates were produced for microstructural characterisation. This configuration (i.e., RS: 19000 rpm, FT: 1 s, FP: 4.6 kN, FoT: 10 s and FoP: 5.8 kN) resulted in sound riveted joints, with no unusual occurrences such as the development of smoke or ashes being observed during the FricRiveting process. Visual inspection of the joints showed that the rivet did not pierce the substrate (see Figures 7.5 and 7.6). Initial observation showed that the reduced friction time resulted in a visible decrease in penetration depth, which indicated that the findings on the effect of the process parameters on joint formation could be used to tailor the dimensions of the anchoring feature in case of fabric-reinforced PEEK substrate.

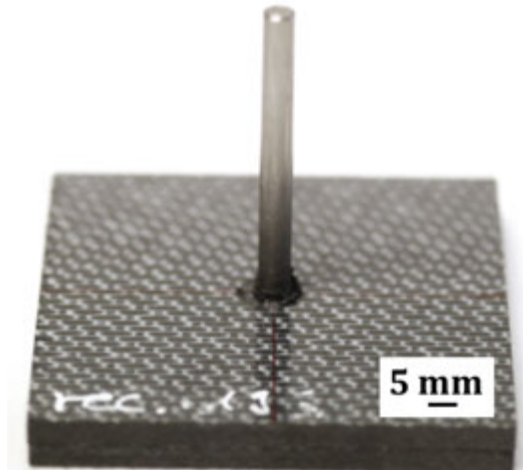


**Figure 7.5.** Metallic-insert joint for woven fabric-reinforced PEEK and grade 3 titanium, produced by two overlapping substrates and the adjusted set of parameters (RS: 19000 rpm, FT: 1 s, FP: 4.6 kN, FoT: 10 s and FoP: 5.8 kN)

The FricRiveted metallic-insert joints (overlap configuration) of composite PEEK laminates were X-rayed using the procedure described in Section 4.5. The X-ray radiographs for one of this joint is shown in Figure 7.6. The resulting measurements for penetration depth and the widening of the rivet tip are summarised in Table 7.3. The penetration depth was significantly reduced by decreasing the friction time to 1 s. The average penetration depth of  $7.5 \text{ mm} \pm 0.1 \text{ mm}$  was within the ideal range for this material combination. The average deformation width at the tip of the

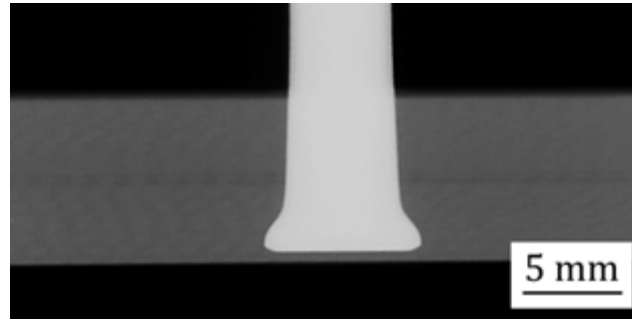


**Figure 7.6.** X-ray scan radiograph of the metallic-insert joint in Figure 7.5

metallic rivet was 7.8 mm, corresponding to a mushrooming efficiency of 56.8%. The deformation width of the rivet tip was significantly less than for the metallic-insert joints made of short carbon fibre-reinforced PEEK joined with the optimised process parameter configuration (91.4%, Chapter 6). Thus, not only the penetration depth was affected by the shorter friction time but also the deformation width of the rivet tip and thereby also the mushrooming efficiency. This behaviour is explained by examining Equation 2.2, in which a decrease in the friction time results in a decrease in the total mechanical energy input. Thus, less energy was available for the plastic deformation of the rivet tip, reducing the deformation width of metallic rivet tip. This is consistent with the findings in Chapter 6, where Figure 6.2 b shows that a decrease in friction time also leads to a lower mushrooming efficiency.

**Table 7.3.** Dimensions of the anchoring feature and the ultimate pull-out force of the FricRiveted metallic-insert joints made of fabric-reinforced PEEK and grade 3 titanium

$T$ [mm]	$w$ [mm]	$F_{\text{pull-out}}$ [kN]
$7.5 \pm 0.1$	$7.8 \pm 0.2$	$10.3 \pm 0.0$

In order to assess the quasi-static mechanical strength of these joints, the specimens were subjected to pull-out tests, following the same procedure adopted earlier. The test results in Table 7.3 show that the average pull-out force of the metallic-insert joints was 10.3 kN which is similar to the ultimate tensile strength of the base material, 10.6 kN. All three of the test specimens failed in failure mode I, “through the rivet” failure, as shown in Figure 7.7. Failure mode I is preferred, since failure occurs outside the joining region, requiring a force similar to the ultimate tensile strength of the base material [54].

Although the adjustment of the energy input by reducing the friction time led to a decreased mushrooming efficiency, the metallic-insert joints nevertheless showed the preferred failure behaviour under tensile loading, with failure taking place in the rivet base material. Thus the adjusted process parameter configuration (RS:

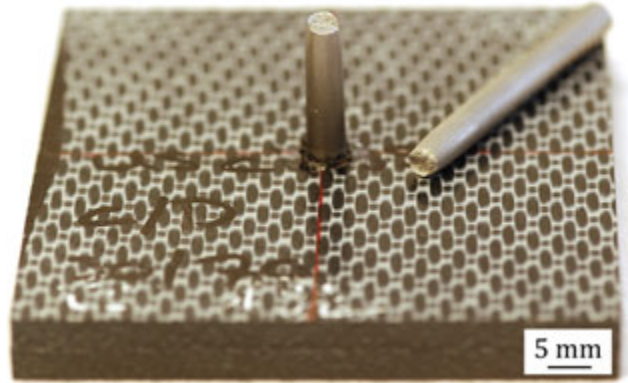


**Figure 7.7.** Example of the failure mode observed for friction-riveted woven fabric-reinforced PEEK/grade 3 titanium metallic-insert (overlap) joints

19000 rpm, FT: 1 s, FP: 4.6 kN, FoT: 10 s and FoP: 5.8 kN) is suitable for evaluating the key design parameters of friction-riveted composite-composite lap shear joints.

### 7.3. Evaluation of key design parameters

In this section, the design of a friction-riveted single lap shear composite-composite joints is discussed. In friction-riveted joints, the anchoring feature can be considered as a mechanical interlock, so the standard procedures for designing mechanically fastened composite joints were adopted for this purpose. For mechanically fastened joints, the selection of an optimal joint geometry and joint material are fundamental to the structural integrity and reliability of the composite structure [27]. The joint performance and the occurrence of a specific failure mode mainly depend on the joint geometry, the laminate configuration or lay-up [28]. The design parameters which must be considered when designing a joint in composite material are the fastener diameter ( $d$ ), the laminate thickness ( $t$ ), the edge distance ( $e$ ), the width of the joint ( $w$ ) and the clamping torque of the fastener [29].

The aim of this investigation was to design a friction-riveted joint capable of carrying large loads and which fails in a non-catastrophic (slowly progressing) failure mode. In this work, the material for both the metallic rivet and the composite substrate for the friction-riveted composite-composite joints were not changed, considering that this lay-up configuration and thickness were the same as those used in aircraft structures. The rivet diameter also remained unchanged, since it was the dimension usually adopted in state-of-the-art mechanical fastening of aircraft composite structures. Therefore in the design of the FricRiveted single-lap shear joints, three key design parameters were taken into account: edge distance, joint width and clamping torque of the rivet.

### 7.3.1. Influence of edge distance on joint mechanical performance

Single-bolt joints were used to investigate the effect of the edge distance on the mechanical performance. According to Hart-Smith [29], this simple joint configuration provides a logical starting point in the assessment of the effect of the key design parameters on the joint performance. Bearing testing of single-bolt joints was selected to analyse the effect of the edge distance and its relationship to specimen width, strength and failure mode of the joint.

The commonly observed failure modes of single-bolt joints were illustrated in Figure 2.1. Figure 2.1 a–c shows the basic failure modes, which are net-tension, shear-out and bearing failure. Tear-out and cleavage failure (Figure 2.1 d and e) are secondary failure modes that occur only after an initial bearing failure [27]. Only two of these failure modes, bearing failure and net-tension failure, are considered acceptable because of the high strength usually entailed – although bearing failure, with its slower crack propagation, is preferred for design purposes. The remaining failure modes at lower loads are considered to be premature failures [29]. Because bearing failure progresses more slowly, it allows damage to be detected before final failure; therefore, bearing failure was chosen as the preferred failure mode for the friction-riveted composite-composite joints. Net-tension, shear-out and cleavage failures all occur suddenly and are therefore considered as catastrophic failures [27, 31]. The distinction between bearing failure and net-tension failure depends mainly on the geometry of the joint, especially the width-to-diameter ratio ( $w/d$ ) [29]. Greater  $w/d$  and sufficient edge distance causes the failure mode to change from net-tension or shear-out failure to bearing failure [31]. When the edge distance is too small, the joint fails in shear-out or cleavage mode.

The bearing specimens were produced and tested as described in Section 4.8.2. The edge distance and width of the specimens were each varied to assess their effect on the mechanical performance and failure mode. Two edge distances ( $e = 10$  mm and 15 mm) were each tested for five different specimen widths ( $w = 15$  mm, 20 mm, 25 mm, 30 mm, 35 mm). The dimensions of the specimens are given in Table 7.4. Three replicas were produced for each of the configurations shown in Table 7.4.

The applied forces and resulting deformations were monitored during testing. In the next step the bearing stress ( $\sigma_i^{br}$ ) and the bearing strain ( $\epsilon_i^{br}$ ) were calculated from Equations 7.1 and 7.2 respectively, where  $P_i$  is the force at the  $i$ -th data point;  $d$  is the diameter of the rivet;  $t$  is the thickness of the composite material;  $\delta_i$  is the extensometer displacement at the  $i$ -th data point; and  $k$  is the force per hole factor ( $= 1.0$  for the single-fastener test) [32]. Then, the stress–strain curves were plotted and the ultimate bearing strength ( $F^{bru}$ ) was determined from the maximum force carried by the specimen prior to the end of the test, using equation 7.3 [32]. The failure modes for all of the specimens were then analysed.

**Table 7.4.** Dimensions of bearing-test specimens;  $t$  is the thickness of the composite material,  $w$  is the width of the specimen,  $L$  is the length of the specimen,  $e$  is the edge distance, and  $d$  is the rivet diameter

$t$ [mm]	$w$ [mm]	$L$ [mm]	$e$ [mm]	$d$ [mm]
4.3	15 ( $3d$ )	100	10 ( $2d$ )	5
4.3	20 ( $4d$ )	100	10 ( $2d$ )	5
4.3	25 ( $5d$ )	100	10 ( $2d$ )	5
4.3	30 ( $6d$ )	100	10 ( $2d$ )	5
4.3	35 ( $7d$ )	100	10 ( $2d$ )	5
4.3	15 ( $3d$ )	100	15 ( $3d$ )	5
4.3	20 ( $4d$ )	100	15 ( $3d$ )	5
4.3	25 ( $5d$ )	100	15 ( $3d$ )	5
4.3	30 ( $6d$ )	100	15 ( $3d$ )	5
4.3	35 ( $7d$ )	100	15 ( $3d$ )	5

$$[h]\sigma_i^{\text{br}} = \frac{P_i}{dtk} \quad (7.1)$$

$$[h]\epsilon_i^{\text{br}} = \frac{\delta_i}{d} \quad (7.2)$$

$$[h]F^{\text{bru}} = \frac{P_{\text{max}}}{dtk} \quad (7.3)$$

The average ultimate bearing strengths for all the test configurations are shown in Figure 7.8 in which is seen that, for all  $w/d$ , an edge distance of  $3d$  led to a higher ultimate bearing strength than edge distance of  $2d$ . This is in agreement with the findings presented by Cooper *et al.* [31] who showed that the edge distance-to-diameter ratio ( $e/d$ ) was almost directly proportional to the failure load. From Figure 7.8, increasing  $w/d$  from 3 to 4 gave a significant increase of the average ultimate bearing strength, from 644.3 MPa to 812.1 MPa for  $e = 3d$ . For  $w/d > 4$  no further increase of the ultimate bearing strength was observed, which indicated that the failure mode changed between a  $w/d$  of 3 and 4. This is supported by the observations made in [31], where they reported that the failure loads in glass fibre-reinforced polyester were almost proportional to the  $w/d$  ratio until the failure mode changed from net-tension to bearing. They also noted that any further increase in  $w/d$  resulted in a decreased load at failure. This behaviour had also been observed by Hart-Smith [29], who reported that the maximum strength was observed in the transition region between bearing failure and net-tension failure.

The average ultimate bearing strength and the corresponding failure mode for each of the investigated specimen geometries are shown in Table 7.5. Examples of the fracture surfaces of these bearing specimens can be found in Appendix G. The ultimate bearing strength varied between 620.3 MPa and 718.4 MPa and the standard deviation was less than 6% in all configurations. The table also shows that the failure mode changed with increasing  $w/d$  ratio from net-tension failure at  $w/d = 3$  to cleavage failure for  $w/d > 3$  and then to shear-out failure for  $w/d > 5$ . These failures occurred suddenly and were therefore considered catastrophic [27, 31]. Net-tension failure is associated with failure of the fibre and matrix due to tensile stress concentrations at the edge of the through-hole. It has been found that this type of failure normally occurs when  $w/d$  is too small [27]. Failure by cleavage and shear-out typically occur when the edge distance is too small [29]. Cleavage failure is initiated by longitudinal splitting of the loaded side of the through-hole, causing high stress concentrations at the hole in the longitudinal direction, and leading to failure across the net section of the specimen [31]. Shear-out failure is associated with the shear and compressive failure of the composite fibres and matrix [27]. These results suggested that the preferred bearing failure was not achieved for an edge distance of  $2d$  and the  $w/d$  ratios investigated here.

For an edge distance of  $3d$ , the ultimate bearing strength varied between 644.3 MPa and 824.8 MPa and the standard deviation was below 8% for all configurations. The

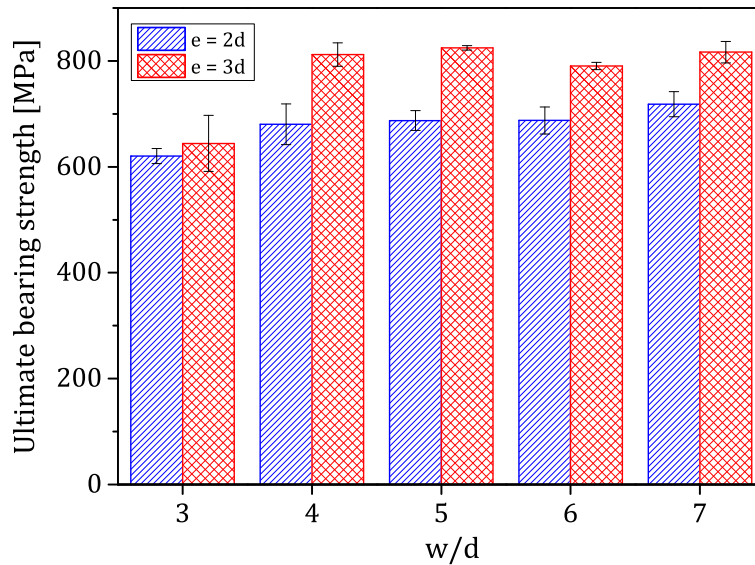


**Figure 7.8.** Average ultimate bearing strength variation with edge distance and specimen width

failure mode changed with increasing  $w/d$  from net-tension failure at  $w/d = 3$  to bearing failure for  $w/d > 3$ . This behaviour agrees with the findings of Cooper *et al.* [31] and Kelly *et al.* [101], who reported that the failure mode changed from net-tension to bearing when the edge distance was sufficiently large and  $w/d$  was increased. This also supported the observations previously discussed, that the increase of the ultimate bearing strength was associated with a change in failure mode, as also reported in [31]. Bearing failure mainly occurs as a result of shear and compression failures of the matrix and the fibres [27]. It was shown that for  $w/d > 3$  and an edge distance of  $3d$ , the preferred bearing failure was achieved. Therefore the edge distance of  $3d$  will be applied in the fabrication of friction-riveted composite-composite lap shear joints.

### 7.3.2. Influence of rivet clamping torque on joint mechanical performance

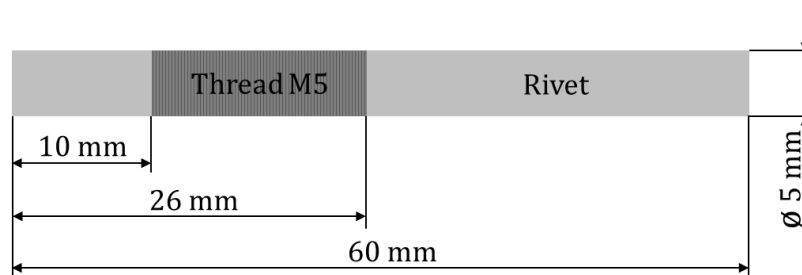
In this section, the clamping torque suitable for friction-riveted composite single-lap shear joints is defined. In order to do this, a threaded rivet geometry, which allows a washer and nut to be attached for load transfer, first needed to be chosen. A thread was cut along the section of the rivet that would be exposed to the surface of the composite substrates; the length of the threaded section was kept to a minimum so that its reduced diameter would not cause the rivet to buckle during the joining



**Table 7.5.** Average ultimate bearing strength ( $F^{bru}$ ) and corresponding failure mode related to specimen geometry

$e$	$w$	$F^{bru}$ [MPa]	Failure mode
$2d$	$3d$	$620.3 \pm 14.3$	Net-tension
$2d$	$4d$	$680.4 \pm 38.5$	Cleavage
$2d$	$5d$	$687.4 \pm 18.6$	Cleavage
$2d$	$6d$	$687.5 \pm 25.7$	Shear-out
$2d$	$7d$	$718.4 \pm 23.5$	Shear-out
$3d$	$3d$	$644.3 \pm 52.9$	Net-tension
$3d$	$4d$	$812.1 \pm 22.2$	Bearing
$3d$	$5d$	$824.8 \pm 4.4$	Bearing
$3d$	$6d$	$790.6 \pm 7.0$	Bearing
$3d$	$7d$	$816.6 \pm 20.3$	Bearing

process. The geometry of the threaded rivet as a result of these considerations is shown in Figure 7.9.

**Figure 7.9.** Dimensions of the threaded rivet (M5) used to allow the friction-riveted lap shear joints to be clamped

The prepared rivets were used to produce five metallic-insert joints with the adapted process parameter set of RS: 19000 rpm, FT: 1 s, FP: 4.6 kN, FoT: 10 s and FoP: 5.8 kN, presented in Section 7.2.1. Then the unthreaded upper length of the rivet (10 mm) was removed and specimens are ready for testing. An example of a torque specimen is shown in Figure 4.15. Clamped test specimens were tested according to the procedure described in Section 4.8.3; the break-loose torque was determined by increasing the torque until the anchored rivet loosened inside the composite.

The anchored rivets in all the tested specimens loosened when a torque of 7 Nm was applied; that is, the break-loose torque for specimens produced using the adapted process parameter set and therefore the clamping torque to be used to tighten the nut and washer in the lap shear joints needed to be less than 7 Nm. Reports in the literature have shown that the clamping torque significantly affects the bearing strength of bolted composite joints. Cooper *et al.* [31] showed that increasing the bolt torque from zero to 3 Nm and 30 Nm, increased the bearing failure load by

45% and 80% respectively. A similar effect has been reported by Hart-Smith [29], who compared pinned joints with finger-tightened bolted joints and showed that the bearing strength was increased by 100%. Studies by Khashaba *et al.* [102] also showed that increasing the bolt clamping torque from 0 Nm to 5 Nm and then to 15 Nm resulted in an increased ultimate bearing strength.

This implies that higher clamping torque produces better joint performance. Therefore, the highest clamping torque possible, without loosening the anchored rivet inside the composite, was to be used for the friction-riveted lap shear joints. To ensure that the composite–metal interface at the joining zone would not be damaged during clamping of the joint, 5 Nm was chosen as the clamping torque for the friction-riveted lap shear joints.

### 7.3.3. Influence of specimen width on joint mechanical performance

The effect of the width or  $w/d$  on the mechanical performance and the failure mode were investigated in single-lap shear specimens. The joints were friction-riveted using the procedure described in Section 4.8.4 and the process parameter set developed in Section 7.2.1. The joints were then clamped by a nut and a washer with a clamping torque of 5 Nm. Three replicates were produced for each of the five  $w/d$  ratios studied ( $w = 15$  mm, 20 mm, 25 mm, 30 mm, 35 mm). A typical friction-riveted single-lap shear joint is shown in Figure 4.16 which presents an X-ray radiograph scan, a photograph and a sketch showing the relevant dimensions. The dimensions of the joints are given in Table 7.6.

**Table 7.6.** Dimensions of the friction-riveted single-lap shear specimens, where  $t$  is the thickness of the composite material,  $w$  is the width of the specimen,  $L$  is the length of the specimen,  $e$  is the edge distance and  $d$  the diameter of the rivet

$t$ [mm]	$w$ [mm]	$L$ [mm]	$e$ [mm]	$d$ [mm]
4.3	15 ( $3d$ )	155	15 ( $3d$ )	5
4.3	20 ( $4d$ )	155	15 ( $3d$ )	5
4.3	25 ( $5d$ )	155	15 ( $3d$ )	5
4.3	30 ( $6d$ )	155	15 ( $3d$ )	5
4.3	35 ( $7d$ )	155	15 ( $3d$ )	5

Single-lap shear joints were tested following the procedure in Section 4.8.4 and using the testing arrangement shown in Figure 4.17. The applied forces and the associated displacements were monitored during each test, and the failure modes were determined for all of the tested joints.

The average ultimate joint strengths for the  $w/d$  ratios in all test configurations are shown in Figure 7.10. The joint strength and the associated failure mode depending

on the  $w/d$  are shown in Table 7.7. The ultimate joint strength was calculated considering the failure mode. The joint strengths of specimens in net-tension failure were calculated from Equation 7.4 [34], where  $P$  is the ultimate tensile force,  $w$  is the width of the specimen and  $t$  is the thickness of the composite material. The joint strengths of specimens in bearing failure were calculated from Equation 7.3.

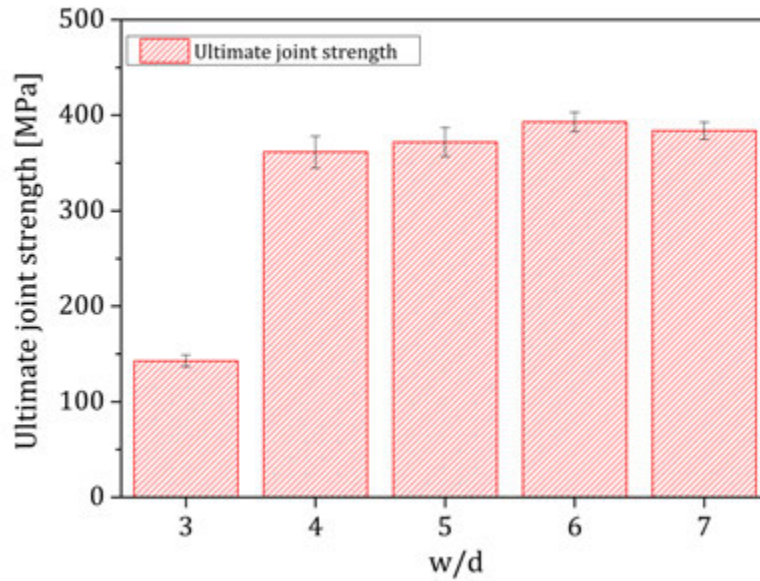


**Figure 7.10.** Influence of the  $w/d$  ratio on the average ultimate strength of friction-riveted woven fabric-reinforced composite joints produced with  $e = 3d$

**Table 7.7.** Average ultimate joint strengths and the corresponding failure modes associated with the  $w/d$  ratio, calculated using Equation 7.4 for specimens in net-tension failure, and from Equation 7.3 for specimens in bearing failure

Width	Joint strength [MPa]	Failure mode
$3d$	$142.7 \pm 9.2$	Net-tension
$4d$	$361.5 \pm 16.7$	Bearing/rivet failure
$5d$	$371.9 \pm 15.1$	Bearing/rivet failure
$6d$	$393.0 \pm 10.2$	Bearing/rivet failure
$7d$	$383.9 \pm 9.1$	Bearing/rivet failure

$$\sigma_{\text{net-ten}} = \frac{P}{(w-d)t} \quad (7.4)$$

It was shown that increasing the  $w/d$  ratio from 3 to 4 led to a 253% increase in ultimate joint strength, from 142.7 MPa to 361.5 MPa. This increase is explained by the change in failure mode from net-tension to bearing, as shown in Table 7.7. All specimens with  $w/d > 3$  experienced bearing failure as the initial failure mode, followed by rivet shear failure as the final failure mode. However, a further increase of  $w/d$  to 6 resulted in very small increases in the joint strength; when  $w/d > 6$  the joint strength decreased. These observations are in agreement with the results reported by Cooper *et al.* [31], who showed that the failure loads were nearly proportional to  $w/d$ , and the failure load at higher  $w/d$  ratios started to decrease and were less than the failure loads closer to the critical  $w/d$  ratio (i.e., the  $w/d$  ratio where the failure mode changed from net tension to bearing). They assumed that this decrease in joint strength was related to the increased clamping area at higher  $w/d$  ratios, which reduced the effective clamping pressure near the bolt and consequently reduced the failure load.

The best performance of the friction-riveted single-lap shear joints was observed for a  $w/d$  ratio of 6, which gave an average ultimate joint strength of 393.0 MPa. This design study identified an optimised friction-riveted single-lap shear joint, fulfilling the two requirements stated at the beginning: a strong friction-riveted single-lap shear joint that fails non-catastrophically. These requirements were met using an edge distance of  $3d$ , a clamping torque of 5 Nm and a joint width of  $6d$  for the evaluated combination of materials.

### 7.4. Failure mechanisms

In Section 7.3.3, two failure modes were identified for friction-riveted composite single-lap shear joints: net-tension and bearing combined with final failure in the rivet by shear. In this section a specimen failing in net-tension ( $w/d = 3$ ) and a specimen failing in bearing ( $w/d = 6$ ), representing the joint produced with the optimised joint key design parameters, were selected to investigate failure into more detail.

The force–displacement curves in Figure 7.11 show the differences in the load-carrying behaviour of the two single-lap shear joints. In both curves, three separate regions were identified. The force–displacement curve of the joint failing by net-tension showed a slight reduction in stiffness, indicated by a change in slope (decrease in Young’s modulus), from a linearly elastic force–displacement relationship in region (1) to region (2) [102] as a result of damage at the edge of the hole. Point (3) represents the maximum load prior to final failure of the joint in the lower composite plate, shown by a sudden drop in force. This behaviour supports the findings reported in the literature wherein the net-tension is a failure mode that occurs suddenly and is therefore considered to be a catastrophic failure [27, 31, 103].

In contrast to the specimen failing in net-tension, the force–displacement curve of the joint failing by bearing/rivet failure shows an initial linear relationship in region

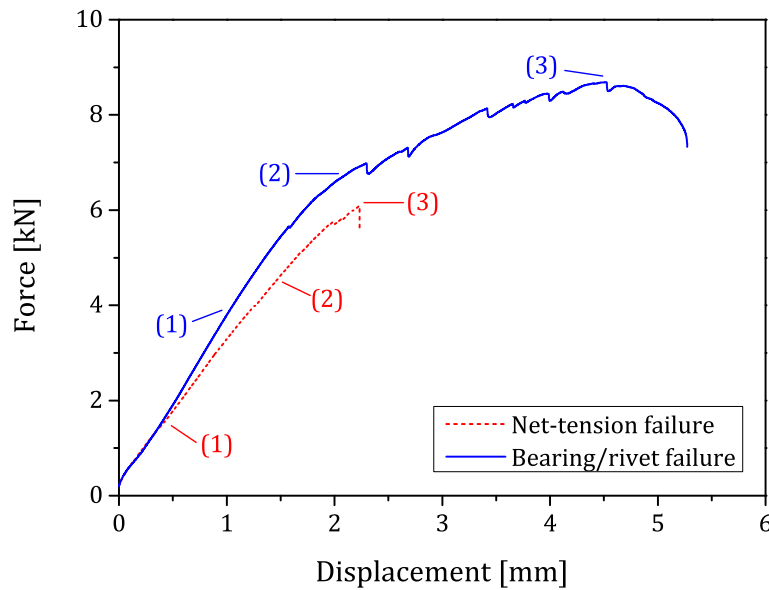


**Figure 7.11.** Comparison of the force–displacement curves of friction-riveted joints failing in net-tension and in a mixed bearing/rivet failure mode

(1) followed by a nonlinear relationship in region (2) with considerably reduced stiffness. This is an indication of progressive damage accumulating in the composite surrounding the rivet [101, 104]. Increasing the displacement further increased the strength of the joint until the maximum load was reached at point (3) [104]. The joint finally failed due to rivet shear failure at a much higher force when the load bearing capacity of the rivet material was exceeded. The average failure load of the net-tension joints ( $w/d$  ratio of 3) was  $6.2\text{ kN} \pm 0.4\text{ kN}$  and for the bearing/rivet failure joints ( $w/d$  ratio of 6)  $8.5\text{ kN} \pm 0.2\text{ kN}$ . Additionally, it can be seen that the displacement at failure in these two joint configurations was very different: for the net-tension joint, failure occurred at an average displacement of  $2.2\text{ mm} \pm 0.2\text{ mm}$ , whereas the bearing/rivet joint failed at  $4.2\text{ mm} \pm 0.3\text{ mm}$ , which indicates that the load was sustained for up to twice as long. The failure process of the bearing/rivet failure joints takes place with a much higher energy absorption than the net-tension joints, as represented by the area below the force–displacement curves [103]. The blips in the force–displacement curve of the bearing/rivet failure joint in region (2) (Figure 7.11) indicate progressive damage to the joint by fibre cracking or matrix crushing by the bearing interaction with the rivet; this phenomenon has also been acoustically detected during testing, which has also been reported by Hart-Smith [29].

Figure 7.12 shows an example of a tested friction-riveted single-lap shear joint that failed by net-tension; Figure 7.13 shows a specimen that failed by bearing/rivet shearing. In net-section failure the critical stress distribution around the hole loaded

by the rivet were the normal stresses at the net-section area of the specimen [104]; thus the fracture occurred across the net-section of the joint, perpendicular to the direction of the applied force, with the crack originating at the edge of the hole as shown in Figure 7.12 [101]. Unlike the more usual failure type where the final crack propagates through the whole thickness of the composite plate, the net-tension failure in these friction-riveted single-lap shear joints produced partial delamination in the lower composite plate. This is associated with the fact that the rivet did not pass completely through the plate as it does in bolted joints. Analytical description of the stress distribution in the friction-riveted joints is very complex and is outside the scope of this work. Basic theory on this subject can be found in [105]. The critical stresses in bearing/rivet shearing joints (Figure 7.13) are radial bearing stresses due to compression at the bearing plane [104]. As discussed, the distinction between net-tension and bearing failure depends mainly on the  $w/d$  ratio. The stresses rapidly decrease with distance from the edge of the hole at the net-section area when the  $w/d$  ratio is increased, and the maximum compressive stresses develop in the bearing area due to the interaction between the rivet and the hole [104]. Compressive stresses induce matrix cracking, fibre microbuckling and kinking, with significant delamination [104]. Further description of the micromechanisms of fracture are outside the scope of this study. More information on the types of fracture micromechanisms can be found in [105].

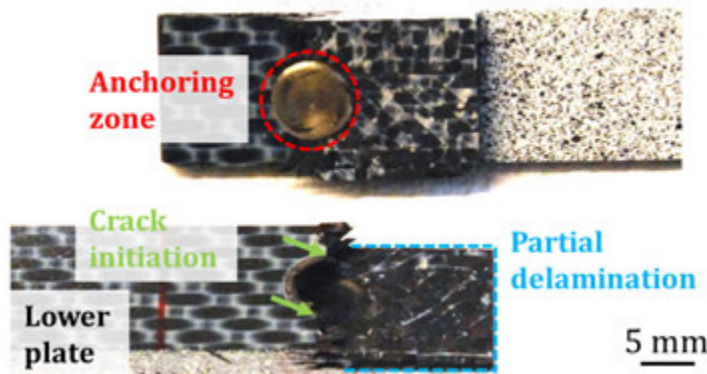


**Figure 7.12.** Example of a friction-riveted single-lap shear joint ( $w/d = 3$ ) failing by net-tension

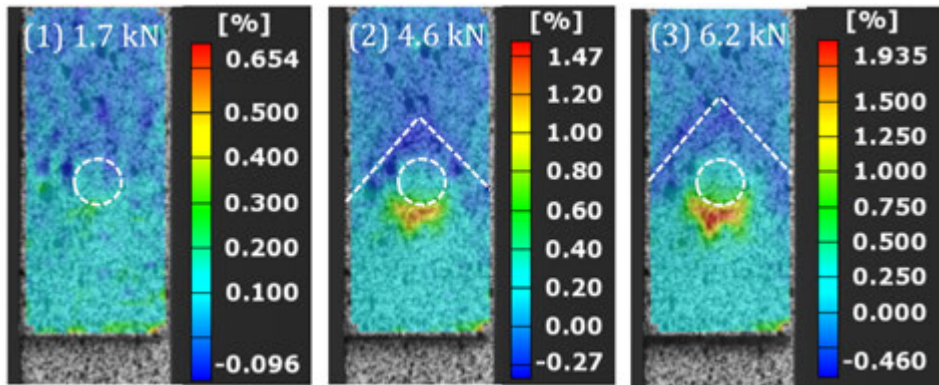
Graphical monitoring of the strain distribution by image correlation was used during lap shear testing to assess the differences in the failure evolution of the two failure modes. The preparation of the specimens and arrangement used in this analysis are shown in Section 4.8.4. For both failure modes, the evolution of the failure was evaluated at three different loading stages, related to regions 1, 2 and 3 described and indicated in Figure 7.11. Figure 7.14 shows the major strain distribution at three load stages for a net-tension joint; the final stage was recorded shortly before final failure. In stage 1 (1.7 kN) it can be seen that the strain in the lower



**Figure 7.13.** Example of a friction-riveted single-lap shear joint ( $w/d = 6$ ) failing by mixed bearing/rivet failure mode

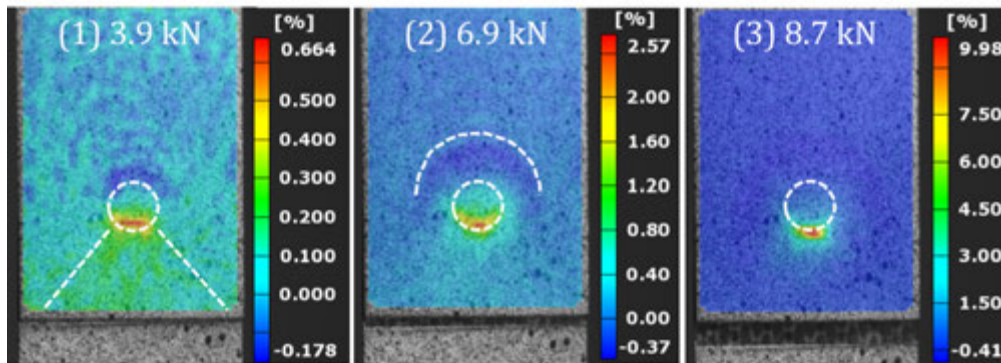
composite beneath the rivet (indicated by the white dashed circle) and close to the free edge, was about zero. Tensile strain then developed above the rivet close to the gripped edge due to the tensile force applied in the lap shear test. As the test progressed (4.6 kN), a compressive strain concentration developed below the rivet. Above the rivet, tensile strain developed along the  $\pm 45^\circ$  fibres of the surface ply of the composite material, shown by the white broken lines in Figure 7.14). These fibres carried the tensile load around the hole, since the  $0^\circ$  and  $90^\circ$  fibres had been severed during the insertion of the rivet. At stage 3 (6.2 kN), shortly before final failure, the compressive and the tensile strains increased. The strain concentration below the rivet broadened toward the width of the specimen perpendicular to the loading direction. The average tensile force carried by the  $\pm 45^\circ$  fibres around the hole increased from an average of 0.27% to an average of 0.46%, followed by failure of the joint in the net-tension failure mode.

Figure 7.15 shows the major strain distribution for the three loading stages indicated in Figure 7.11 for a bearing/rivet joint failure. In stage 1 (3.9 kN), the figure shows that a compressive strain field developed below the rivet, close to the free edge. This compressive field had the shape of a right-angled triangle (indicated in the figure by dashed lines) due to the compressive force carried by the  $\pm 45^\circ$  fibres. A zone of strain concentration was located directly at the interface between the deformed rivet tip and the composite, where the rivet was pressed against the boundary of the hole. A tensile strain field was located above the rivet, close to the gripped edge of the joint. At stage 2 (6.9 kN), the compressive and tensile strains increased as loading increased. An annular tensile strain concentration field is seen to have developed above the rivet (dashed semi-circle in Figure 7.15) due to the tensile force transferred by friction into the lower plate at the area of increased clamping pressure associated with the washer on the upper plate on the opposite side of the joint. In stage 3, shortly before shear failure of the rivet (8.74 kN), a compressive strain field was concentrated at the interface between the deformed rivet tip and the composite below the rivet. The tensile strain field above the rivet has now vanished because the



**Figure 7.14.** Major strain distribution during evolution of net-tension failure at three load levels, indicated in the force-displacement curve in Figure 7.11 for a specimen with  $w/d = 3$ . The white dashed circles show the location of the rivet; the broken lines indicate the direction of the tensile force carried by the  $\pm 45^\circ$  fibres

clamping pressure has decreased due to rotation and bending of the rivet, with the associated tendency toward physical separation of the upper and lower composite plates due to secondary bending (see Figure 7.15).



**Figure 7.15.** Major strain distribution during evolution of initial bearing failure followed by rivet shear failure of the joint indicated in Figure 7.11. Dashed circles show the location of the rivet

The rotation of the rivet in a specimen failing by bearing/rivet failure mode was examined by X-ray radiography; a sample radiograph is shown in Figure 7.16. In general, when a riveted single-lap shear joint is subjected to tensile loading, asymmetric load transfer takes place related to the geometry of the joint. This results in heterogeneous bearing pressure at the rivet–hole interface (i.e. a knife-edge like contact) in both composite partners. Such nonuniform stress distribution causes out-of-plane bending of the joint, or “secondary bending” [106]. Secondary bending in a bolted single-lap shear joint subjected to tensile loading is shown schematically



in Figure 7.17. Once secondary bending begins to rotate the rivet, clamping pressure decreases and the load is carried by the bending rivet until the joint finally fails by rivet bending failure. Secondary bending may be reduced by making the joint more symmetrical – for example, by adopting double-lap shear joint geometry [4].

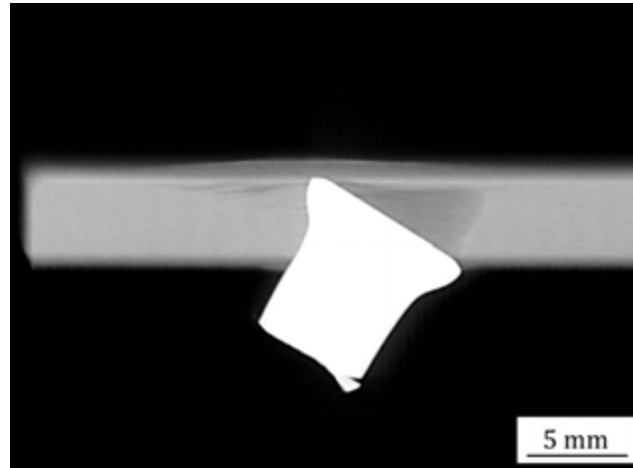


**Figure 7.16.** Rivet rotation and out-of-plane accumulated plastic deformation at a friction-riveted single-lap shear joint failing by bearing/rivet failure mode

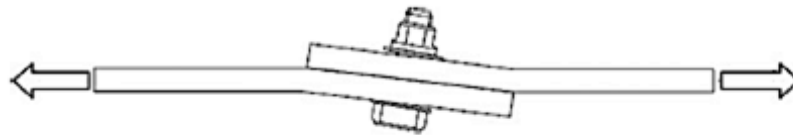


**Figure 7.17.** Schematic representation of secondary bending and rivet rotation under tensile loading due to the asymmetric geometry of a single-lap shear joint, adapted from [106]

## 7.5. Mechanical performance of friction-riveted and state-of-the-art mechanically fastened joints

In order to place the mechanical performance of the friction-riveted single-lap shear joints into context, they were compared to state-of-the-art single-lap shear bolted joints, assembled in accordance with Airbus standards. The ultimate goal of every joining technology is to reach the base material strength of the joining partners. Joint efficiency is defined as the ultimate joint strength compared to the base material strength [29]. Three reference joints were produced using the same PEEK composite material as had been used for the friction-riveted single-lap shear joints.

These reference joints, produced by Airbus Germany have an edge distance of  $3d$  and a width of  $5d$ , where  $d = 5$  mm. The friction-riveted joints were produced with the same geometry for comparison purposes. The reference joints were bolted using Ti6Al4V LGP<sup>®</sup> lockbolts (standard no. ASNA2041) from ALCOA (Hildesheim, Germany) having an actual diameter of 4.8 mm (nominal diameter 5 mm). The through holes drilled prior to the installation of the fasteners had a diameter of 4.82 mm. The lockbolts were installed at an Airbus facility in accordance with the internal standard procedures generally used to install these lockbolts in composite materials; an example is shown in Figure 7.18.



**Figure 7.18.** X-ray radiograph of a state-of-the-art mechanically fastened Airbus reference joint

The Airbus reference joints were tested alongside friction-riveted joints following the procedure set out in Section 4.8.4. The ultimate joint strength was calculated according to the failure mode (initial bearing failure, Equation 7.3).

The results for the reference joints compared with the friction-riveted single-lap shear joints are presented in Table 7.8. The reference joints reached an average ultimate lap shear force of  $9.3 \text{ kN} \pm 0.2 \text{ kN}$ ; the friction-riveted joints reached an average ultimate lap shear force of  $8.1 \text{ kN} \pm 0.3 \text{ kN}$ . All of the joints failed initially in bearing followed by a final rivet failure, similar to the failure evolution for friction-riveted joints.

**Table 7.8.** Average ultimate force, failure mode and displacement at failure for friction-riveted single-lap shear joints and mechanically fastened Airbus reference joints

	FricRiveted joint	Bolted Airbus joint
Ultimate load [kN]	$8.1 \pm 0.3$	$9.3 \pm 0.2$
Displacement at failure [mm]	$4.5 \pm 0.3$	$7.7 \pm 0.7$
Failure mode	Bearing + rivet shearing	Bearing + rivet shearing

Figure 7.19 compares the force–displacement curves for a friction-riveted single-lap shear and a mechanically fastened reference joint. The slope of the elastic deformation segment of the reference joint curve is steeper than for the friction-riveted joint, indicating a higher stiffness of the reference joint [102]. This behaviour might be explained by the high clamping pressure obtained from the installation of the lockbolt related to the geometry of the clamping nut. For the reference joints, the initial linear segment of the force–displacement curve was followed by a nonlinear region with a significant loss in stiffness (decreased slope), indicating progressive accumulating damage [101]. Table 7.8 and Figure 7.19 also show that the

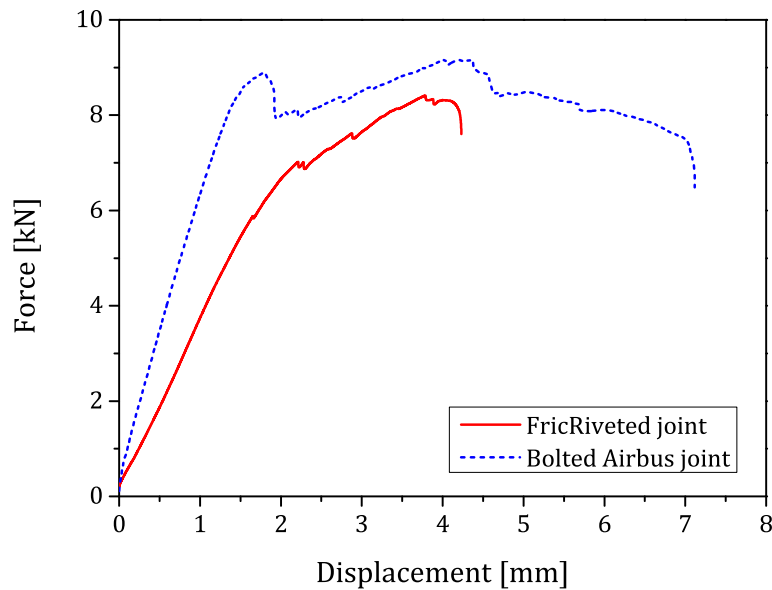


**Figure 7.19.** Force–displacement curves comparing a friction-riveted joint with a mechanically fastened Airbus reference joint

displacement at failure of the two joint types were significantly different, with the reference joints having a higher average displacement at failure ( $7.7\text{ mm}\pm 0.7\text{ mm}$ ) than the friction-riveted joints ( $4.45\text{ mm}\pm 0.3\text{ mm}$ ). These findings indicate that the load was carried for a much longer time and that the failure of the reference joints took place with a much higher energy absorption [103]. These higher ultimate lap shear forces and displacements at failure of the reference joints may be explained by the higher shear strength of Ti6Al4V (760 MPa [55]), twice that of the grade 3 titanium used in the friction-riveted joints (380 MPa [55]).

Figure 7.20 compares the joint efficiencies of the friction-riveted single-lap shear joint and the Airbus reference joint, calculated for both joint types by Equation 7.5 adapted from [29,107], where  $F^{bru}$  is the joint strength and  $F^{tu}$  the ultimate tensile strength of the rivet base material (Table 4.1, Section 4.1.1). The joint efficiency was 0.7 for the friction-riveted joint and 0.5 for the bolted reference joint, which represents a joint efficiency increase of 21% for the friction-riveted joints. The difference may be explained by the different properties of the rivet materials used in the two joining technologies. Although the ultimate load-carrying capacity of the friction-riveted joints is lower than for the reference joints, the joint efficiency of the friction-riveted joints is higher because of the lower tensile strength of the rivet material. It is believed that the load-carrying capacity of the friction-riveted joints might be improved by using Ti6Al4V as rivet material. To do this, a different process parameter set for the development of an anchoring feature inside the composite

substrate would need to be developed, which was not part of this work but will present a subject of future work.

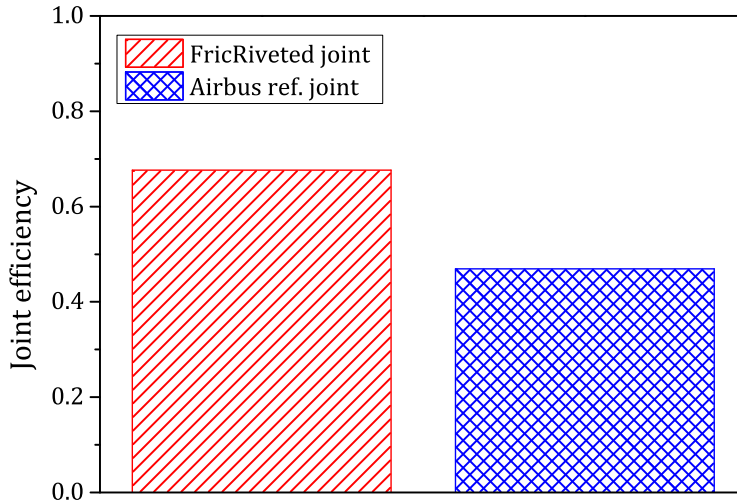


**Figure 7.20.** Comparison of the joint efficiency of the friction-riveted and the Airbus reference joints

$$J = \frac{F^{bru}}{F^{tu}} \quad (7.5)$$

## 7.6. Summary and conclusion

In this chapter it was demonstrated that the optimised process parameter set for friction-riveted PEEK-CA30/grade3 Ti metallic-insert joints, developed using RSM 400 equipment, was transferable to the new RNA system. Additionally, the feasibility of joining woven fabric-reinforced PEEK and grade3 titanium was accomplished by adjusting the process parameters set to this new material combination using the established relationships between the process parameters and the process outcome. The key design parameters for friction-riveted single-lap shear joints were determined by analysing the influence of the edge distance, the clamping torque and the specimen width on the joint mechanical performance. Finally, the friction-riveted joints were compared to state-of-the-art mechanically fastened reference joints provided by Airbus Germany. The results obtained within the framework of this investigation led to the following conclusions:

- The three prerequisites (comparability in "monitoring of the process parameters and torque", compatibility in "geometry of the rivet anchoring zone" and equality in "quasi-static mechanical performance") identified to demonstrate transferability of the results obtained with the RSM 400 system to the new RNA system were fulfilled. It was shown that the evolution over time of the process parameters and torque of both systems matched reasonably well, and the shape and dimensions of the anchoring zone in both systems showed negligible differences and the quasi-static mechanical performances of the joints were also demonstrated to be equivalent.
- The feasibility of FricRiveting was demonstrated for the challenging material combination of woven fabric-reinforced PEEK laminates and titanium grade 3.
- The process parameter set, optimised for friction-riveted PEEK-CA30/grade 3 Ti metallic-insert joints (Chapter 6) was successfully adjusted for woven fabric-reinforced PEEK laminates by using the results from the DoE study carried out on short carbon fibre-reinforced metallic-insert joints. The adjusted process parameter set was: RS: 19000 rpm, FT: 1 s, FP: 4.6 kN, FoT: 10 s and FoP: 5.8 kN.
- It was demonstrated that, although the woven fabric-reinforced PEEK substrate material possessed different properties from those of the short carbon fibre-reinforced PEEK – different amount of fibres and different fibre type, for example – the trends in the relationships between the process parameters and properties were found to be reasonably valid and could be used to adjust the process parameter set.
- The investigation of the influence of edge distance, rivet clamping torque and specimen width on the mechanical performance of the joint led to the development of an optimised friction-riveted single-lap shear joint (edge distance  $3d$ , clamping torque 5 Nm and specimen width  $6d$ ), which fulfilled the aircraft industry requirements of combining high strength with non-catastrophic failure type.
- The optimised friction-riveted single-lap shear joint showed an increase in joint efficiency of 21% over that of state-of-the-art mechanically fastened joints provided by Airbus Germany.

## 8. Final remarks

The objectives addressed within the framework of this thesis were the application of the FricRiveting technology to carbon fibre-reinforced material and titanium, through the determination of the effect of the carbon fibre reinforcement on the joinability, as well as the investigation of the effect of the process parameters on the joint formation, microstructure and the joint mechanical performance, as well as the design and analysis of a high-performance friction-riveted composite-composite single-lap shear joint that fulfils aircraft industry requirements. From the results of the experimental work and analyses the following final conclusions were drawn.

- It was experimentally demonstrated that FricRiveting on commercially pure titanium (grades 1, 2 and 3) and PEEK substrates is feasible. For Ti6Al4V as rivet material, the formation of an anchoring feature inside the polymer substrate was not achieved due to the limitations of the available RSM 400 equipment. It was assumed that the energy generated during the FricRiveting process was insufficient to widen the rivet tip due to the higher strength of the Ti6Al4V rivet. Future investigation in the newly built RNA equipment, allowing the use of higher friction and forging forces, may allow the plasticizing and formation of Ti6Al4V rivet anchoring zones.
- The feasibility of FricRiveting was experimentally proven for the challenging material combination of short carbon fibre-reinforced PEEK and titanium grade 3. The FricRiveting system (RSM 400) was improved by implementing a differential pressure sensor, allowing the calibration of high-friction pressure levels, resulting in a significant decrease of the maximum standard deviation.
- The analysis of the DoE model was used to identify optimised process parameter sets depending on the joint requirements; therefore, the joint formation and mechanical performance was tailored to the specific requirements of particular applications. To obtain shallower rivet penetration depths or low mechanical energy input (e.g., to avoid possible thermal degradation of the polymer matrix), the RS, FT and FP must be assigned low values. The FoP was shown to have less impact on these responses; therefore may be kept constant for different applications. To increase the mushrooming efficiency and the pull-out force, the RS, FT and FoP must be assigned high values, while the FP needs to be set at the intermediate level. An optimised process parameter-set leading to improved pull-out performance was developed using ANOVA.
- For the metallic-insert joints made of PEEK containing 30% short carbon fibres and grade 3 titanium, a mushrooming efficiency of 70% led to the maximal

---

pull-out performance of 10.6 kN. At this 70% efficiency threshold, the failure mode of the joint changes from failure mode III (pull-out of rivet) to failure mode I (rivet failure). Joints failing through the titanium rivet displayed values similar to the ultimate tensile strength of titanium itself. Therefore, the joint performance can be improved by selecting a rivet material having a higher tensile strength once the preferred failure mode, rivet failure, was achieved.

- The microstructure of FricRiveted joints was significantly affected by the high rates of heating and deformation related to the FricRiveting joining process. The influence of the process on the titanium rivet and on the composite substrate were investigated using the optimised metallic-insert joint made of PEEK reinforced with 30% short carbon fibres and grade 3 titanium. The microstructural characterisation of the joining region allowed the identification of several microstructural zones both in the metal and in the composite component of the joint. Seven zones were found to be present at the joining area. In the composite part, these were the composite base material (CBM); composite heat-affected zone (CHAZ); composite thermomechanically affected zone (CTMAZ); and the composite stir zone (CSZ). The zones identified in the metal component were the metal thermomechanically affected zones 1 and 2 (MTMAZ-1 and MTMAZ-2) and the metal friction zone (MFZ). A model representing the material flow was introduced which was developed from observation of the orientation of the short carbon fibres that were partially reoriented during the process.
- Thermogravimetric analysis indicated that the FricRiveting process did not significantly induced thermo-mechanical degradation to the composites polymeric matrix in the vicinity of the rotating titanium rivet. These findings are explained by consideration of the measured process temperatures. The highest temperature recorded was 480 °C, far below the onset temperature of the first decomposition step that occurs in PEEK reinforced with 30% short carbon fibres at 586 °C
- It was experimentally demonstrated that FricRiveting of fabric-reinforced PEEK (TPCL PEEK) and grade 3 titanium is feasible. The previously optimised process parameter set for short carbon fibre-reinforced PEEK needed to be adapted to the fabric-reinforced substrate. The substrate material contains different amounts (from 30 wt% to 58 wt%), types (short and woven) and distribution of reinforcement fibres, so that different frictional and rheological properties affect the heat generation; it was nevertheless shown that trends in relationships between the process parameters and joint properties remained reasonably valid. Therefore an optimised process parameter set for woven fabric-reinforced PEEK laminates was defined from the knowledge gained about the relationships between process parameters and joint formation for short carbon fibre-reinforced PEEK.

- The results of the design study on friction-riveted woven fabric-reinforced PEEK laminate/grade 3 titanium single-lap shear joints led to the definition of an optimised joint configuration, fulfilling the requirements of high strength accompanied by a non-catastrophic failure mode. These requirements were met when using an edge distance of  $3d$ , a clamping torque of 5 Nm and a joint width of  $6d$ .
- The friction-riveted single-lap shear joints were compared with state-of-the-art mechanically fastened reference joints provided by Airbus Germany. The friction-riveted joints had a joint efficiency (which is the joint strength divided by the strength of the rivet material) of 0.7 and the bolted reference joint had a joint efficiency of 0.5. The optimised friction-riveted single-lap shear joints therefore achieved a joint efficiency 21% higher than the state-of-the-art mechanically fastened reference joints, showing the potential of the FricRiveting technology for composite aircraft structures.



## 9. Recommendations for future work

FricRiveting is still a very new technology and in its pioneering stage as a potential joining process for composite structures, especially for aircraft applications. Therefore, further research will still be necessary in order to obtain a better understanding of the technology and to identify potential applications. The next steps in future research should be focusing on:

- The feasibility study for Ti6Al4V as rivet material using the newly built RNA equipment might lead to the formation of the anchoring feature inside the polymer/composite substrate. It is believed that the use of higher friction and forging forces in combination with the displacement control operation mode, available with the RNA equipment, may generate the energy level, allowing the plasticizing and formation of Ti6Al4V rivet anchoring zones.
- A detailed investigation of the microstructural changes, in the composite joint regions, by microhardness and nanoindentation testing in order to precisely characterize the local mechanical properties.
- Further investigation of the MTMAZ-1/MTMAZ-2 interface would be necessary to determine the exact location and shape of this boundary. In order to accomplish this, the surface preparation method for pure titanium needs to be improved, allowing a larger EBSD scan, covering the whole boundary region of both zones.
- The investigation of the fatigue behavior, the impact resistance (joint toughness) and the influence of environmental conditions (extreme temperatures, fluids, etc.) on the friction riveted joints (metallic-insert and single lap shear joints) would provide further information on the joint performance and durability, which would allow the transfer of the FricRiveting technology into aircraft applications.

# Bibliography

- [1] Lohner H. Hochleistungswerkstoffe und -technologien für modern Flugzeuge. In *Zweites Dresdener Werkstoffsymposium*, Dresden 2011.
- [2] Zepf HP. *Faserverbundwerkstoffe mit thermoplastischer Matrix*, volume 529 of *Kontakt & Studium*. Expert-Verlag, Renningen-Malmsheim, 1997.
- [3] Vasiliev VV and Morozov EV. *Mechanics and Analysis of Composite Materials*. Elsevier Science Ltd., Oxford, 2001.
- [4] Peters ST. *Handbook of Composites*. Chapman & Hall, London, second edition, 1998.
- [5] Messler Jr R W. *Joining Composite Materials and Structures*, pages 647–696. Butterworth-Heinemann, Burlington, 2004.
- [6] Stokes VK. Joining methods for plastics and plastic composites: An overview. *Polymer Engineering and Science*, 29(19):1310–1324, 1989.
- [7] Maguire DM. Joining thermoplastic composites. *SAMPE Journal*, 25(1):11–14, 1989.
- [8] Rudolf R, Mitschang P, Neitzel M, and Rueckert C. Welding of high-performance thermoplastic composites. *Polymer and Polymer Composites*, 7(5):309–315, 1999.
- [9] Yousefpour A, Hojjati M, and Immarigeon J-P. Fusion bonding/welding of thermoplastic composites. *Journal of Thermoplastic Composite Materials*, 17(4):303–341, 2004.
- [10] Amancio-Filho ST and Santos dos JF. Joining of polymers and polymer-metal hybrid structures: Recent developments and trends. *Polymer engineering and Science*, 49:1461–76, 2009.
- [11] Messler Jr Robert W. The challenges for joining to keep pace with advancing materials and designs. *Materials & Design*, 16(5):261–269, 1996.
- [12] Ageorges C, Ye L, and Hou M. Advances in fusion bonding techniques for joining thermoplastic matrix composites: A review. *Composites Part A: Applied Science and Manufacturing*, 32(6):839 – 857, 2001.
- [13] Ahmed TJ, Stavrov D, Bersee HEN, and Beukers A. Induction welding of thermoplastic composites: An overview. *Composites Part A: Applied Science and Manufacturing*, 37(10):1638–1651, 2006.

- 
- [14] Ageorges C and Ye L. Resistance welding of metal/thermoplastic composite joints. *Journal of Thermoplastic Composite Materials*, 14(6):449–475, 2001.
- [15] Stavrov D and Bersee HEN. Resistance welding of thermoplastic composites: An overview. *Composites Part A: Applied Science and Manufacturing*, 36(1):39–54, 2005.
- [16] Knapp W, Clement S, Franz C, Oumarou M, and Renard J. Laser-bonding of long fiber thermoplastic composites for structural assemblies. *Physics Procedia*, 5, Part B(0):163–171, 2010.
- [17] Goushegir SM, Santos dos JF, and Amancio-Filho ST. Friction spot joining of aluminum AA2024/carbon-fiber reinforced poly(phenylene sulfide) composite single lap joints: Microstructure and mechanical performance. *Materials and Design*, 54:196–206, 2013.
- [18] Amancio-Filho ST and Santos dos FJ. EP 2 329 905 B1 - Method for joining metal and plastic workpieces, European Patent Office 2012.
- [19] Abibe AB, Amancio-Filho ST, Santos dos JF, and Hage JR E. Development and analysis of a new joining method for polymer-metal hybrid structures. *Journal of thermoplastic composites and materials*, 24:233–249, 2011.
- [20] Abibe AB, Amancio-Filho ST, Santos dos JF, and Hage Jr E. Mechanical and failure behaviour of hybrid polymer-metal staked joints. *Materials and Design*, 46:338–347, 2013.
- [21] Amancio-Filho ST, Santos dos FJ, and Beyer M. US 8 025 827 B2 - Method and device for connecting a plastic workpiece to a further workpiece, U.S. Patent Office 2011.
- [22] Amancio-Filho ST, Beyer M, and Santos dos JF. US 7 575 149 B2 - Method of connecting a metallic bolt to a plastic workpiece, U.S. Patent Office 2009.
- [23] Amancio-Filho ST, Beyer M, and Santos dos JF. EP 1 790 462 B1 - Verfahren zum Verbinden eines metallischen Bolzens mit einem Kunststoff-Werkstück, 2011.
- [24] Amancio-Filho ST and Santos dos JF. Fricriveting: A new joining technique for thermoplastics-lightweight alloy structures. *Materials Science and Technology*, pages 2362 – 2373, 2008.
- [25] Amancio-Filho ST. *Friction Riveting: Development and analysis of a new joining technique for polymer-metal multi-materials structures*. PhD thesis at hamburg university of technology, Germany 2007.
- [26] Hart-Smith LJ. *ASM Handbook Composites*, chapter Bolted and Bonded Joints. ASM International, 2001.
- [27] Thoppul SD, Finegan J, and Gibson RF. Mechanics of mechanically fastened joints in polymer-matrix composite structures - A review. *Composites Science and Technology*, 69(3-4):301 – 329, 2009.

- [28] Gintert LA. *ASM Handbook Composites*, chapter Element and Subcomponent Testing, pages 778–793. ASM International, 2001.
- [29] Hart-Smith LJ. *Joining fiber-reinforced plastics-Chapter 6: Design and Empirical Analysis of Bolted or Riveted Joints*. Elsevier Applied Science, 1987.
- [30] Camanho PP and Lambert M. Design methodology for mechanically fastened joints in laminated composite materials. *Composites Science and Technology*, 66(15):3004 – 3020, 2006.
- [31] Cooper C. and Turvey GJ. Effects of joint geometry and bolt torque on the structural performance of single bolt tension joints in pultruded GRP sheet material. *Composite Structures*, 32(1-4):217 – 226, 1995.
- [32] ASTM D5961M 08 Standard test method for bearing response of polymer matrix composite laminates, 2008.
- [33] Jones RM. *Mechanics of Composite Materials*. Taylor & Francis Inc., Philadelphia 1998.
- [34] Niu MCY. *Airframe structural design*. Conmilit Press LTD., Hong Kong 1995.
- [35] Vinson JR. Adhesive bonding of polymer composites. *Polymer Engineering and Science*, 29(19):1325–1331, 1989.
- [36] ASTM D5573 99 Classifying failure modes in fiber-reinforced-plastic (FRP) joints.
- [37] Dubé M, Hubert P, Yousefpour A, and Denault J. Resistance welding of thermoplastic composites skin/stringer joints. *Composites Part A: Applied Science and Manufacturing*, 38(12):2541–2552, 2007.
- [38] Kelly G. Load transfer in hybrid (bonded/bolted) composite single-lap joints. *Composite Structures*, 69(1):35 – 43, 2005.
- [39] Kelly G. Quasi-static strength and fatigue life of hybrid (bonded/bolted) composite single-lap joints. *Composite Structures*, 72(1):119 – 129, 2006.
- [40] Lee YH, Lim DW, Choi JH, Kweon JH, and Yoon MK. Failure load evaluation and prediction of hybrid composite double lap joints. *Composite Structures*, 92:2916 – 2926, 2010.
- [41] Amancio-Filho ST, Roeder J, Nunes SP, Santos dos JF, and Beckmann F. Thermal degradation of polyetherimide joined by friction riveting (FricRiveting). part I: Influence of rotation speed. *Polymer Degradation and Stability*, 93(8):1529–38, 2008.
- [42] Amancio-Filho ST and Santos dos JF. Entwicklung des Reibnietens als neues Fügeverfahren für Kunststoff und Leichtbaulegierungen. *Materialwissenschaft und Werkstofftechnik*, 39(No.11):799 – 805, 2008.
- [43] Amancio-Filho ST. Friction riveting: Development and analysis of a new joining technique for polymer-metal multi-material structures. *Welding in the World*, 55(01 02):13 – 24, 2011.

- 
- [44] Stokes VK. Analysis of the friction (spin)-welding process for thermoplastics. *Journal of Materials Science*, 23(8):2772–2785, 1988.
- [45] Crawford RJ and Tam Y. Friction welding of plastics. *Journal of Materials Science*, 16(12):3275–3282, 1981.
- [46] Ma TJ, Li WY, and Yang SY. Impact toughness and fracture analysis of linear friction welded Ti-6Al-4V alloy joints. *Materials and Design*, 30:2128 – 2132, 2009.
- [47] Vairis A and Frost M. Modelling the linear friction welding of titanium blocks. *Materials Science and Engineering A*, 292(1):8–17, 2000.
- [48] Crossland B. Friction welding. *Contemporary Physics*, 12(6):559–574, 1971.
- [49] *Dubbel: Taschenbuch für den Maschinenbau*, volume 17. Beitz, W and Küttner, KH, 1990.
- [50] Amancio-Filho ST dos Santos FJ. Influence of processing parameters on microstructure and properties of a polyetherimide joined by FricRiveting: Investigation of rotational speed. In *67th Annual technical conference of the society of plastics engineers, ANTEC 2009*, Chicago, 2009.
- [51] Amancio-Filho ST and Santos dos V, JFand Ventzke. Determination of fracture mechanisms under tensile loading in a commercial available engineering thermoplastic material joined by FricRiveting. In *5th International conference on fracture of polymers, composites and adhesives*, Switzerland: Les Diablerets 2009.
- [52] Rodrigues CF, Blaga LA, Santos dos JF, Canto LB, Hage Jr. E, and Amancio-Filho ST. FricRiveting of aluminum 2024-T351 and polycarbonate: Temperature evolution, microstructure and mechanical performance. *Journal of Materials Processing Technology*, 214(0):2029 – 2039, 2014.
- [53] Blaga L, Bancila R, and Santos dos ST, JFand Amancio-Filho. Friction riveting of glass-fibre-reinforced polyetherimide composite and titanium grade 2 hybrid joints. *Materials and Design*, 50:825–829, 2013.
- [54] Blaga L. *Innovating materials in bridge construction. Contribution to construction with composite fiber reinforced materials*. Thesis, Politehnica Timisoara, 2012.
- [55] Boyer R, Welsch G, and Collings EW. *Materials properties handbook: Titanium alloys*. ASM International, 1998.
- [56] Lütjering G and Williams JC. *Titanium*. Springer-Verlag Berlin Heidelberg, 2007.
- [57] Zwicker U. *Titan und Titanlegierungen*. Springer-Verlag, Berlin Heidelberg New York, 1974.
- [58] Brydson JA. *Plastic Materials*. Butterworth-Heinemann, Oxford 1999.

- [59] Harper CA. *Handbook of plastics, elastomers & composites*. McGrawHill Handbooks, New York 2002.
- [60] Mark JE, editor. *Polymer Data Handbook*. Oxford University Press, Oxford 1999.
- [61] Mata F, Gaitonde VN, Karnik SR, and Pavo Davim J. Influence of cutting conditions on machinability aspects of peek, peek cf 30 and peek gf 30 composites using pcd tools. *Journal of Materials Processing Technology*, 209(4):1980–1987, 2009.
- [62] Kurtz SM and Devine JN. PEEK biomaterials in trauma, orthopedic, and spinal implants. *Biomaterials*, 28(32):4845–4869, 2007.
- [63] Patel P, Hull TR, McCabe RW, Flath D, Grasmeder J, and Percy M. Mechanism of thermal decomposition of poly(ether ether ketone) (PEEK) from a review of decomposition studies. *Polymer Degradation and Stability*, 95(5):709 – 718, 2010.
- [64] Ketron peek. Technical report, Arthur Krüger Technik in Kunststoffen, 2012.
- [65] Mishra AK and Schultz JM. Kinetics of strain-induced crystallization during injection molding of short fiber composites of poly(ether ether ketone). *Polymer Composites*, 12(3):169–178, 1991.
- [66] Sarasua JR, Remiro PM, and Pouyet J. The mechanical behaviour of peek short fibre composites. *Journal of Materials Science*, 30(13):3501–3508, 1995. *Journal of Materials Science*.
- [67] Harper CA, editor. *Modern Plastics Handbook*. McGraw-Hill Companies, Inc., New York 1999.
- [68] Tenax Toho. Product data sheet tenax-E TPCL PEEK-HTA40. Technical report, Toho Tenax Europe GmbH, 2012.
- [69] Harms & Wende GmbH & Co. KG. *RSM400 Reinschweiß-System*.
- [70] Harms & Wende GmbH & Co. KG, Hamburg, Germany. *Reibschweißköpfe RSM400 RK - Technisches Handbuch 24651 4-29433-2*, 2006.
- [71] Mathews PG. *Design of experiments with MINITAB*. American Society for Quality, Quality Press, Milwaukee, 2004.
- [72] Schmidt SR and Launsby RG. *Understanding industrial designed experiments*. Air Academy Press & Associates, Colorado Springs 2008.
- [73] Kleppmann W. *Taschenbuch Versuchsplanung*. Carl Hanser Verlag, München 2001.
- [74] Montgomery DC. *Design and analysis of experiments*. John Wiley & Sons, Inc., New York 1991.
- [75] Rapp R. US 3 348 486 A - Plastic-lead mushrooming bullet, U.S. Patent Office 1967.

- 
- [76] Hawkyard JB, Eaton D, and Johnson W. The mean dynamic yield strength of copper and low carbon steel at elevated temperatures from measurements of the mushrooming of flat-ended projectiles. *International Journal of Mechanical Sciences*, 10(12):929–930, 1968.
- [77] Hawkyard JB. A theory for the mushrooming of flat-ended projectiles impinging on a flat rigid anvil, using energy considerations. *International Journal of Mechanical Sciences*, 11(3):313–333, 1969.
- [78] Wang B and Lu G. Mushrooming of circular tubes under dynamic axial loading. *Thin-Walled Structures*, 40(2):167–182, 2002.
- [79] Balendra R and Travis FW. An examination of the double-frustum phenomenon in the mushrooming of cylindrical projectiles upon high-speed impact with a rigid anvil. *International Journal of Mechanical Sciences*, 13(6):495–505, 1971.
- [80] DIN EN 1435 Deutsches Institut für Normung e.V. Radiographic testing of welded joints, September 2002.
- [81] Struers . *Secotom 15/50*. Struers, 62110599 edition, November 2013.
- [82] Vander Voort GF. *Metallography principles and practice*. ASM International, 1999.
- [83] Petzow G. *Metallographisches keramographisches plastographisches Ätzen*. Gebrüder Borntraeger, Berlin Stuttgart, 1994.
- [84] ASTM E 1131 08 Standard test method for compositional analysis by thermogravimetry.
- [85] DIN EN 2591 Elektrische und optische Verbindungselemente, 1992.
- [86] Blaga ST, Land Amancio-Filho, Santos dos JF, and Bancila R. FricRiveting of civil engineering composite laminates for bridge construction. In *70th Annual technical conference of the society of plastics engineers, ANTEC 2012*, Orlando, FL 2012.
- [87] Committee ASM Handbook, editor. *ASM Handbook Properties and Selection: Nonferrous Alloys and Special-Purpose Materials*. ASM International, 1992.
- [88] Neter J, Wasserman W, and Kutner M. *Applied Linear Statistical Models*. McGraw-Hill Companies, Inc./Irwin, 1990.
- [89] Hayajneh MT, Tahat MS, and Bluhm J. A study of the effects of machining parameters on the surface roughness in the end-milling process. *Jordan Journal of Mechanical and Industrial Engineering*, 1:1 – 5, 2007.
- [90] Mironov S., Sato YS, and Kokawa H. Development of grain structure during friction stir welding of pure titanium. *Acta Materialia*, 57(15):4519 – 4528, 2009.
- [91] Zhang MQ, Lu ZP, and Friedrich K. Thermal analysis of the wear debris of polyetheretherketone. *Tribology International*, 30(2):103–111, 1997.

- [92] Meenan BJ, McClorey C, and Akay M. Thermal analysis studies of poly(etheretherketone)/hydroxyapatite biocomposite mixtures. *Journal of Materials Science: Materials in Medicine*, 11(8):481–489, 2000.
- [93] Committee ASM Handbook, editor. *ASM Handbook Forming and Forging*. ASM International, 1993.
- [94] Zeng Z, Jonsson S, and Roven HJ. The effects of deformation conditions on microstructure and texture of commercially pure Ti. *Acta Materialia*, 57(19):5822–5833, 2009.
- [95] Engler O and Randle V. *Introduction to Texture Analysis: Macrotexture, Microtexture, and Orientation Mapping*. CRC Press, 2009.
- [96] Mironov S, Sato YS, Kokawa H, Inoue H, and Tsuge S. Structural response of superaustenitic stainless steel to friction stir welding. *Acta Materialia*, 59:5472–5481, 2011.
- [97] Williams JC, Baggerly RG, and Paton NE. Deformation behavior of HCP Ti-Al alloy single crystals. *Metallurgical and Materials Transactions A*, 33(3):837–850, 2002.
- [98] Suhuddin U, Mironov S, Krohn H, Beyer M, and Santos dos FJ. Microstructural evolution during friction surfacing of dissimilar aluminum alloys. *Metallurgical and Materials Transactions A*, 43A:5224–31, 2012.
- [99] Hay JN and Kemmish DJ. Thermal decomposition of poly(aryl ether ketones). *Polymer*, 28(12):2047 – 2051, 1987.
- [100] Patel P, Hull TR, Lyon RE, Stoliarov SI, Walters RN, Crowley S, and Safronava N. Investigation of the thermal decomposition and flammability of PEEK and its carbon and glass-fibre composites. *Polymer Degradation and Stability*, 96(1):12 – 22, 2011.
- [101] Kelly G and Hallström S. Bearing strength of carbon fibre/epoxy laminates: effects of bolt-hole clearance. *Composites Part B: Engineering*, 35(4):331 – 343, 2004.
- [102] Khashaba UA, Sallam HEM, Al-Shorbagy AE, and Seif MA. Effect of washer size and tightening torque on the performance of bolted joints in composite structures. *Composite Structures*, 73(3):310 – 317, 2006.
- [103] Moroni F, Pirondi A, and Kleiner F. Experimental analysis and comparison of the strength of simple and hybrid structural joints. *International Journal of Adhesion and Adhesives*, In Press, Corrected Proof:–, 2010.
- [104] Atas A and Soutis C. Subcritical damage mechanisms of bolted joints in CFRP composite laminates. *Composites Part B: Engineering*, 54(0):20 – 27, 2013.
- [105] Baker A, Dutton S, and Kelly D. *Composite Materials for Aircraft Structures*. American Institute of Aeronautics and Astronautics, Inc., Reston 2004.



- [106] Vieille B, Aucher J, and Taleb L. Woven ply thermoplastic laminates under severe conditions: Notched laminates and bolted joints. *Composites: Part B*, 42:341–349, 2011.
- [107] Crosky A, Kelly D, Li R, Legrand X, Huong N, and Ujjin R. Improvement of bearing strength of laminated composites. *Composite Structures*, 76(3):260 – 271, 2006.



# Appendices

# A. Appendix

## Feasibility study

**Table A.1.** Parameter configurations selected for the first trials of FricRiveting grade 1 titanium and PEEK

Configuration	Process setting parameters			
	RS [rpm]	FT [s]	FP [MPa]	FoP [MPa]
1	20000	1.5	0.4	0.55
2	18000	1.5	0.4	0.55
3	18000	1	0.4	0.55
4	18000	1.5	0.5	0.6
5	18000	1	0.5	0.6
6	18000	1	0.6	0.7
7	18000	1.5	0.6	0.7

**Table A.2.** Parameter configurations selected for the trials of FricRiveting grade 2 titanium and PEEK

Configuration	Process setting parameters			
	RS [rpm]	FT [s]	FP [MPa]	FoP [MPa]
1	20000	1	0.5	0.6
2	20000	1.5	0.5	0.6
3	20000	1	0.6	0.7
4	20000	1.5	0.6	0.7
5	18000	1	0.6	0.7
6	18000	1.5	0.6	0.7
7	18000	1	0.7	0.8
8	18000	1.5	0.7	0.8
9	20000	1	0.7	0.8
10	20000	1.5	0.7	0.8

**Table A.3.** Parameter configurations selected for the first trials of FricRiveting grade 3 titanium and PEEK

Configuration	Process setting parameters			
	RS [rpm]	FT [s]	FP [MPa]	FoP [MPa]
1	20000	1	0.5	0.6
2	20000	1.5	0.5	0.6
3	20000	1	0.6	0.7
4	20000	1.5	0.6	0.7
5	18000	1	0.6	0.7
6	18000	1.5	0.6	0.7
7	18000	1	0.7	0.8
8	18000	1.5	0.7	0.8
9	20000	1	0.7	0.8
10	20000	1.5	0.7	0.8

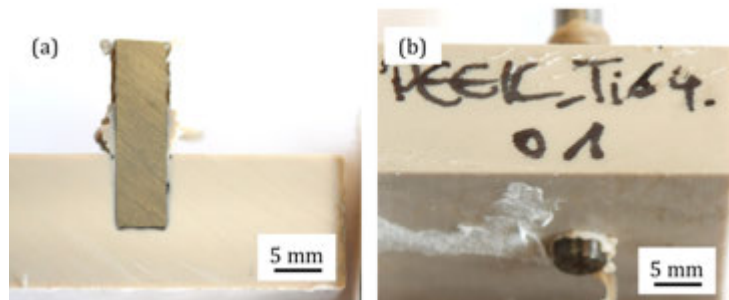


**Figure A.1.** Images used for the visual inspection of the metallic-insert joints made of Ti64 and PEEK; (a) low energy input (RS: 19000 rpm, FT: 1.5 s, FoP: 0.4 MPa, FP: 0.7 MPa and FoT: 1.5 s); (b) high energy input (RS: 20000 rpm, FT: 1.5 s, FoP: 1 MPa, FP: 0.8 MPa and FoT: 10 s)

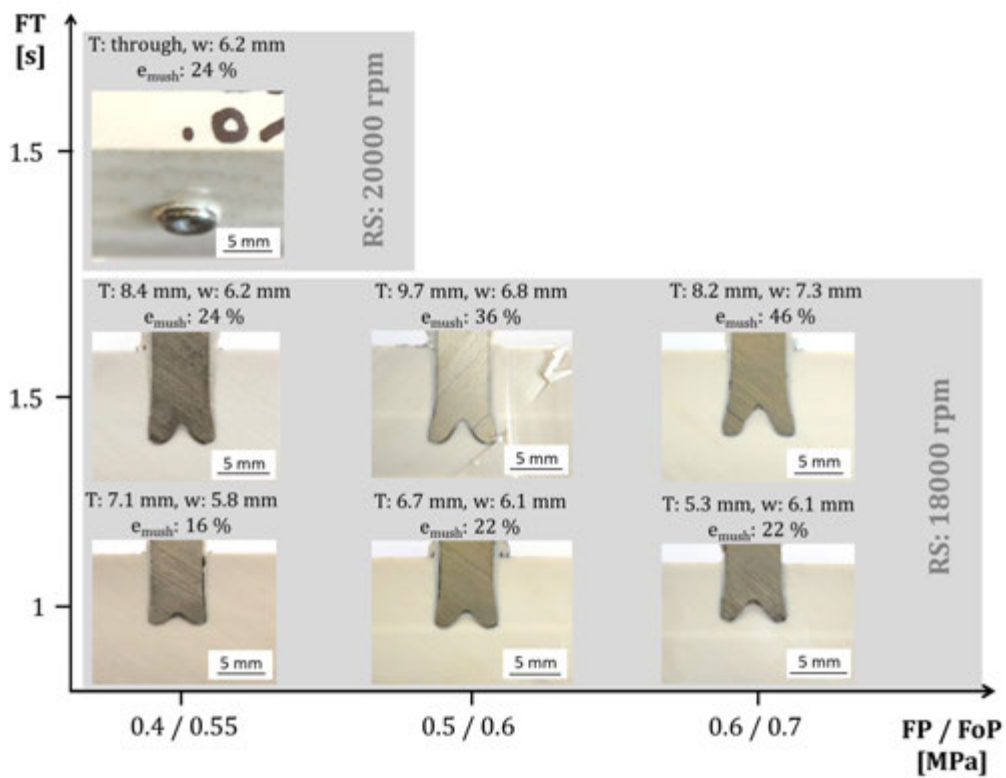


**Figure A.2.** Macrographs of cross-sections taken from the middle of the metallic-insert joints (PEEK and Ti grade 1), indicating penetration depth ( $T$ ), widening of the rivet tip ( $w$ ) and mushrooming efficiency ( $e_{mush}$ )

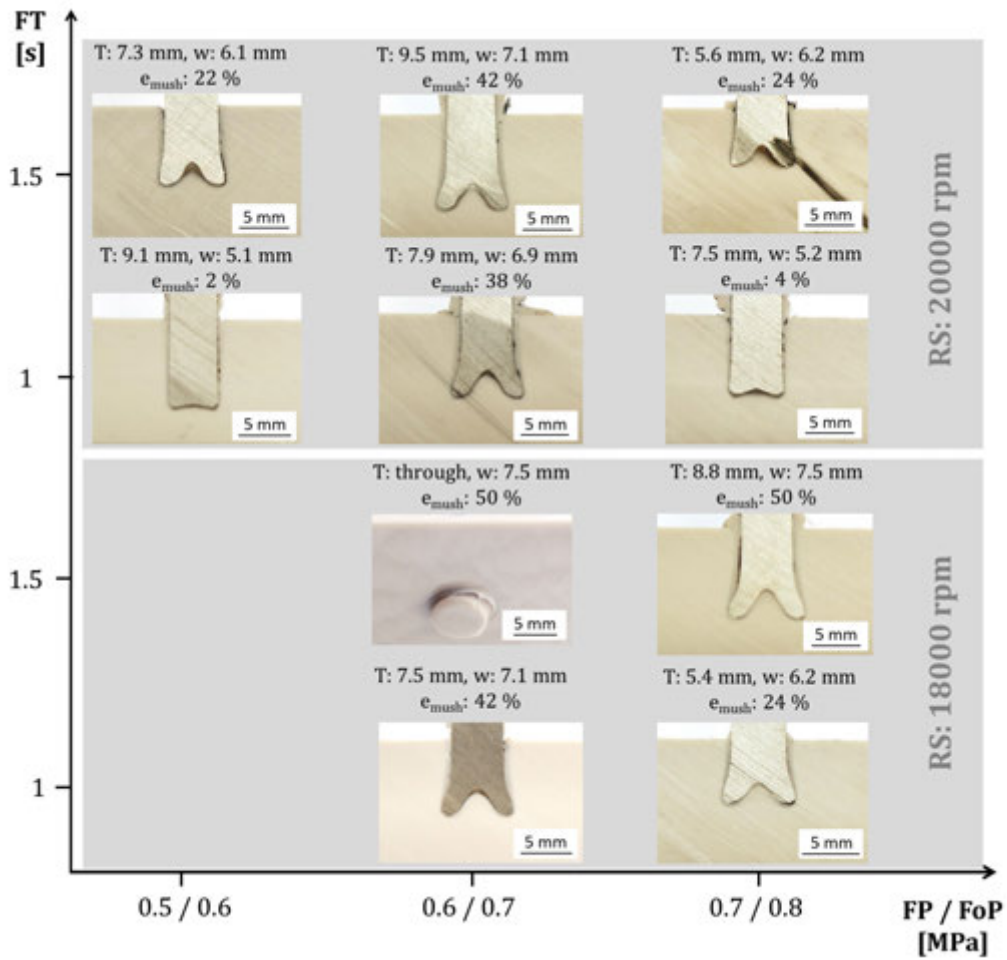


**Figure A.3.** Macrographs of cross-sections taken from the middle of the metallic-insert joints (PEEK and Ti grade 2), indicating penetration depth ( $T$ ), widening of the rivet tip ( $w$ ) and mushrooming efficiency ( $e_{mush}$ )

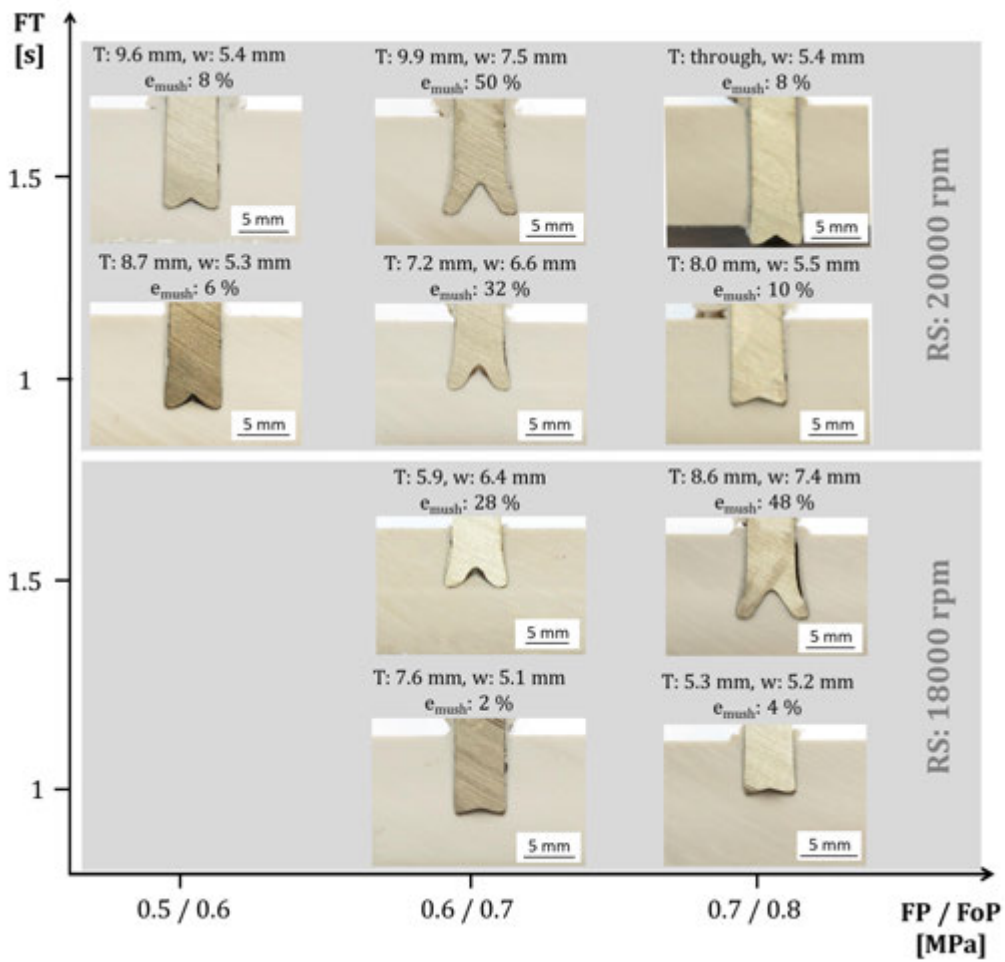


**Figure A.4.** Macrographs of cross-sections taken from the middle of the metallic-insert joints (PEEK and Ti grade 3), indicating penetration depth ( $T$ ), widening of the rivet tip ( $w$ ) and mushrooming efficiency ( $e_{mush}$ )



## B. Appendix

X-ray radiographes of PEEK/Ti grade 3 metallic-insert joints



**Figure B.1.** X-ray scans of FricRiveted metallic-insert joints made of PEEK and grade 3 titanium and joined using configuration 1 (see Table 5.1)

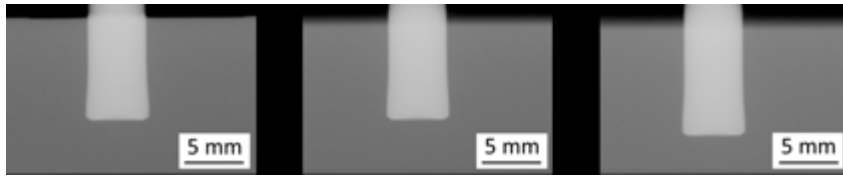


**Figure B.2.** X-ray scans of FricRiveted metallic-insert joints made of PEEK and grade 3 titanium and joined using configuration 2 (see Table 5.1)



**Figure B.3.** X-ray scans of FricRiveted metallic-insert joints made of PEEK and grade 3 titanium and joined using configuration 3 (see Table 5.1)

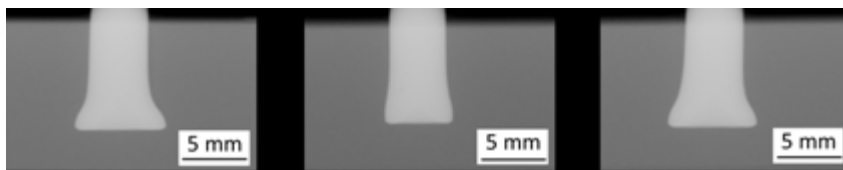


**Figure B.4.** X-ray scans of FricRiveted metallic-insert joints made of PEEK and grade 3 titanium and joined using configuration 4 (see Table 5.1)



**Figure B.5.** X-ray scans of FricRiveted metallic-insert joints made of PEEK and grade 3 titanium and joined using configuration 5 (see Table 5.1)



**Figure B.6.** X-ray scans of FricRiveted metallic-insert joints made of PEEK and grade 3 titanium and joined using configuration 6 (see Table 5.1)



**Figure B.7.** X-ray scans of FricRiveted metallic-insert joints made of PEEK and grade 3 titanium and joined using configuration 7 (see Table 5.1)

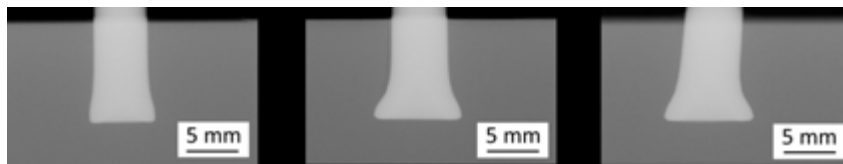


**Figure B.8.** X-ray scans of FricRiveted metallic-insert joints made of PEEK and grade 3 titanium and joined using configuration 8 (see Table 5.1)



**Figure B.9.** X-ray scans of FricRiveted metallic-insert joints made of PEEK and grade 3 titanium and joined using configuration 9 (see Table 5.1)



**Figure B.10.** X-ray scans of FricRiveted metallic-insert joints made of PEEK and grade 3 titanium and joined using configuration 10 (see Table 5.1)



**Figure B.11.** X-ray scans of FricRiveted metallic-insert joints made of PEEK and grade 3 titanium and joined using configuration 11 (see Table 5.1)

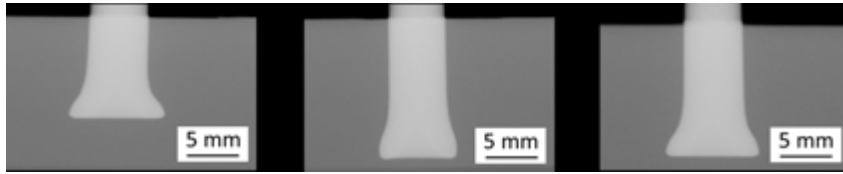


**Figure B.12.** X-ray scans of FricRiveted metallic-insert joints made of PEEK and grade 3 titanium and joined using configuration 12 (see Table 5.1)

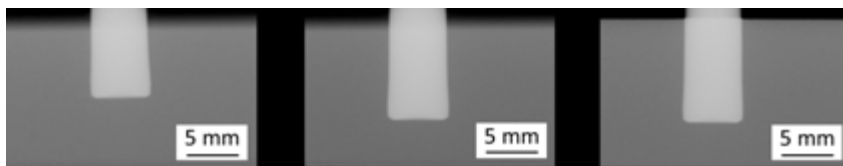


**Figure B.13.** X-ray scans of FricRiveted metallic-insert joints made of PEEK and grade 3 titanium and joined using configuration 13 (see Table 5.1)



**Figure B.14.** X-ray scans of FricRiveted metallic-insert joints made of PEEK and grade 3 titanium and joined using configuration 14 (see Table 5.1)

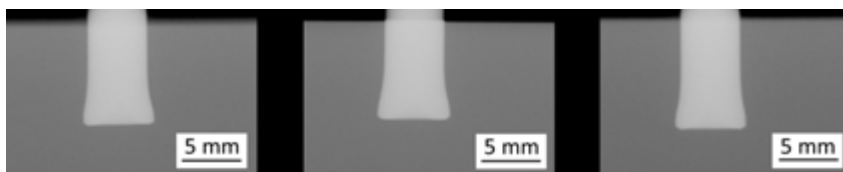


**Figure B.15.** X-ray scans of FricRiveted metallic-insert joints made of PEEK and grade 3 titanium and joined using configuration 15 (see Table 5.1)



**Figure B.16.** X-ray scans of FricRiveted metallic-insert joints made of PEEK and grade 3 titanium and joined using configuration 16 (see Table 5.1)

## C. Appendix

Mechanical performance of metallic-insert joints

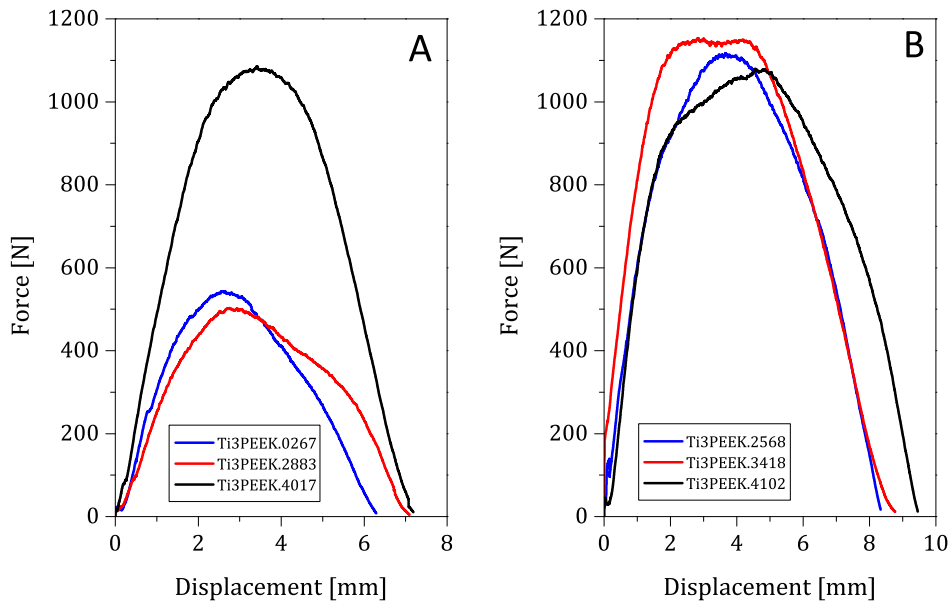


**Figure C.1.** Force–displacement curves of metallic-insert joints made of PEEK and grade 3 titanium; A: joined using configuration 1 and B: using configuration 2 (see Table 5.1)

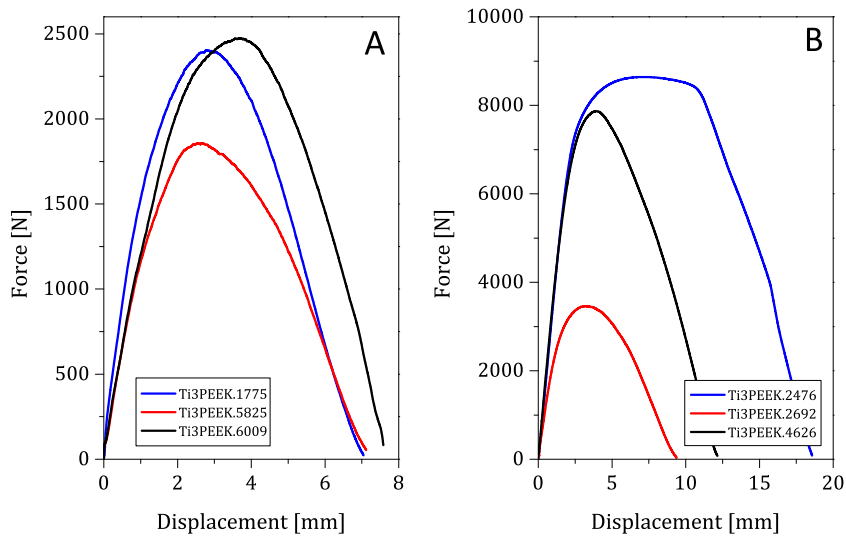


**Figure C.2.** Force-displacement curves of metallic-insert joints made of PEEK and grade 3 titanium; A: joined using configuration 3 and B: using configuration 4 (see Table 5.1)

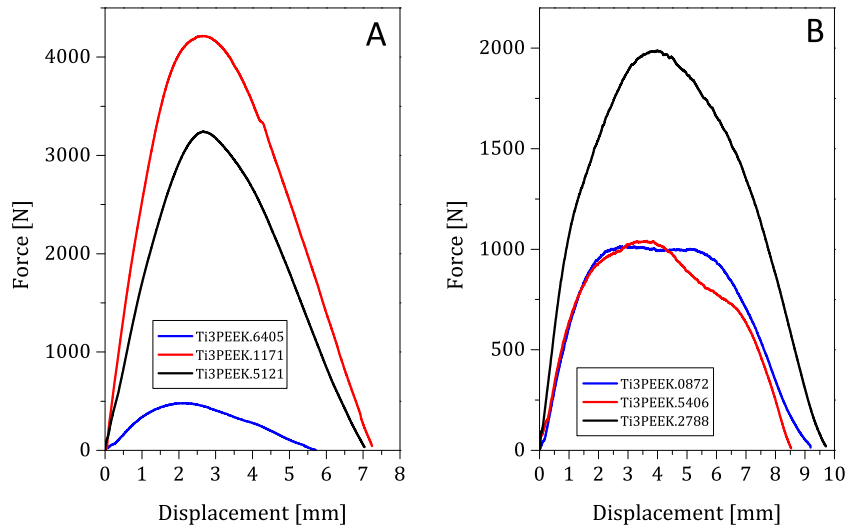


**Figure C.3.** Force–displacement curves of metallic-insert joints made of PEEK and grade 3 titanium; A: joined using configuration 5 and B: using configuration 6 (see Table 5.1)

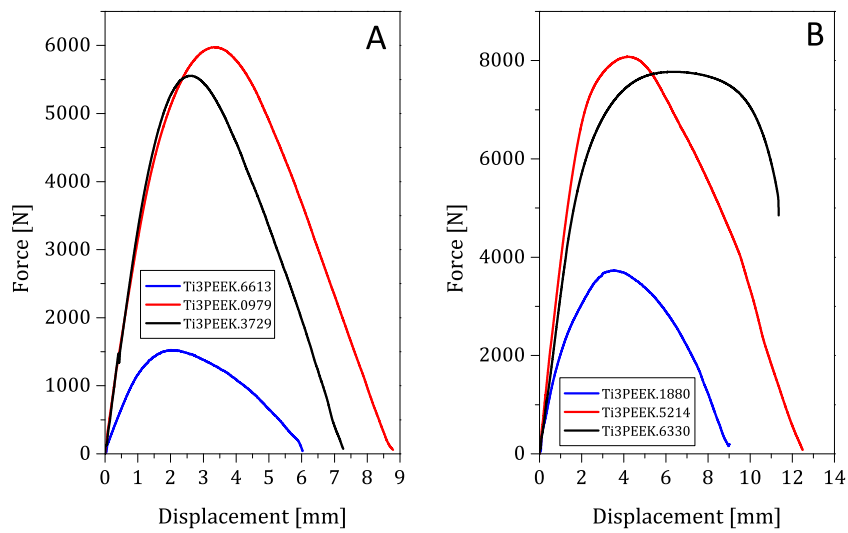


**Figure C.4.** Force–displacement curves of metallic-insert joints made of PEEK and grade 3 titanium; A: joined using configuration 7 and B: using configuration 8 (see Table 5.1)

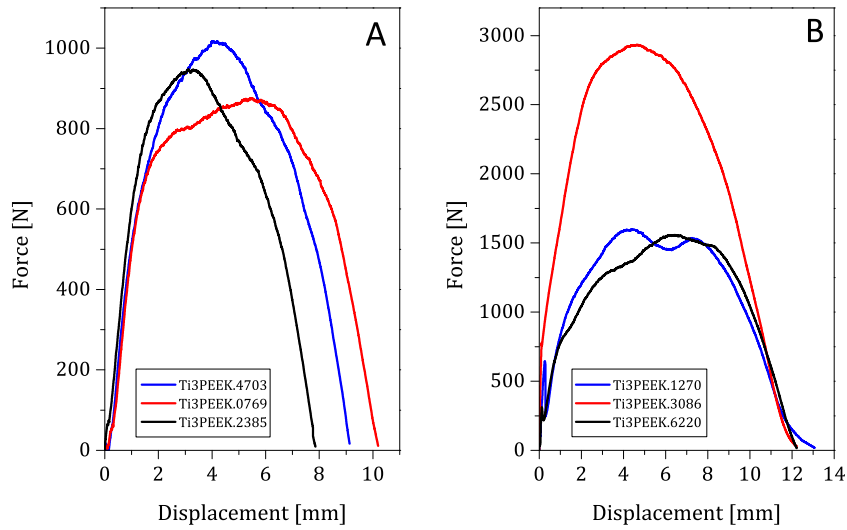


**Figure C.5.** Force–displacement curves of metallic-insert joints made of PEEK and grade 3 titanium; A: joined using configuration 9 and B: using configuration 10 (see Table 5.1)

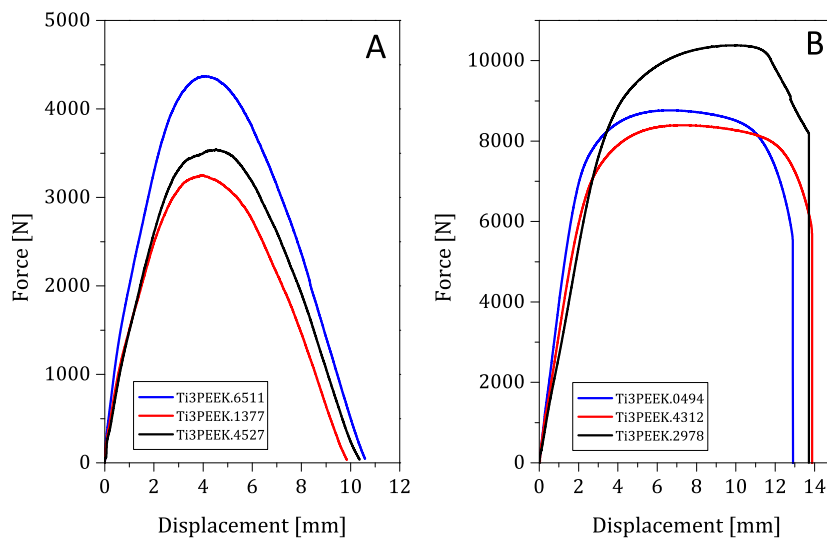


**Figure C.6.** Force–displacement curves of metallic-insert joints made of PEEK and grade 3 titanium; A: joined using configuration 11 and B: using configuration 12 (see Table 5.1)



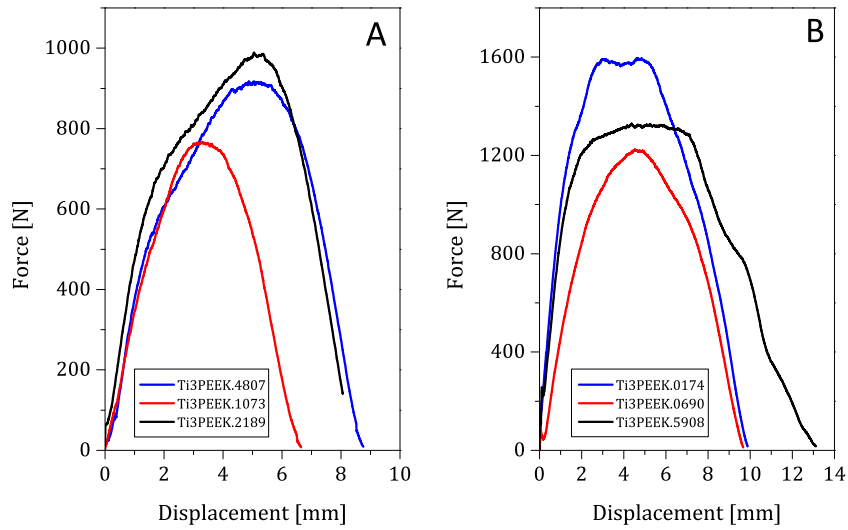


**Figure C.7.** Force–displacement curves of metallic-insert joints made of PEEK and grade 3 titanium; A: joined using configuration 13 and B: using configuration 14 (see Table 5.1)

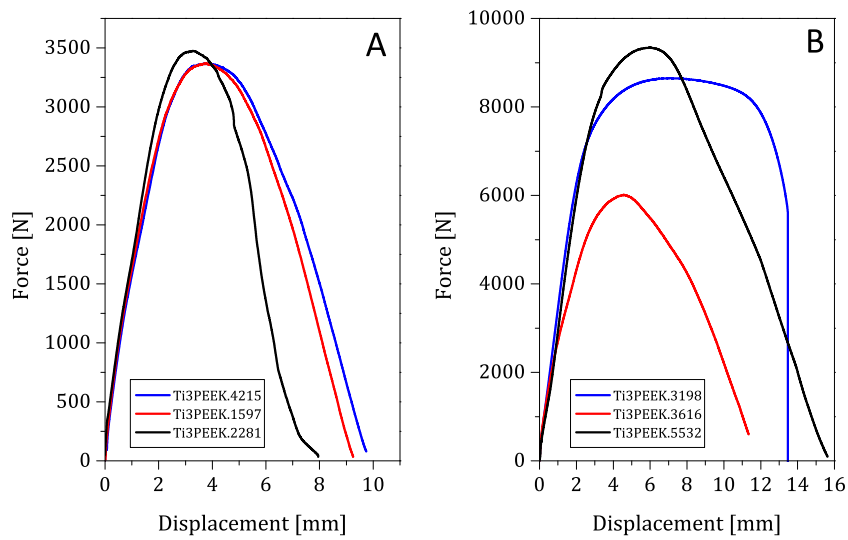


**Figure C.8.** Force–displacement curves of metallic-insert joints made of PEEK and grade 3 titanium; A: joined using configuration 15 and B: using configuration 16 (see Table 5.1)

## D. Appendix

X-ray radiographes of PEEK-CA30/Ti grade 3 metallic-insert joints

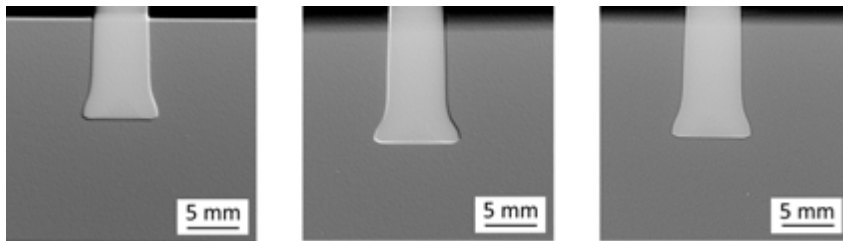


**Figure D.1.** X-ray scans of FricRiveted metallic-insert joints made of PEEK reinforced with 30% short carbon fibres and grade 3 titanium and joined using configuration 1 (see Table 6.2)

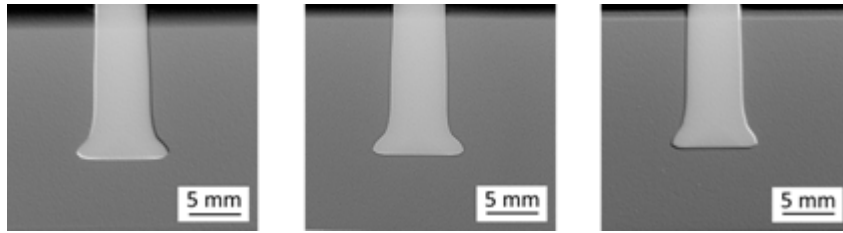


**Figure D.2.** X-ray scans of FricRiveted metallic-insert joints made of PEEK reinforced with 30% short carbon fibres and grade 3 titanium and joined using configuration 2 (see Table 6.2)

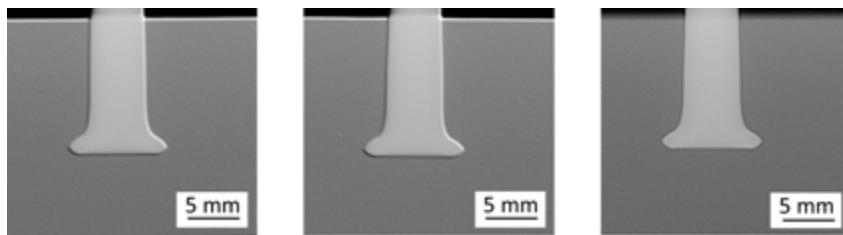


**Figure D.3.** X-ray scans of FricRiveted metallic-insert joints made of PEEK reinforced with 30% short carbon fibres and grade 3 titanium and joined using configuration 3 (see Table 6.2)

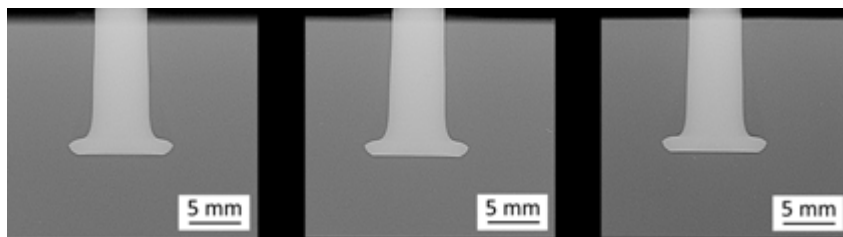


**Figure D.4.** X-ray scans of FricRiveted metallic-insert joints made of PEEK reinforced with 30% short carbon fibres and grade 3 titanium and joined using configuration 4 (see Table 6.2)

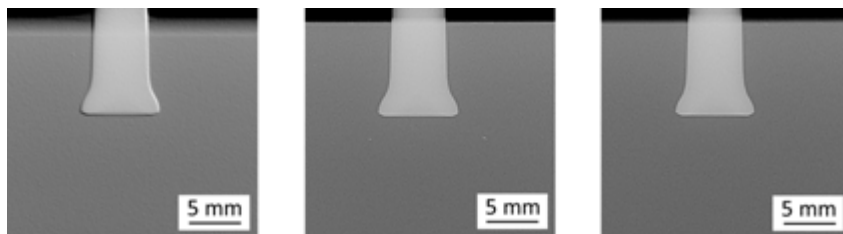


**Figure D.5.** X-ray scans of FricRiveted metallic-insert joints made of PEEK reinforced with 30% short carbon fibres and grade 3 titanium and joined using configuration 5 (see Table 6.2)

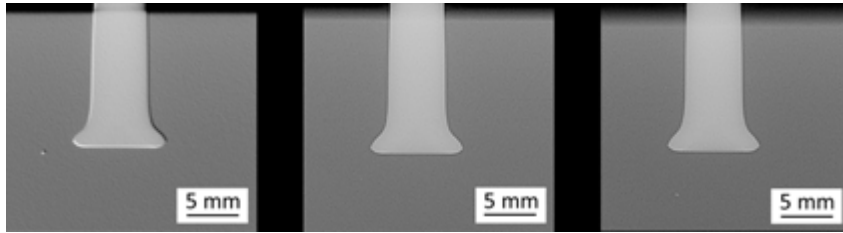


**Figure D.6.** X-ray scans of FricRiveted metallic-insert joints made of PEEK reinforced with 30% short carbon fibres and grade 3 titanium and joined using configuration 6 (see Table 6.2)

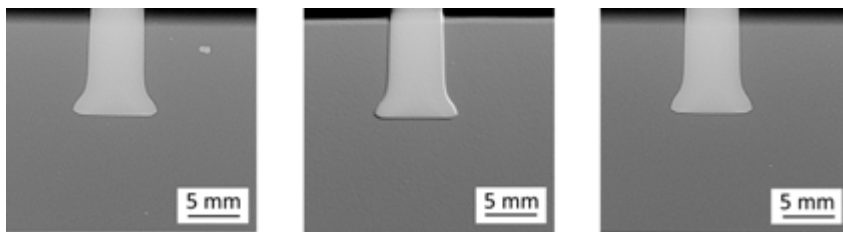


**Figure D.7.** X-ray scans of FricRiveted metallic-insert joints made of PEEK reinforced with 30% short carbon fibres and grade 3 titanium and joined using configuration 7 (see Table 6.2)

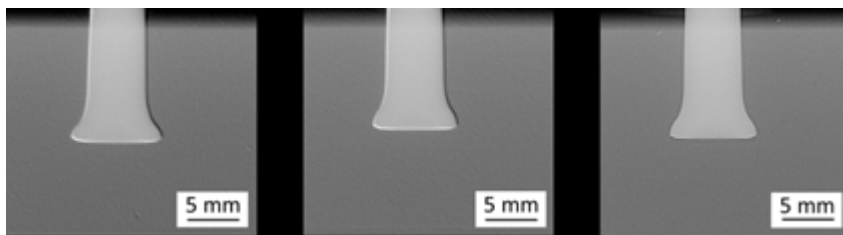


**Figure D.8.** X-ray scans of FricRiveted metallic-insert joints made of PEEK reinforced with 30% short carbon fibres and grade 3 titanium and joined using configuration 8 (see Table 6.2)

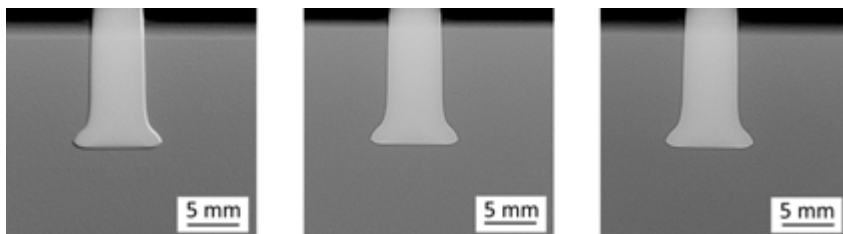


**Figure D.9.** X-ray scans of FricRiveted metallic-insert joints made of PEEK reinforced with 30% short carbon fibres and grade 3 titanium and joined using configuration 9 (see Table 6.2)

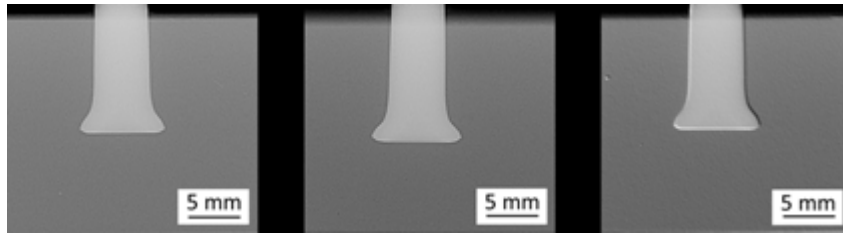


**Figure D.10.** X-ray scans of FricRiveted metallic-insert joints made of PEEK reinforced with 30% short carbon fibres and grade 3 titanium and joined using configuration 9 (see Table 6.2)

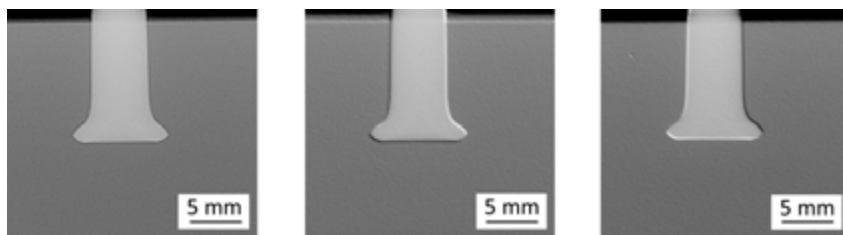


**Figure D.11.** X-ray scans of FricRiveted metallic-insert joints made of PEEK reinforced with 30% short carbon fibres and grade 3 titanium and joined using configuration 10 (see Table 6.2)

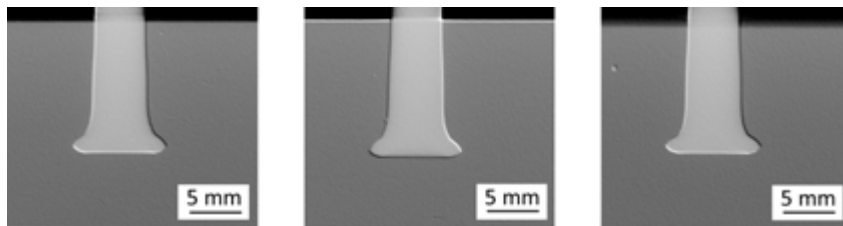


**Figure D.12.** X-ray scans of FricRiveted metallic-insert joints made of PEEK reinforced with 30% short carbon fibres and grade 3 titanium and joined using configuration 11 (see Table 6.2)

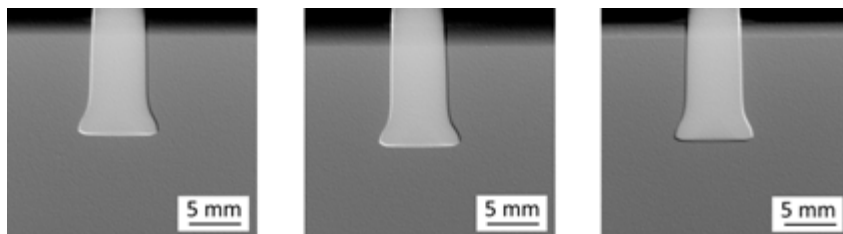


**Figure D.13.** X-ray scans of FricRiveted metallic-insert joints made of PEEK reinforced with 30% short carbon fibres and grade 3 titanium and joined using configuration 12 (see Table 6.2)

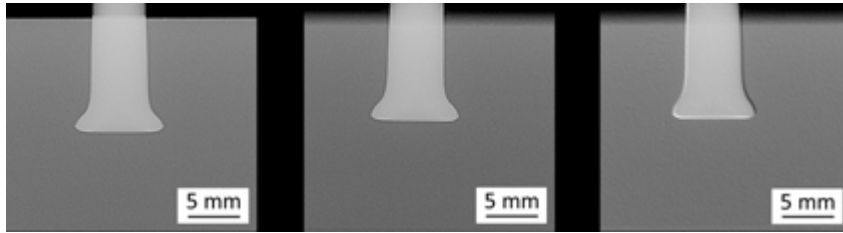


**Figure D.14.** X-ray scans of FricRiveted metallic-insert joints made of PEEK reinforced with 30% short carbon fibres and grade 3 titanium and joined using configuration 13 (see Table 6.2)

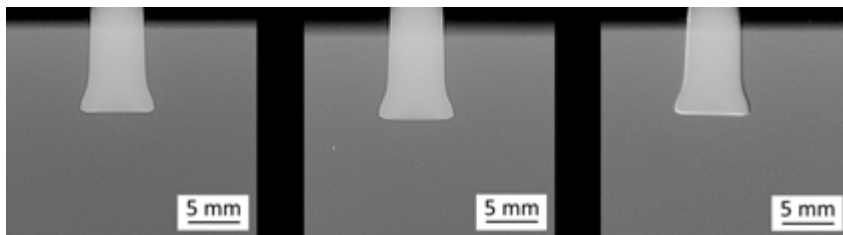


**Figure D.15.** X-ray scans of FricRiveted metallic-insert joints made of PEEK reinforced with 30% short carbon fibres and grade 3 titanium and joined using configuration 14 (see Table 6.2)

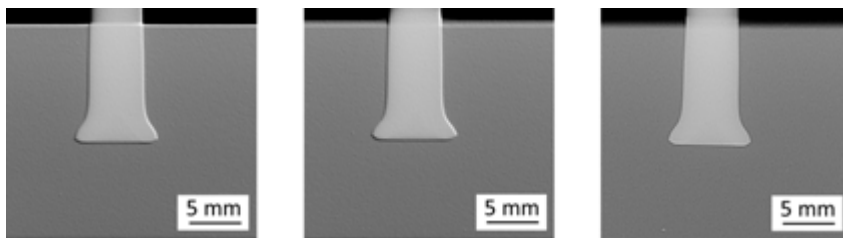


**Figure D.16.** X-ray scans of FricRiveted metallic-insert joints made of PEEK reinforced with 30% short carbon fibres and grade 3 titanium and joined using configuration 15 (see Table 6.2)

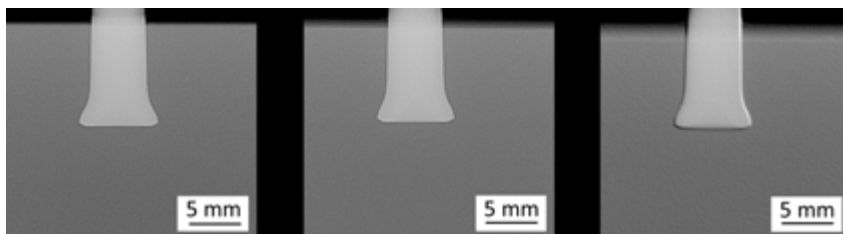


**Figure D.17.** X-ray scans of FricRiveted metallic-insert joints made of PEEK reinforced with 30% short carbon fibres and grade 3 titanium and joined using configuration 16 (see Table 6.2)

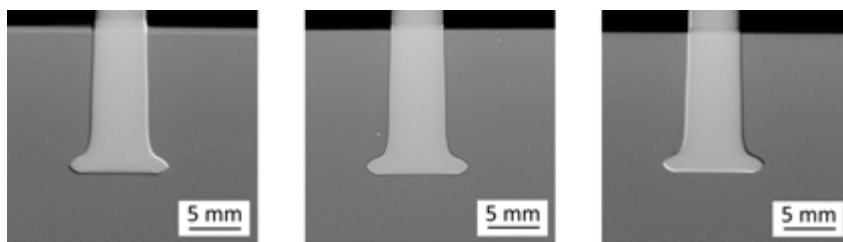


**Figure D.18.** X-ray scans of FricRiveted metallic-insert joints made of PEEK reinforced with 30% short carbon fibres and grade 3 titanium and joined using configuration 17 (see Table 6.2)

## E. Appendix

Temperature evolution during the FricRiveting process



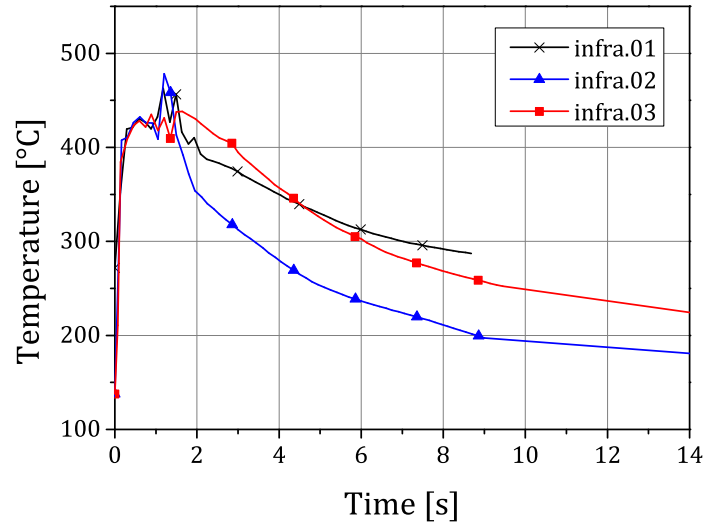


**Figure E.1.** Process temperature evolution during FricRiveting a metallic-insert joint, using configuration 0 (the configuration with the medium energy input which is also the optimised parameter set, see Table 6.4)

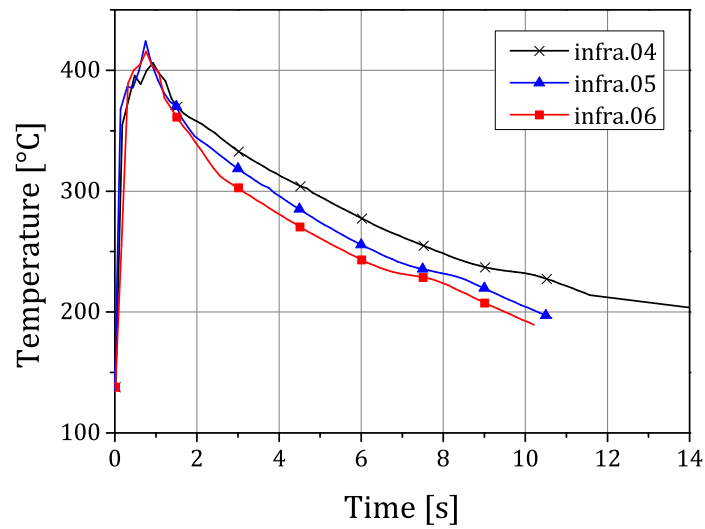


**Figure E.2.** Process temperature evolution during FricRiveting a metallic-insert joint, using configuration 14 (the configuration with the low energy input which is also the optimised parameter set, see Table 6.2)

## F. Appendix

**Table F.1.** Data sheet of the RSM 400 system (Harms & Wende GmbH, Germany)

RSM 400	
Weight	45 kg
Power	Asynchronous 1.85 kW or 3.0 kW
Supply voltage	24 VDC
Speed	6000 rpm to 23000 rpm
Supply	Max 1 MPa
Feed	Pneumatic, stroke 50 mm
Dimensions	280 mm in diameter, 550 mm length
Holding capacity	5 mm to 14 mm in diameter

### Differences between the RSM 400 and the RNA systems

For the RNA system, in comparison to the RSM 400 system, the characteristic of the rotational speed has been improved. The improvement is illustrated by a more uniform characteristic of the rotational speed curve of the RNA system showing smaller deviations from the set point. The main reason for this improvement was the use of a field-orientated controlled synchronous motor drive system with a closely coordinated rotational speed control operation, in the case of the RNA system. The disturbance variables, particularly the varying process torques acting on the rotational speed characteristic, were adjusted to give a uniform characteristic of the rotational speed over time. The RSM 400 drive, in contrast to the RNA system, is a open-loop controlled asynchronous machine [70], where any load-dependent rotational slip in speed cannot be detected or adjusted.

The marginal differences in the force characteristics can be attributed to the differences in the linear drive concepts of the two systems. The RSM 400 uses a simple pneumatic system [70], consisting of a cylinder and a piston charged with a control pressure which results in a corresponding force. Thus, also in case of disturbance, the RSM 400 system leads to a high degree of quality regarding the stabilisation of this force. The system performance is consistent with the behaviour of a soft but preloaded mechanical spring. However, the force measurement and a closed-loop control mode are not incorporated in the RSM 400 system. The linear drive concept of the RNA system is a closed-loop control system where the differences between the force set point and the resultant force were determined and subsequently readjusted

by the pneumohydraulic actuator system. The force characteristic is thus sensitive to dynamic changes of the contact properties of the joining partners and on the control settings.

The minor variation of the torque characteristics of the two systems can be interpreted as a result of the marginal differences in the characteristics of the rotational speed and the force. Compared to the RSM 400 system, the RNA has an integrated torque measurement system which can be used to monitor and control the process. Torque is measured in the RSM 400 system by the external torque measurement platform described in Subsection 4.2.1 and can only be used to monitor the process.

<b>H. LOITZ - ROBOTIK</b> <small>Dipl.-Ing. Henry Loitz</small>		
<b>Technische Daten</b>		
<b>Abmessungen</b>	Höhe	3,40 m (4,10 m)
	Breite	3,00 m
	Tiefe	3,80m
	Luftbedarf	ca. 6 bar, kontinuierlich
	Gewicht	ca. 5000 kg
<b>Leistungsdaten</b>	Höhe	1000x700x700 mm
	Spindelhub	50 mm
	Spindelperformance	21000RPM/25Nm
	Vertikalkraft	24kN bei 6bar
	Achs- geschwindigkeiten	160mm/sec Ebene 36mm/sec vertikal
<b>Anschlüsse</b>	Stromanschluss	3Ph~400 V /50 Hz 100 A
	Druckluft	Festo Kupplungs- stecker KS4- 1/2"
<b>Arbeitsgeräusche</b>	<p>&lt; 80 dB (A) im Leerlauf/Ruhezustand Spitzenwerte können darüber liegen. Es wird angemessener Gehörschutz empfohlen!</p> <p>Verordnung zur Umsetzung der EG-Richtlinien 2002/44/EG und 2003/10/EG zum Schutz der Beschäftigten vor Gefährdungen durch Lärm und Vibrationen)</p> <p>Vom 6. März 2007</p>	
2-7		

**Figure F.1.** Data sheet of the RNA system (H. Loitz-Robotik, Germany)

## G. Appendix

### Failure modes for bearing test specimens

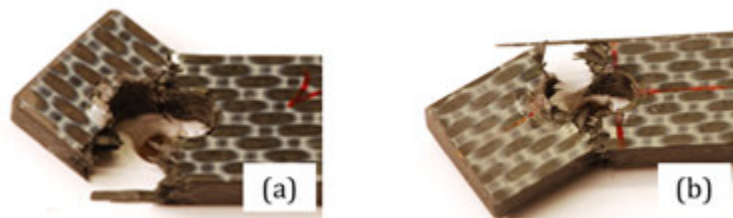


**Figure G.1.** Example of bearing test specimens with  $w = 3d$  and failing in: (a) net-tension ( $e = 2d$ ); (b) net-tension ( $e = 3d$ )

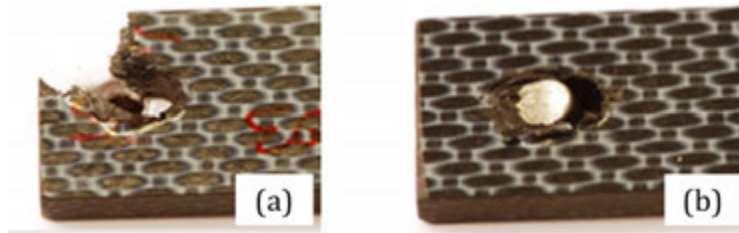


**Figure G.2.** Example of bearing test specimens with  $w = 4d$  and failing in: (a) cleavage ( $e = 2d$ ); (b) bearing ( $e = 3d$ )

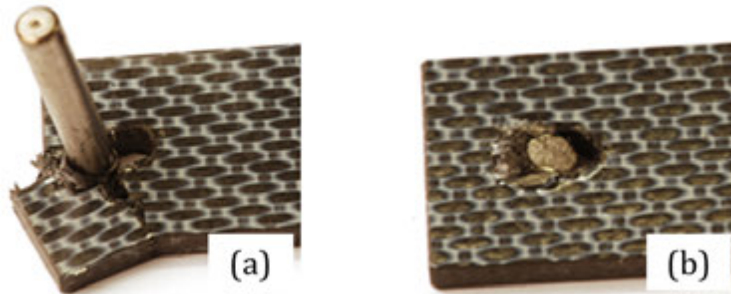


**Figure G.3.** Example of bearing test specimens with  $w = 5d$  and failing in: (a) cleavage ( $e = 2d$ ); (b) bearing ( $e = 3d$ )

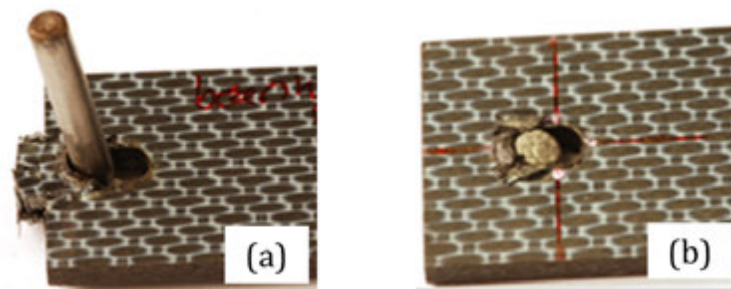


**Figure G.4.** Example of bearing test specimens with  $w = 6d$  and failing in: (a) shear-out ( $e = 2d$ ); (b) bearing ( $e = 3d$ )

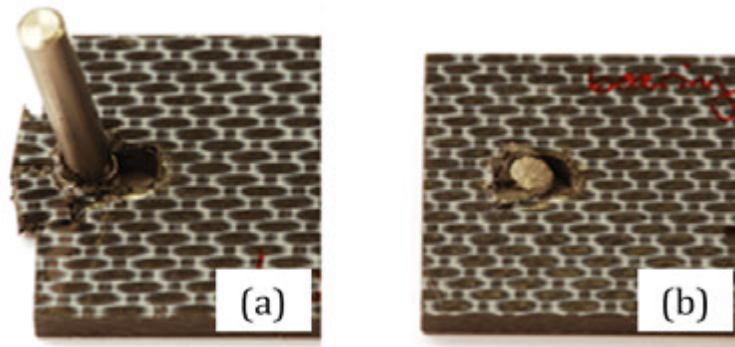


**Figure G.5.** Example of bearing test specimens with  $w = 7d$  and failing in: (a) shear-out ( $e = 2d$ ); (b) bearing ( $e = 3d$ )





## Danksagung

Diese Arbeit ist das Resultat meiner Forschung in dem Bereich Friction Riveting in der Abteilung Festphase-Fügeprozesse des Helmholtz-Zentrum Geesthacht. Die hier vorgestellten Ergebnisse hätten nicht ohne die Hilfe und Unterstützung vieler lieber Kolleginnen und Kollegen, Familie und Freunde erzielt werden können.

- Herrn Prof. Dr.-Ing. Sergio de Traglia Amancio Filho danke ich für die Betreuung meiner Doktorarbeit und Herrn Prof. Dr.-Ing. Wolfgang Hintze für die Übernahme des Zweitgutachtens.
- Dem Institutsleiter Herrn Prof. Dr.-Ing. Norbert Huber und meinem Abteilungsleiter Herrn Dr. Jorge F. dos Santos möchte ich für die Möglichkeit, meine Arbeit am Helmholtz-Zentrum Geesthacht zu verwirklichen, herzlich danken.
- Dr. Uceu Suhuddin, Henning Krohn, Matthias Beyer, Peter Haack, Karl-Heinz Balzereit, Petra Fischer, Falk Dorn, Menno Peters und Andre Abibe danke ich für die aktive Unterstützung bei der Durchführung der experimentellen Versuche.
- Für die motivierende und produktive Arbeitsatmosphäre sowie für ihre Unterstützung gilt mein Dank allen Mitarbeiterinnen und Mitarbeitern der Abteilung Festphase-Fügeprozesse wie auch den guten Seelen des Instituts, Frau Stephanie Koch und Dagmar Koschek.
- Henry Loitz, Dr.-Ing. Dirk Schnubel, Henning Krohn, Matthias Beyer, Dr. Arne Roos, Dr. Domenico Furfari, Marco Pacchione, Dr.-Ing. Jens Telgkamp und Dr. Uceu Suhuddin danke ich für ihre Freundschaft und die anregenden, fachlichen Diskussionen bezüglich verschiedener Aspekte meiner Arbeit. Herrn Henry Loitz danke ich außerdem für die Entwicklung und Umsetzung der Reibauftragsanlage, durch deren Einsatz die Friction Riveting Technologie nachhaltig optimiert werden konnte.
- Dr.-Ing. Daniel Kupka danke ich für die Geduld, in der Beantwortung meiner unzähligen Fragen bezüglich LATEX.
- Hilde Altmeyer, Eveline Altmeyer und Emely Bortel danke ich für ihre Anteilnahme an meiner fachlichen und persönlichen Entwicklung, ihre Unterstützung, ihr stets offenes Ohr bei allen Belangen und dafür dass ich an ihrer Lebenserfahrung teilhaben und davon profitieren darf.
- Mein ganz besonderer Dank gilt meinem großartigen Mann Flo Harres, meinem Herz Chloé Altmeyer sowie meinen besten Freunden Pascal Thome und Katrin Steinberger. In ihrer Mitte kann ich immer sein und sie geben mir das Gefühl von Herzen geliebt zu werden. Gemeinsames Eintauchen in die Nacht und Auftauchen im Sonnenlicht hat mir stets meine innere Balance zurück gegeben. Ihr seid mega!
- Meinen Eltern Michèle und Jörg Altmeyer bin ich unendlich dankbar für ihre bedingungslose Liebe und Unterstützung. Sie gaben mir alle Freiheit meinen eigenen Weg zu finden und diesen zu gehen.

